Numerical study on nitrogen injection at trans- and supercritical conditions
(versão corrigida após defesa)

João Miguel Nunes Cleto

Dissertação para obtenção do Grau de Mestre em
Engenharia Aeronáutica
(mestrado integrado)

Orientador: Prof. Doutor André Resende Rodrigues da Silva

junho de 2022

Numerical study on nitrogen injection at trans- and supercritical conditions

Dedication

To my family and friends, that guide me on this journey of becoming a Man in this world.

Numerical study on nitrogen injection at trans- and supercritical conditions

Acknowledgments

> *"The rung of a ladder was never meant to rest upon, but only to hold a man's foot long enough to enable him to put the other somewhat higher."*
>
> *Thomas H. Huxley*

Numerical study on nitrogen injection at trans- and supercritical conditions

Numerical study on nitrogen injection at trans- and supercritical conditions

Resumo

O presente estudo numérico investiga as diferenças entre a injeção de um único jato de azoto em condições transcríticas e supercríticas *gas-like* recorrendo a um método numérico baseado nas equações de Navier-Stokes com aplicação das médias temporais de Reynolds. Embora os propelentes sejam injetados em condições supercríticas nas câmaras de combustão de motores foguete de propelente líquido, a mistura dos propelentes pode resultar num comportamento transcrítico local, ou seja, a temperatura da mistura resultante pode ser caracterizada por variações de temperatura que são localmente inferiores às condições do ponto crítico. Assim, este estudo visa avaliar a adequação de modelos termodinâmicos e abordagens numéricas geralmente aplicadas a jatos em condições supercríticas na previsão do comportamento de jatos transcríticos.

Num motor foguete de propelente líquido, uma combustão mais eficiente é obtida à custa do combustível e/ou oxidante excederem os seus pontos críticos e entrarem no regime supercrítico. Embora estas condições estejam associadas há algumas décadas ao complexo ambiente das câmaras de combustão de motores foguetes, os fenómenos envolvidos ainda não são totalmente compreendidos, da mesma forma que as ferramentas necessárias para simular tais condições não estão completamente desenvolvidas.

O sistema de equações de governo é composto pelas equações de conservação da massa, quantidade de movimento e energia, às quais foram aplicadas as médias de Favre. Para lidar com as condições incompressíveis, mas de massa volúmica variável, características daquelas no interior da câmara de combustão, a técnica das médias temporais de Reynolds é substituída pelo método das médias de Favre. O sistema de equações é então fechado recorrendo ao modelo de turbulência $k - \varepsilon$ standard.

Realizar simulações numéricas envolvendo fluidos supercríticos não é uma tarefa direta, podendo provar ser um desafio. Como a lei de fluido ideal não é mais válida para descrever o comportamento do fluido devido ao comportamento não linear das propriedades termofísicas nestas condições, considera-se um desvio da formulação de fluido ideal, utilizando a Equação de Estado de fluido real de Peng-Robinson.

Por fim, os resultados obtidos numericamente são apresentados e validados com os dados experimentais. Enquanto uma maior aproximação aos dados experimentais é obtida tanto na previsão do comportamento do jato quanto na magnitude dos resultados para as condições supercríticas simuladas, é recuperada uma perceção sobre a transição entre comportamento de jato transcrítico e supercrítico. Observa-se ainda que a capacidade de prever o comportamento do jato transcrítico é preponderante nos resultados computacionais obtidos.

Palavras-chave

injeção em condições transcríticas, ponto crítico, motores foguete

Numerical study on nitrogen injection at trans- and supercritical conditions

Numerical study on nitrogen injection at trans- and supercritical conditions

Abstract

The present numerical study investigates the differences between the injection of a single nitrogen jet under transcritical and supercritical gas-like conditions resorting to a Reynolds-averaged Navier-Stokes-based numerical method. Albeit the propellants are injected under supercritical conditions into the combustion chambers of liquid rocket engines, the propellants' mixture can result in local transcritical behavior, i.e., the resulting mixture temperature can be characterized by temperature variations that are locally below its critical point condition. Therefore, this study aims to evaluate the suitability of thermodynamic models and numerical approaches generally applied to jets at supercritical conditions in the transcritical jet behavior prediction.

In a liquid rocket engine (LRE), higher combustion efficiency is obtained at the expense of both the fuel and/or the oxidizer exceeding their critical point and entering the supercritical regime. Even though these conditions have been associated for some decades with the complex environment of rocket combustion chambers, the involved phenomena are still not fully understood as well as the necessary tools to simulate such conditions are not completely developed.

The system of governing equations is composed of the Favre-averaged conservation equations of mass, momentum, and energy. To deal with the incompressible but variable density conditions, characteristic of those inside the combustion chamber, the Reynolds time-averaging technique is replaced by the Favre averaging method. The system of equations is then closed resorting to the standard $k - \varepsilon$ turbulence model.

Performing numerical computations involving supercritical fluids is not a straightforward task and can prove to be challenging. As the ideal gas law is no longer valid to describe fluid behavior due to the highly nonlinear behavior of the thermophysical properties at these conditions, ideal gas departure is considered, using the real gas Peng-Robinson Equation of State.

Ultimately, the numerically obtained results are presented and validated against the experimental data. While a greater approximation to the experimental evidence is attained both in predicting jet behavior and the magnitude of the results for the simulated supercritical conditions, awareness is retrieved into the transition between transcritical and supercritical jet behavior. In addition, it is observed that the ability to predict transcritical jet behavior is preponderant in the obtained computational results.

Keywords

Numerical study on nitrogen injection at trans- and supercritical conditions

x

Contents

List of Figures

Numerical study on nitrogen injection at trans- and supercritical conditions

List of Tables

Numerical study on nitrogen injection at trans- and supercritical conditions

Nomenclature

Re	Reynolds Number	-
Pr	Prandl Number	-
Pe	Péclet Number	-
c_p	Isobaric Specific Heat	$[\mathrm{J} \cdot \mathrm{kg}^{-1} \cdot \mathrm{K}^{-1}]$
c_v	Isochoric Specific Heat	$[\mathrm{J} \cdot \mathrm{kg}^{-1} \cdot \mathrm{K}^{-1}]$
γ	Adiabatic Index	-
R	Real Gas Constant	$[\mathrm{J} \cdot \mathrm{mol}^{-1} \cdot \mathrm{K}^{-1}]$
F	Thrust, Flux	$[\mathrm{N}], [\mathrm{m}^{-2}]$
$\dot{m}$	Mass Flow Rate	$[\mathrm{kg} \cdot \mathrm{s}^{-1}]$
A_e	Nozzle Exit Cross-Section	$[\mathrm{m}^2]$
I_{sp}	Specific Impulse	$[\mathrm{s}]$
g_0	Standard Surface Gravity	$[\mathrm{m} \cdot \mathrm{s}^{-2}]$
p	Pressure	$[\mathrm{MPa}]$
ρ	Density	$[\mathrm{kg} \cdot \mathrm{m}^{-3}]$
δ	Reduced Density	-
T	Temperature	$[\mathrm{K}]$
τ	Inverse Reduced Temperature	-
Q	Source Term	-
u	Velocity	$[\mathrm{m} \cdot \mathrm{s}^{-1}]$
u_τ	Friction Velocity	$[\mathrm{m} \cdot \mathrm{s}^{-1}]$
t	Time	$[\mathrm{s}]$
Δt	Time Interval	$[\mathrm{s}]$
Ω	Control Volume	$[\mathrm{m}^3]$
S	Control Surface	$[\mathrm{m}^2]$
U	Arbitrary Scalar	-
Γ	Diffusivity Coefficient	$[\mathrm{m}^2 \cdot \mathrm{s}^{-1}]$
σ_{ij}	Internal Stress Tensor	$[\mathrm{MPa}]$
τ_{ij}	Viscous Shear Stress Tensor	$[\mathrm{MPa}]$
s_{ij}	Strain-Rate Tensor	$[\mathrm{s}^{-1}]$
μ	Dynamic Viscosity	$[\mathrm{Pa} \cdot \mathrm{s}^{-1}]$
ν	Kinematic Viscosity	$[\mathrm{m}^2 \cdot \mathrm{s}^{-1}]$
ζ	Second Viscosity Coefficient	$[\mathrm{Pa} \cdot \mathrm{s}^{-1}]$
f_i	Body-Force Density Vector	$[\mathrm{N} \cdot \mathrm{m}^{-3}]$
E	Total Specific Energy	$[\mathrm{J} \cdot \mathrm{kg}^{-1}]$
e	Internal Specific Energy	$[\mathrm{J} \cdot \mathrm{kg}^{-1}]$
q	Heat Flux	$[\mathrm{J} \cdot \mathrm{s}^{-1}]$
κ	Thermal Conductivity, von Kármán constant	$[\mathrm{W} \cdot \mathrm{m}^{-1} \cdot \mathrm{K}^{-1}], -$
α	Thermal Diffusivity	$[\mathrm{m}^2 \cdot \mathrm{s}^{-1}]$
H	Total Specific Enthalpy	$[\mathrm{J} \cdot \mathrm{kg}^{-1}]$

Numerical study on nitrogen injection at trans- and supercritical conditions

h	Specific Enthalpy	$[\mathrm{J \cdot kg^{-1}}]$
t_{ij}	Reynolds Stress Tensor	$[\mathrm{MPa}]$
$\tilde{s}_{ij}$	Mean Strain-Rate Tensor	$[\mathrm{s^{-1}}]$
k	Turbulent Kinetic Energy	$[\mathrm{m^2 \cdot s^{-2}}]$
ε	Turbulent Dissipation Rate	$[\mathrm{m^2 \cdot s^{-3}}]$
ω	Specific Dissipation Rate, Acentric Factor	$[\mathrm{s^{-1}}]$, -
δ_{ij}	Kronecker Delta Function	-
l	Characteristic Length Scale	$[\mathrm{m}]$
l_{mix}	Mixing Scale	$[\mathrm{m}]$
y	Absolute Distance to Wall	$[\mathrm{m}]$
v	Molar Volume	$[\mathrm{m^3 \cdot mol^{-1}}]$
M	Molar Mass	$[\mathrm{g \cdot mol^{-1}}]$
θ	Explicit Under-Relaxation Factor	-
Δx	Spatial Interval	$[\mathrm{m}]$
x	Spatial Coordinate	$[\mathrm{m}]$
d	Injector's Diameter	$[\mathrm{m}]$
r	Radial Distance	$[\mathrm{m}]$
I	Raman Signal Intensity, Turbulence Intensity	$[\mathrm{J \cdot kg \cdot m^{-1}}]$, [%]
h_f	Heat Transfer Coefficient	$[\mathrm{W \cdot m^{-2} \cdot K^{-1}}]$

Subscripts

e	Nozzle Exit Condition
cc	Combustion Chamber Condition
inj	Injection Condition
∞	Background, Chamber Condition
c	Critical Point Condition
pb	Pseudo-boiling Condition
r	Reduced Variable
w	Wall
S	Surface
V	Volume
A	Advective
D	Diffusive
i, j, k, x, y, z	Cartesian Directions

Superscripts

$+$	Wall Unit
$*$	Dimensionless Variable Based on Injection and Chamber Conditions
0	Dilute Gas Contribution
r	Residual Contribution
c	Critical Enhancement Contribution
$\overline{\phi}$	Reynolds Average
$'$	Reynolds Fluctuation
$\tilde{\phi}$	Favre Average
$''$	Favre Fluctuation

Additional Equation of State Parameters

a, b

β, m

A, B, Z

σ, T^*, θ

$N_i, t_i, d_i, l_i, \gamma_i$

q_D, k_B, R_0

$\Phi, \hat{\Phi}, \hat{\Phi}_0$

$\xi, \xi_0, \widetilde{\chi}$

$\mathbf{v}, \gamma, \Gamma$

Turbulence Modelling Coefficients

$C_{\varepsilon 1}, C_{\varepsilon 2}, C_\mu$

$\sigma_k, \sigma_\varepsilon$

List of Acronyms

AEROG	Aeronautics and Astronautics Research Center
AFRL	Air Force Research Laboratory
CFD	Computational Fluid Dynamics
DLR	Deutsches Zentrum für Luft- und Raumfahrt
DNS	Direct Numerical Simulation
EoS	Equation of State
FVM	Finite Volume Method
LES	Large Eddy Simulation
LRE	Liquid Rocket Engine
MBWR	Modified Benedict-Webb-Rubin
NIST	National Institute of Standards and Technology
PR	Peng-Robinson
QUICK	Quadratic Upstream Interpolation for Convective Kinematics
RANS	Reynolds-averaged Navier-Stokes
SRK	Soave-Redlich-Kwong
UDF	User Defined Function

Chapter 1

Introduction

The attractiveness of supercritical fluids has been demonstrated through numerous studies and successful implementation in the most varied fields of work. However, this concept is not relatively recent, nor was it humanly created.

A fluid is considered to be in a supercritical state when both its temperature and pressure values are above the critical point conditions. The critical temperature, T_c, characterizes the point beyond which a transition to the liquid phase is no longer possible, regardless of the applied pressure. The critical pressure, p_c, is then defined as the vapor pressure at the critical temperature. Thus, the critical point marks the end of the coexistence line (vapor-pressure curve), where both temperature and pressure reach their respective critical values [1].

A supercritical state is characterized by $T > T_c$ and $p > p_c$ however, according to the positioning in relation to the critical point values for temperature and pressure, three additional regimes can be described. A second regime, designated by subcritical regime, is characterized by temperature and pressure values below their respective critical point values. Regarding the other two, each one can be defined by combining the value of one of the properties (temperature and pressure) being above the corresponding critical point value and the other below it. Thus, in the $T > T_c$ and $p < p_c$ case study, we operate in the superheated regime; whereas, for the $T < T_c$ and $p > p_c$ conditions, we operate in the transcritical regime.

Several processes in Nature have been resorting to supercritical fluids for billions of years. Either by processing minerals in aqueous solutions near or above the critical point of water [2] or by the formation of supercritical water in underwater volcanoes as a consequence of elevated water pressure and volcanic eruption temperature [3]. The primarily CO_2 comprised Venus atmosphere is another example, as it can be considered to be in the supercritical regime due to its temperature and pressure values [4, 5].

The existence of supercritical fluids was first noted by Baron Charles Cagniard de la Tour around 1822. Since then, the number of applications using these fluids has increased where examples of applications ranging from their use in supercritical drying in the production of aerogels due to their convenient properties in the removal and cleaning of surfaces to their use in the energy domain where, e.g., supercritical water is used in power-plant steam generators [6].

Several applications present some benefits as they can require less energy consumption in

various industrial processes while compared to the conventional ones, have a lower environmental impact, there is the possibility of adjusting their thermophysical properties by just changing the operating temperature and/or pressure, or lead to improvements in terms of process efficiency [7, 8].

Noticeable developments have also been accomplished in the propulsion field, with the introduction of higher pressure systems in the development of liquid rocket engines (LREs), gas turbines, and diesel engines [9–11]. The operation at higher chamber pressures in LREs allows obtaining higher specific impulse values, whereas in gas turbines and diesel engines an increase in power output and efficiency is registered [12]. In this work, the focus will be on the first type of engine.

Rocket engine technology has been developing for decades, either through its application in space programs or through the creation of ballistic missiles. The use of these engines is very appealing since they take along both their fuel and oxidizer, making them independent of the involving atmosphere for its combustion, in contrast with jet engines that need oxygen from the surrounding atmosphere for their functioning [11]. Therefore, rocket engines can operate in the vacuum of space leading them to be one of the most used propulsion systems for that kind of mission.

The working principle of rocket engines, explained by Newton's third law, is based on the creation of reaction forces that thrust the vehicle as a consequence of the mass that is accelerated and expelled. These reaction forces are then created as a result of the chemical reaction between the fuel and oxidizer, injected into the combustion chamber, where combustion takes place in a relatively small volume. Consequently, a thermal expansion occurs, creating high-pressure and high-temperature combustion products that are then accelerated and expelled through a nozzle.

The thrust F produced by this type of engine can be expressed as the sum of two contributions, where the first is named impulse or momentum thrust while the second is pressure thrust. In equation (1.1), $\dot{m}$ represents the total mass flow rate of the combustion products and p_∞ the (undisturbed) atmospheric pressure. Additionally, u_e, A_e, and p_e represent the exhaust gases velocity, the cross-section area, and the pressure at the nozzle exit, respectively [13].

$$F = \dot{m}u_e + A_e\left(p_e - p_\infty\right) \quad \text{(1.1)}$$

Regarding the specific impulse, I_{sp}, it is the total impulse per unit weight of propellant and represents an important figure of merit of the performance of a rocket propulsion system. This parameter portraits how much thrust can be extracted from a unit of weight of propellant and, for that reason, high values of specific impulse are desirable.

Assuming that the expansion through the nozzle is isentropic, the nozzle exit pressure is

equal to the ambient pressure, and the velocity inside the combustion chamber is negligible, we have

$$I_{sp} = \frac{F}{g_0 \dot{m}} = \frac{1}{g_0} \left\{ \frac{2\gamma}{\gamma - 1} R T_{cc} \left[1 - \left(\frac{p_e}{p_{cc}} \right)^{\frac{\gamma - 1}{\gamma}} \right] \right\}^{1/2} \quad (1.2)$$

where T_{cc} and p_{cc} are the temperature and pressure in the chamber, and R is the specific gas constant.

From the analysis of equation (1.2), it can be noted that the combustion temperature T_{cc} should be high. The combustion temperature is mainly controlled by the chemistry of the fuel and oxidizer, where the propellants will burn at a specific temperature called adiabatic flame temperature, whose value is determined by the heat of reaction. The propellants choice is important since the more highly reacting they are, the higher the T_{cc} is.

In rocket engines, the choice of propellants to be used is often the same or, by changing them, the handicaps to face are the same. In the LRE field, a typical fuel–oxidizer combination consists of the coaxial injection of hydrogen and oxygen or methane, or hydrazine. As such, not being able to change much more parameters, the choice to obtain higher values of I_{sp} lies in T_{cc} and p_{cc}. Therefore, by changing these parameters, higher efficiency of the chemical reaction is obtained, thus reducing the mass of propellants necessary to achieve a given objective, consequently increasing the available mass for payload.

These results led to the general trend observed in the propulsion area of the adoption of increasingly higher combustion chamber pressures. However, as a consequence of operating at elevated pressures, conditions exist in which the injected fluid(s) might be subject to ambient pressures that exceed the critical pressure(s) of the propellants. Some examples of LREs that operate at chamber pressures above the critical conditions are the RS-25, the LE-7A, and the Merlin 1D engines (used in the Falcon 1, Falcon 9, and Falcon Heavy launch vehicles) [14–16].

The research in the flow behavior field and injection phenomena under these conditions is essential to deepening knowledge on the processes that occur in a LRE combustion chamber. While some phenomena are not fully understood, understanding the complex environment of rocket combustion chambers gives the designer more reliable and time/cost-saving tools to project a higher-performance rocket engine.

In the present numerical study, following the experimental work of Oschwald et al. [17], nitrogen N_2 surrogates the $LO_2 - H_2$ combination, typical of LREs. Its relative handling easiness, increased safety it provides when compared with the use of O_2 ($p_{c,O_2}/p_{c,N_2} \approx 1.48$), and similar characteristics to those of the $LO_2 - H_2$ mixture, allow N_2 to be a reference as working fluid in the study of the behavior of supercritical fluids, without considering chemical equilibrium or even the effects of combustion [10].

However, experimental campaigns resorting to supercritical fluids face several challenges, e.g., the associated costs, the complexity of the processes under these conditions, and the reliable measurement techniques. Alternatively, when validated for specific conditions, the Computational Fluid Dynamics (CFD) tools can provide valuable information about the phenomena involved without facing these sometimes insurmountable challenges. In this way, the use of an accurate numerical solver based on proven mathematical and physical models, aiming at characterizing the flow behavior and injection phenomena inside the combustion chamber of LREs, can be seen as an equally powerful means of generating knowledge.

1.1   Objectives

This work investigates the differences between the injection of a single nitrogen jet under transcritical and supercritical gas-like conditions into a combustion chamber filled with supercritical nitrogen. For that purpose, it resorts to a Reynolds-averaged Navier-Stokes (RANS)-based numerical method. A mathematical model based on an incompressible but variable density approach, capable of dealing with the sharp temperature and density gradients and the nonlinear behavior of the thermodynamic properties characteristic of the flows inside the combustion chambers of LREs, is proposed. Hence, through the employment of a RANS approach, we aim to evaluate the performance of thermodynamic models and numerical approaches in supercritical injection cases and evaluate their suitability in the prediction of transcritical jet behavior.

The motivation for carrying out this work lies within the scope of other studies also developed in the Aeronautics and Astronautics Research Center (AEROG), e.g., the validation of the use of a variable density but incompressible approach in the study of cryogenic nitrogen jets under supercritical conditions [18]; the study and modeling of nitrogen jets under trans- and supercritical conditions, where it is found that the methods employed for the calculation of the transport properties have a reduced effect on the obtained numerical results as opposed to turbulence that appears to have a crucial role in jet behavior [19]; the evaluation of the performance of several turbulence models in supercritical nitrogen mixing layers, where no direct correlation is found between the complexity of a turbulence model and the accuracy of the numerically obtained results [20]; the evaluation of jet topology for different injectors' conditions, where the results demonstrate the influence of a 'thermal breakup mechanism' concept suggested in the literature [21]. In this way, the present work intends to extend the analyzes previously performed to the transcritical regime.

1.2   Challenges

Performing numerical computations involving supercritical fluids is not a straightforward task. The operation near or under supercritical conditions creates several challenges, which may require the use of more complex mathematical and physical models or the adoption of certain approximations.

Near the critical point conditions, we are in the presence of thermodynamic singularities. While the mass diffusivity, surface tension, and latent heat are zero, the isentropic compressibility, isobaric specific heat, and thermal conductivity tend to infinity, thus portraying the singular behavior of thermodynamic properties in the vicinity of the critical point. However, this nonlinear behavior of the thermophysical properties, particularly in the Widom line vicinity, makes their accurate modeling a challenging task in the description of supercritical fluid behavior. In the transport properties definition, it may even be necessary to introduce additional models to surpass this nonlinear behavior.

In addition, the ideal gas law is no longer adequate to describe fluid behavior, near and beyond the critical point, since diffusion coefficients become functions of pressure besides temperature. Hence, this departure from ideal gas behavior must be considered. Furthermore, while operating under supercritical conditions, the flow reveals a quantitative similarity to gas jet-like behavior. Therefore, the flow can be successfully described with an approach developed for incompressible but variable density flows.

The prediction of the behavior of supercritical fluids is thus subject to challenges such as these requiring the creation and development of models that allow capturing as closely as possible these strong variations resulting from operating near and beyond the critical point.

1.3   Overview

The present work is organized into seven distinct chapters. The current chapter, Chapter 1, presents a contextualization of the supercritical fluids field and the motivation, objectives, and challenges of this work. Chapter 2 introduces important considerations and fundamental concepts concerning the supercritical regime and presents a literature review of relevant experimental and numerical studies regarding supercritical fluid behavior. Chapter 3 aims to describe the mathematical and physical models employed in this work. Chapter 4 presents the numerical algorithm used to apply the equations from the previous models to a discrete domain, aiming to maintain minimal associated error. Moving on to Chapter 5, this chapter focuses on presenting the experimental test matrix of the experimental study of reference alongside the corresponding computational domain and associated initial and boundary conditions. In Chapter 6, the numerically obtained results are presented and compared against the experimental data. Finally, Chapter 7 presents the most pertinent conclusions of this work and introduces future work suggestions.

Chapter 2

State of the Art

This chapter presents some fundamental concepts and definitions towards a better understanding of the supercritical regime and its effects on fluid behavior. Then, some of the considerations elaborated in the literature are presented along with a study review that has been carried out both in the experimental and computational domains.

2.1   Considerations on the supercritical regime

With the increase in pressure and temperature in combustion chambers of LREs, while enhancing injection and combustion efficiencies, both the fuels and oxidizers can exceed their critical point conditions. When that is the case, we have entered the domain of supercritical fluid flows.

A fluid is considered to be in a supercritical state when both its pressure and temperature values are above the critical point conditions. In the case of a pure substance, the critical pressure, p_c, and temperature, T_c, act as identifiers of the fluid [6]. The ideal gas Equation of State (EoS) is no longer appropriate to describe the fluid behavior considering that diffusion coefficients become functions of pressure besides temperature [22]. In addition, dense fluid corrections are necessary in the form of departure functions to the thermodynamic variables.

Near the critical point conditions, thermophysical properties present a distinct behavior as while the mass diffusivity, surface tension, and latent heat are zero, the isentropic compressibility, isobaric specific heat, and thermal conductivity tend to infinity. In addition, a phenomenon named critical divergence takes place as the isobaric specific heat tends to infinity and thermal diffusivity to zero [23]. Considering this distinct behavior at the critical point, we can therefore say we are in the presence of thermodynamic singularities.

However, a noticeable characteristic of a supercritical state is that the discontinuity between the liquid and gas phases noted at subcritical conditions is no longer present due to the disappearance of the surface tension at and beyond the critical point. As a result, there is only a single-phase behavior under supercritical conditions, where the single term "fluid" is used instead [24,25]. Oschwald et al. [10] reported similar phenomena as they performed surface tension measurements for oxygen from subcritical temperatures, with higher values, up to the critical temperature, for which it completely vanishes.

Besides the isobaric specific heat, c_p, as will be further discussed in this section, the dynamic

viscosity, μ, and the thermal conductivity, λ, are also greatly affected near and at supercritical conditions. Both present a strong nonlinear behavior in the supercritical regime, as depicted in Figures 2.1 and 2.2, with the values available from the National Institute of Standards and Technology (NIST) database [26]. In these Figures, it is possible to ascertain the evolution of dynamic viscosity and thermal conductivity for several pressure levels, respectively. In this way, the definition of the evolution of each of these properties becomes a very important assignment. As a result, Section 3.7 addresses this assignment.
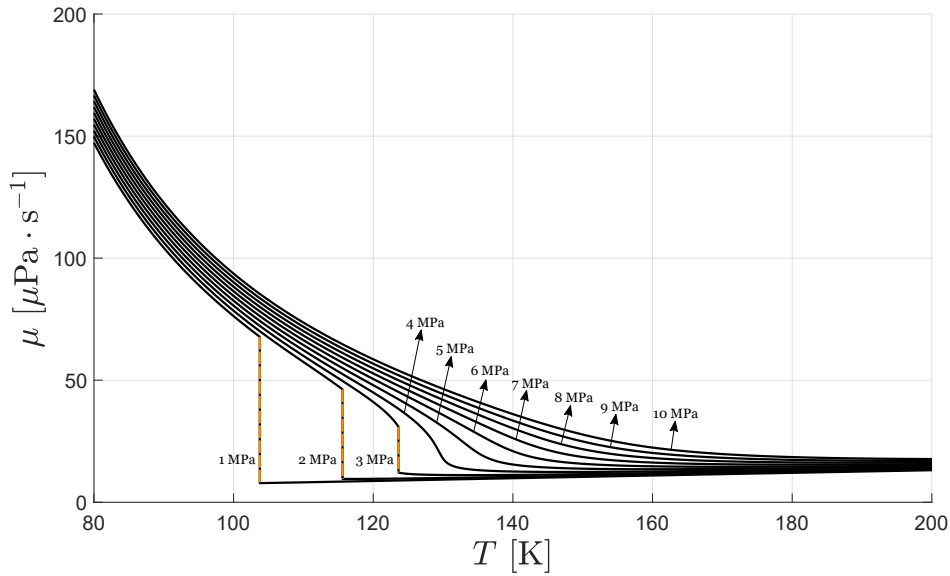
Figure 2.1: Plots of dynamic viscosity for nitrogen for pressures from 1 MPa to 10 MPa, dashed lines represent liquid-vapor discontinuity (data from the NIST database) [26].
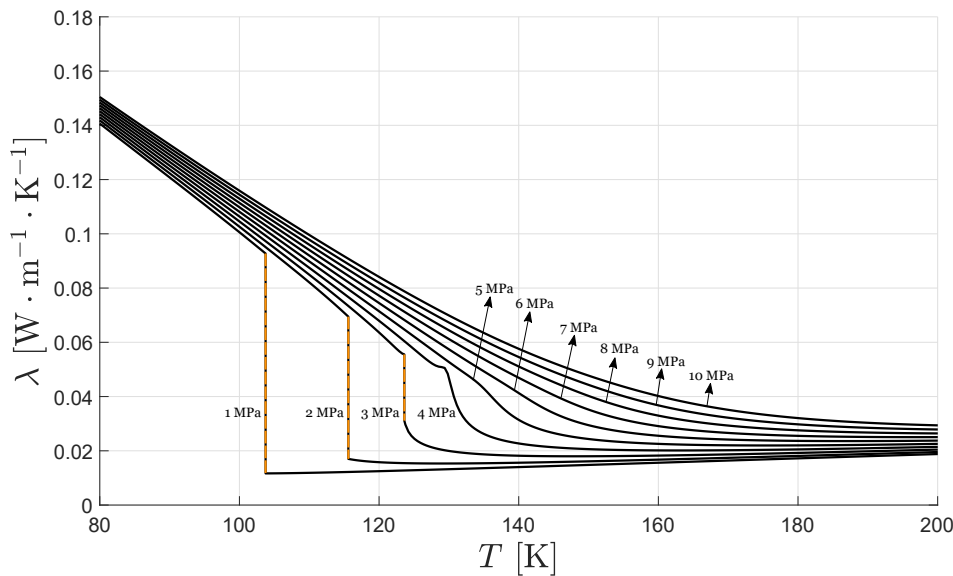
Figure 2.2: Plots of thermal conductivity for nitrogen for pressures from 1 MPa to 10 MPa, dashed lines represent liquid-vapor discontinuity (data from the NIST database) [26].

Numerical study on nitrogen injection at trans- and supercritical conditions

A supercritical state is characterized by $T > T_c$ and $p > p_c$ however, according to the positioning in relation to the critical point values for temperature and pressure, three other regimes can be defined. Figure 2.3 shows a representation of the definition of the various regimes.
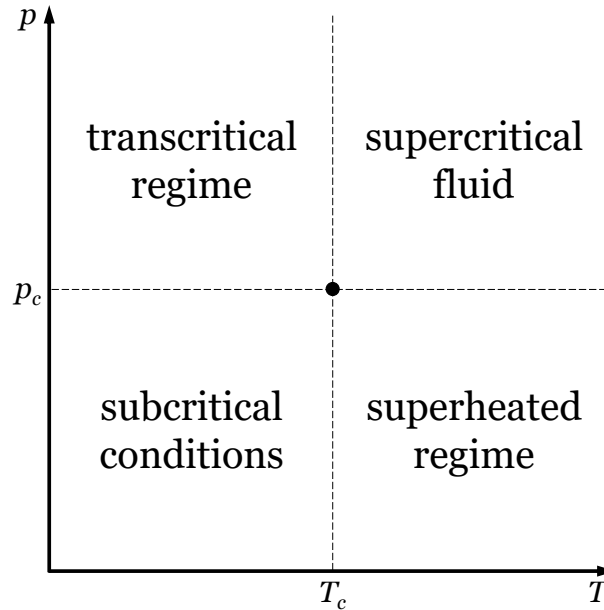
Figure 2.3: Regime definition.

A subcritical fluid is characterized by temperature and pressure values below their respective critical point values. In the same region, it is possible to present the classic phase diagram where the gaseous, liquid, and solid phases are represented along with the corresponding coexistence lines [1].

Concerning the other regimes, each one can be characterized by the value of one of the properties (temperature and pressure) being above the corresponding value of the critical point and the other below it. In the case of the superheated regime, the temperature is above the critical point value and pressure below it, and in a transcritical regime case, the temperature is below the critical point value and pressure above it. In the referred transcritical regime, until the temperature exceeds the critical point value, it is considered to be in the presence of a compressed liquid.

Even taking into account that nitrogen is not employed as a propellant in liquid rocket propulsion, its relative handling easiness and the increased safety it provides when compared, e.g., with the use of oxygen (for reference, $p_{c,\text{O}_2} = 5.04$ MPa and $T_{c,\text{O}_2} = 154.6$ K), make it a working fluid of great reference in the study of the behavior of supercritical fluids, without considering chemical equilibrium or even the effects of combustion. Additionally, for the same conditions, the fact that nitrogen has characteristics similar to those of the oxygen-hydrogen mixture, commonly used in liquid rocket propulsion, further strengthens its use in this area of study [10, 27].

Numerical study on nitrogen injection at trans- and supercritical conditions

When working with supercritical fluids and discussing the regime characterization, the phase diagram can present an interesting point of view. Figure 2.4 depicts a phase diagram.
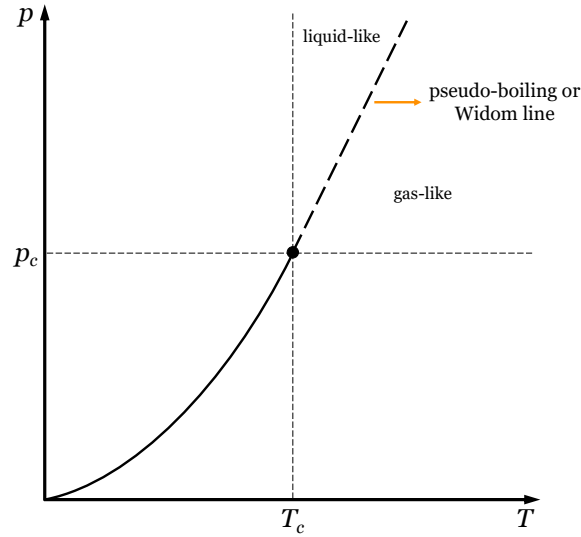
Figure 2.4: Phase diagram and pseudo-boiling or Widom line.

Since nitrogen is the working fluid at study, Table 2.1 presents its critical properties. These properties can be used to locate its critical point in a phase diagram, like the one depicted in Figure 2.4.

Table 2.1: Critical properties of nitrogen (data from the NIST database) [26].

Property	Value
T_c [K]	126.192
p_c [MPa]	3.3958
ρ_c [kg $\cdot$ m^{-3}]	313.300

In order to try to reach an agreement and resolve some of the contradictions, Banuti et al. [28] performed molecular dynamics to argon. In this work, the authors divide transitions at the supercritical fluid state into two major concepts: a thermodynamic one, having a macroscopic nature, and a dynamic one, occurring in the microscopic domain. The thermodynamic transition is associated with the crossover across the Widom line, this being the continuation of the coexistence line (vapor-pressure curve), present at subcritical conditions, into the supercritical regime. As it resembles the subcritical boiling phenomenon, it is also named the pseudo-boiling line. In contrast to the thermodynamic case, the dynamic transition [29–31] does not lead to a sudden change of thermodynamic fluid properties.

The pseudo-boiling or Widom line separates a supercritical liquid-like state from one supercritical gas-like state, where the transition phenomenon is named "pseudo-boiling" [10]. Associate to this transition, the disappearance of latent heat makes mass diffusion the governing parameter rather than vaporization, while the absence of surface tension leads the

diffusion process to dominate the jet atomization.

Banuti [32], introduces pseudo-boiling, describing that at supercritical conditions, the energy supplied to the fluid is used to both overcome molecular attraction and to raise its temperature. In addition, the author termed both contributions as structural and thermal, respectively. Therefore, this process differs from what occurs in the subcritical case since, in that case, the temperature remains constant, and all the supplied energy is used to overcome molecular attraction. The differentiation between structural and thermal contributions will therefore influence the jet evolution, as a result of crossing the Widom line and the respective pseudo-boiling temperature. For that reason, the critical temperature is no longer the transition criterion being then replaced by the pseudo-boiling temperature.

The c_p-Widom line is a line that contains the points at a pressure above the critical pressure and at a temperature $T > T_c$ that corresponds to the maximum value of the isobaric specific heat at this particular pressure (pseudo-boiling points).

Nevertheless, while studying the behavior of the propellant mixture inside the combustion chamber of a LRE operating with a bi-propellant mixture, e.g., oxygen-hydrogen, the pressure and temperature ranges of nitrogen must be established as representative of the phenomena that now take place in the chamber.

In case the oxygen and hydrogen injection into the combustion chamber occurs separately and, at supercritical conditions, the behavior of the resulting mixture will undergo several changes [33, 34]. This behavior can be characterized by temperature variations that are locally lower than the critical mixing temperature, thus positioning the mixture in the trans-critical regime. Subsequently, the conditions in the chamber would lead to a mixing temperature increase, eventually crossing the critical point, thus approaching supercritical liquid-like conditions. In case of an even higher mixing temperature increase, the mixture would further be subjected to pseudo-boiling effects, and eventually cross the Widom line into supercritical gas-like conditions [32].

This transition from liquid-like supercritical conditions to gas-like supercritical conditions can be compared to a subcritical boiling, where the main distinction is that the isothermal vaporization typical of subcritical fluids is replaced by a continuous non-equilibrium process that occurs over a narrow temperature range [10], as shown in Figure 2.4. As a result, the isobaric specific heat, c_p, presents a maximum and tends to infinity when approaching the critical point, as portrayed in Figure 2.5 for the nitrogen case.

Figure 2.5 depicts the evolution of density, ρ, and isobaric specific heat, c_p, with temperature, T, for nitrogen. In addition, pressure values from 4 to 6 MPa are represented using different line styles. The experimental data plotted is available from the NIST database [26]. Considering the critical properties of nitrogen, Figure 2.5 shows that the supercritical regime has indeed numerous states with noticeably different density and isobaric specific heat values.

While different isobaric plots converge to different density values for higher temperatures, they relatively converge to a similar density value for lower temperatures, thus portraying a liquid-like behavior.
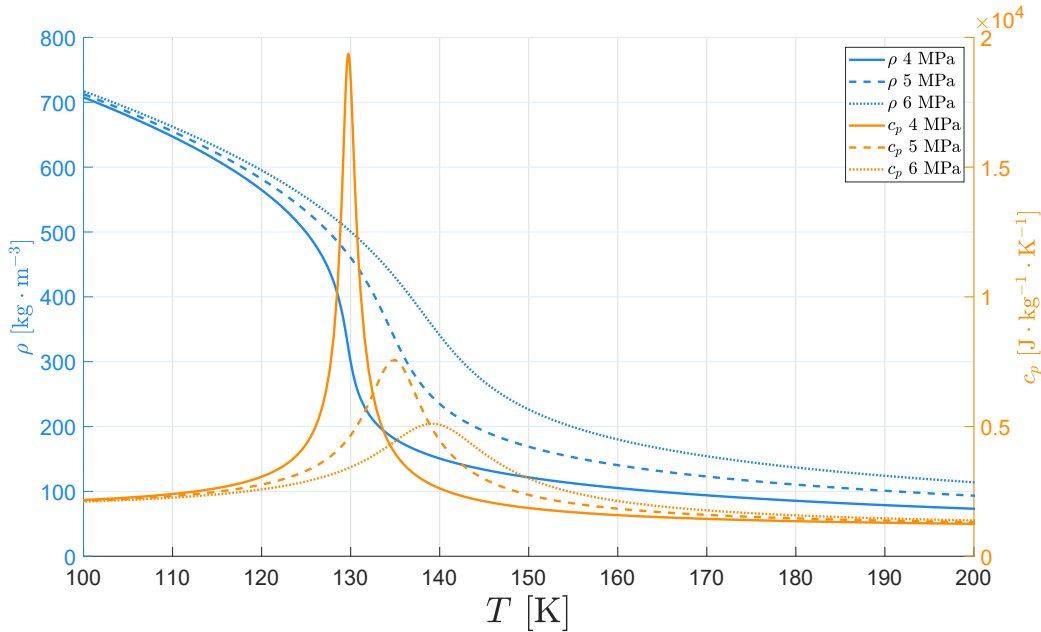
Figure 2.5: Plots of density and isobaric specific heat for nitrogen for pressures from 4 MPa to 6 MPa (data from the NIST database) [26].

The local maxima of the isobaric specific heat or the inflection point of density can be used as identifiers of the pseudo-boiling temperatures for different pressures, as shown in Figure 2.5. For the nitrogen case, it can be seen that for pressure values closer to the critical value of 3.40 MPa, the local maxima of the isobaric specific heat become more noticeable in addition to the value of $(\partial \rho / \partial T)_{\max}$.

Furthermore, in a quantitative investigation of the pseudo-boiling phenomenon carried by Banuti [32, 35], it is discovered that the isobaric specific heat distributions, besides suffering a displacement to higher temperatures, also widen and flatten with the pressure increase. Figure 2.5 depicts such behavior for the various pressures of 4, 5, and 6 MPa for the nitrogen case. In addition, the author discovered that, at a reduced pressure of $p_r = 3$, the local maxima of the isobaric specific heat have flattened, leading to the disappearance of the nonlinear transitions. Therefore, the significance of the noticeable fluid property changes of pseudo-boiling is thus limited to pressures $p_c < p < 3p_c$. Here, reduced pressure, p_r, is defined as the ratio of a given pressure p to the critical pressure, $p_r = p/p_c$. Figure 2.6 represents the extended $p - T$ diagram of the fluid, which compares the continuous but highly nonlinear variation between a liquid-like and a gas-like supercritical state to a subcritical vaporization process [36].
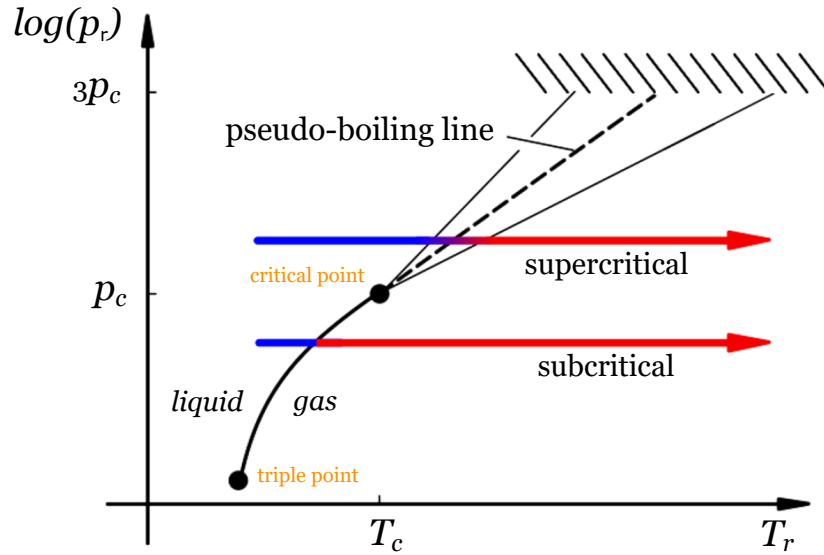
Figure 2.6: Extended $p - T$ diagram and supercritical injection characteristics (adapted from [36]).

Regarding the jet structure, supercritical fluids present distinct behaviors not observed at subcritical conditions. Figure 2.7 presents results obtained by Chehroudi et al. [37], which shows shadowgraphs of cryogenic liquid nitrogen jets injected into a gaseous nitrogen environment at a fixed supercritical temperature of 300 K. The pressures in Figure 2.7 are presented as reduced pressures, p_r, in relation to the critical pressure of nitrogen. From lower right to upper left in Figure 2.7, we have: $p_r = 0.23$ (a), 0.43 (b), 0.62 (c), 0.83 (d), 1.03 (e), 1.22 (f), 1.62 (g), 2.03 (h), 2.44 (i), 2.74 (j).
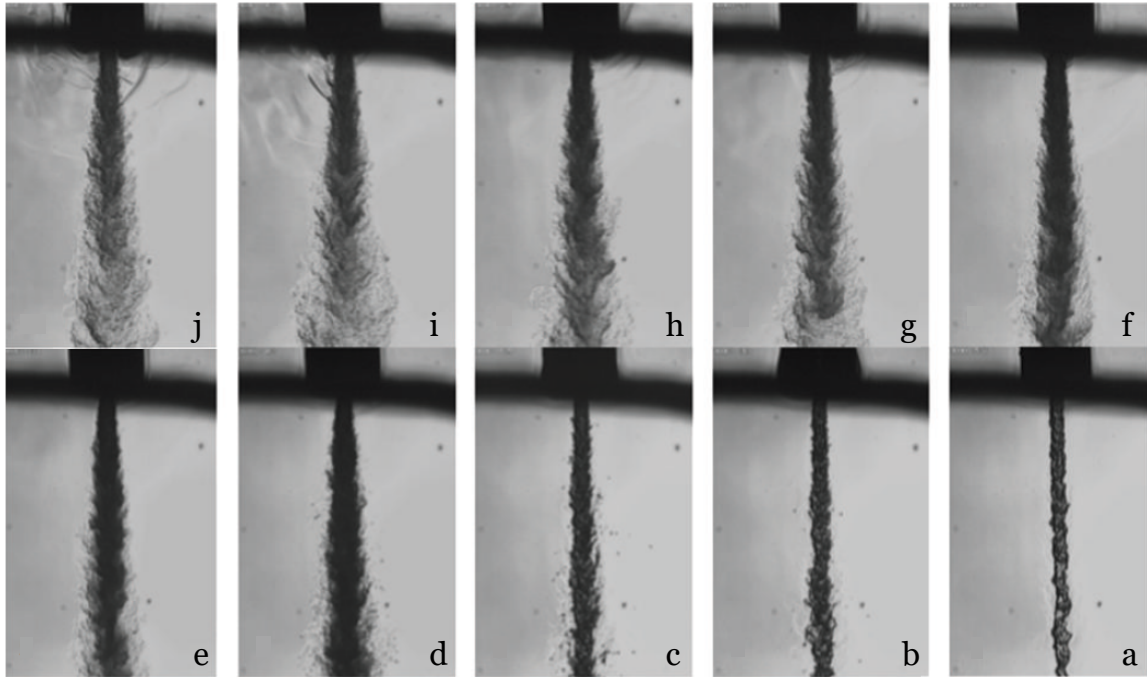
Figure 2.7: Liquid nitrogen jet injected into a nitrogen environment at a fixed supercritical temperature of 300 K varying sub- to supercritical pressures [37].

In frames (a) to (d), where the chamber pressure is subcritical, the jet presents a classical liquid spray appearance with the presence of the classical jet disintegration process at subcritical conditions. In line with the classical liquid jet breakup regimes described by Reitz and Bracco [38], surface instabilities grow downstream from the injector, where ligaments and droplets are ejected from the jet (see Figure 2.8a). According to Oschwald et al. [10], this behavior corresponds to the second wind-induced jet breakup mode described by Reitz and Bracco [38], where the theory of Rayleigh [39] regarding jet disintegration is appropriate for its description.

Figure 2.8 contains selected images from Figure 2.7 under additional magnification. The purpose of these images is to represent three injection cases under sub-, near-, and super-critical chamber pressures.

However, major structural and visual changes occur at $p_r = 1.03$ (e), as the nitrogen jet enters into a supercritical pressure and temperature environment, and noticeable changes in the interface are visible. As the critical point is crossed, ligaments and droplets are no longer visible, instead and as described by Chehroudi et al. [12], thread- or finger-like entities emerge from the jet but do not break up as before. Until this moment, the exact formation mechanism of these entities is not well known [40]. These thread- or finger-like structures, rather than breaking up in the classical mechanical theory view, dissolve at different distances from the dense core. Such entities are portrayed at a reduced pressure of $p_r = 1.22$ in Figure 2.8b.

Due to the density decrease, energy dissipation becomes dominant at this point. Schmitt et al. [41] performed a LES study where it is found that the large density gradients between the jet and the chamber environment affect the development of Kelvin-Helmholtz vortical structures and consequently the breakup. By comparing two different cases affected by these structures, the case with a higher density jet and therefore the higher density gradient inhibits the formation of Kelvin-Helmholtz vortical structures, thus delaying the breakup [40, 42]. This change in the mixing layer morphology is due to the combined effects of the surface tension being zero as the critical pressure is exceeded and the disappearance of latent heat as a result of the transition to supercritical pressures.

Ultimately, as the chamber pressure is further increased to a reduced value of $p_r = 2.74$, the length and thickness of the dense core decrease, and the jet start to have an appearance similar to that of subcritical gaseous jets. This resemblance is illustrated in Figure 2.7 in frames (g) to (j) and in Figure 2.8c. Regarding the droplets and ligaments production, these no longer occur, as well, by consequence, any additional classical liquid atomization [37].

(a) $p_r = 0.92$ (b) $p_r = 1.22$ (c) $p_r = 2.71$
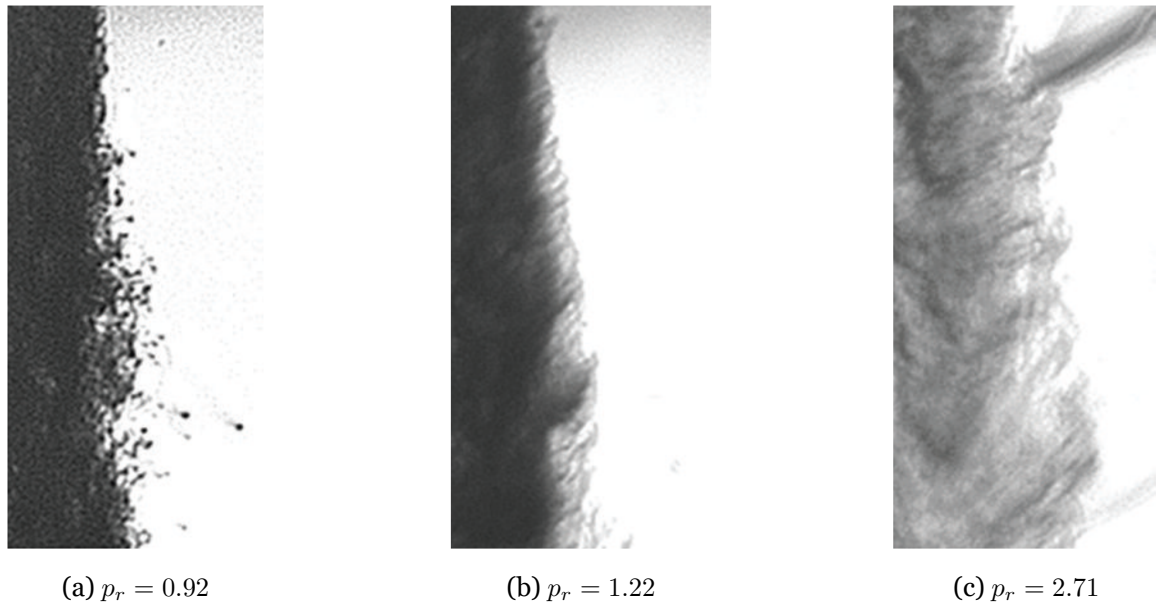
Figure 2.8: Magnified images of the jets in Figure 2.7 at their outer boundaries [37].

Ultimately, both the thermodynamic behavior and the breakup mechanisms preponderantly affect the jet structure. As the liquid-like nitrogen is injected into the chamber, its temperature suffers an increase as it begins to mix with the warmer nitrogen gas environment. As a consequence, the structure of the flow changes, and it can be divided into three characteristic regions: potential core, transition, and self-similar or fully developed region. This division is depicted in Figure 2.9.

Potential Core ⟶ | ⟵ *Transition Region* ⟶ | ⟵ *Self Similar Region*
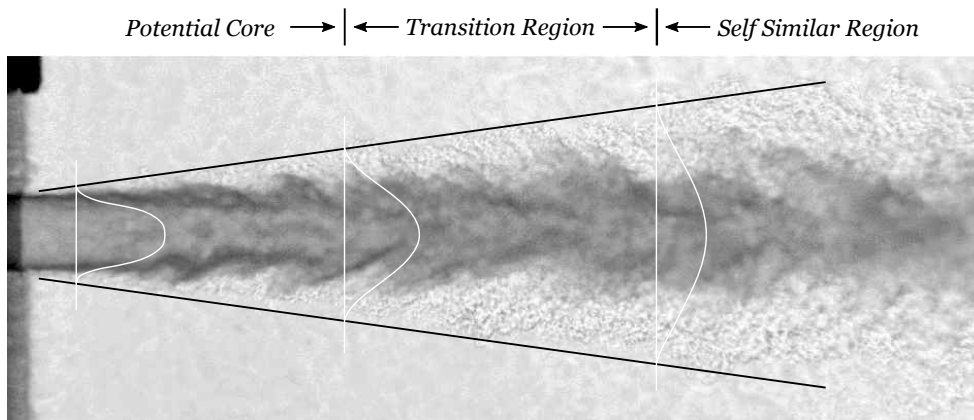
Figure 2.9: Jet mixing flow field (adapted from [43]).

Branam and Mayer [43] define the length of the potential core of the jet as the distance at which the centerline density remains relatively constant. This parameter has its importance, as it is an indicator of breakup efficiency. In the same matter, Banuti [35] compiles and compares four distinct equations in an attempt to predict this length, which is either based on the ratio between the densities of the liquid- and gas-like fluids or either assumes a constant value for any specific test geometry. After the potential core region, the jet is in a transitional

state where the turbulent and diffusive mixing present great relevance. As instabilities start to appear, dense pockets of liquid-like nitrogen are detached from the jet core and persist for a considerable length downstream. As a result, a strong density decrease occurs as density fluctuations suffer a notable increase [44, 45]. In this phenomenon, energy dissipation is noteworthy. Lastly, in the self-similar or fully developed region, the absolute value of flow variables can still change however their corresponding radial profiles are no longer varying in the axial direction.

In the experimental field, the flow structure is noticeable when resorting to axial and radial density distributions as well as to the jet spreading angle. These measurements, therefore, reveal great interest not only in experimental studies but also in the numerical field since they are used to validate the numerically obtained results.

In a study conducted by Banuti and Hannemann [36], the authors present substantial evidence for the introduction of a thermal disintegration mechanism as complementary to the classical mechanical breakup of supercritical jet disintegration. This formulation of a thermal disintegration mechanism is based on the pseudo-boiling theory and resolves certain existing discrepancies at the theoretical and computational domains, being unique for injection at supercritical pressures.

The rationale for this work is related to the fact that some experiments in quasi-isobaric supercritical injection raise discrepancies at the theoretical and the computational level. A constant value for the potential core length, expected in line with the mechanical breakup process, is not retrieved, instead, density is observed to decrease instantly as the jet enters the chamber. This behavior cannot be fully explained by a merely mechanical view of supercritical injection. However, the authors show that by introducing a thermal disintegration mechanism, the existing dilemma could be surpassed. The results indicate that this thermal disintegration mechanism may dominate classical mechanical breakup when heat transfer is considered taking place in the injector region and when the fluid state is sufficiently close to the pseudo-boiling point. In addition, the authors provide a procedure that allows capturing the referred subsided cores.

Figure 2.10 portrays how the jet disintegration process occurs depending on whether the injection takes place under sub- or supercritical conditions. Figure 2.10a, concerning subcritical injection, depicts how the instabilities in the shear layer form as waves with ever-increasing amplitude until they detach from the jet, forming droplets and ligaments. A mass stripping phenomenon is observed towards the jet centerline until the stream is no longer connected. The processes responsible for the rate at which this phenomenon occurs are atomization and vaporization. In contrast, in the supercritical injection case, the previous structures are replaced by the turbulent mixing of the supercritical fluid with the surrounding environment, as shown in Figure 2.10b. Since diffusion and mixing are faster processes than vaporization and in addition to the fact that surface tension inhibited breakup, supercritical mixing is predicted to occur at a higher rate and to be more effective.

(a) Subcritical classical breakup.

(b) Supercritical mixing-like disintegration.
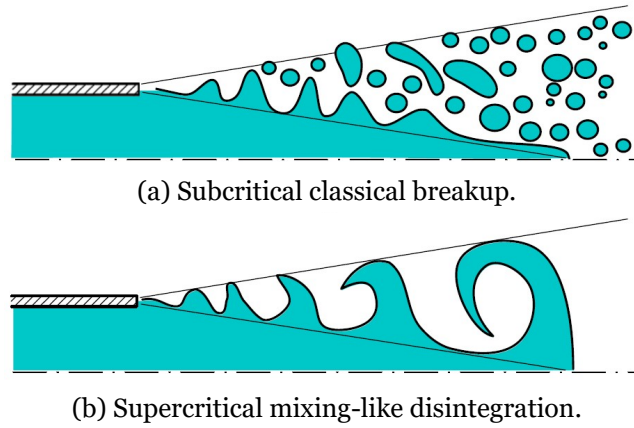
Figure 2.10: Jet appearance in sub- and supercritical injections [36].

Banuti and Hannemann also present a method in which it is possible to assess the existence of a constant density core through a thermodynamic analysis but only if the jet disintegration mechanism resort to a thermal mechanism formulation.

In order for a fluid to reach the pseudo-boiling state at constant pressure, the specific enthalpy of the fluid initially at a given temperature T_{init} needs to increase to reach T_{pb} by an amount

$$\Delta h_{pb} = \int_{T_{init}}^{T_{pb}} c_p(T) \, \mathrm{d}T \quad (2.1)$$

where the subscript pb represents the pseudo-boiling condition. If the fluid absorbs less heat than Δh_{pb}, the fluid will remain liquid-like. If not, if it has absorbed more heat, it becomes gas-like.

The power required to transform continuously, e.g., a jet with a mass flow $\dot{m}$, is given by

$$\Delta \dot{H}_{pb} = \dot{m} \int_{T_{init}}^{T_{pb}} c_p(T) \, \mathrm{d}T \quad (2.2)$$

This equation describes the power necessary to gasify a liquid jet.

If the mass flow $\dot{m}$ is known, equation (2.2) only depends on the integral of equation (2.1). Figure 2.11 depicts its evaluation for the nitrogen case for injection at different states. In addition, the critical temperature of nitrogen is also represented in orange. In a fluid injection context, it can then be considered that $T_{init} = T_{inj}$.
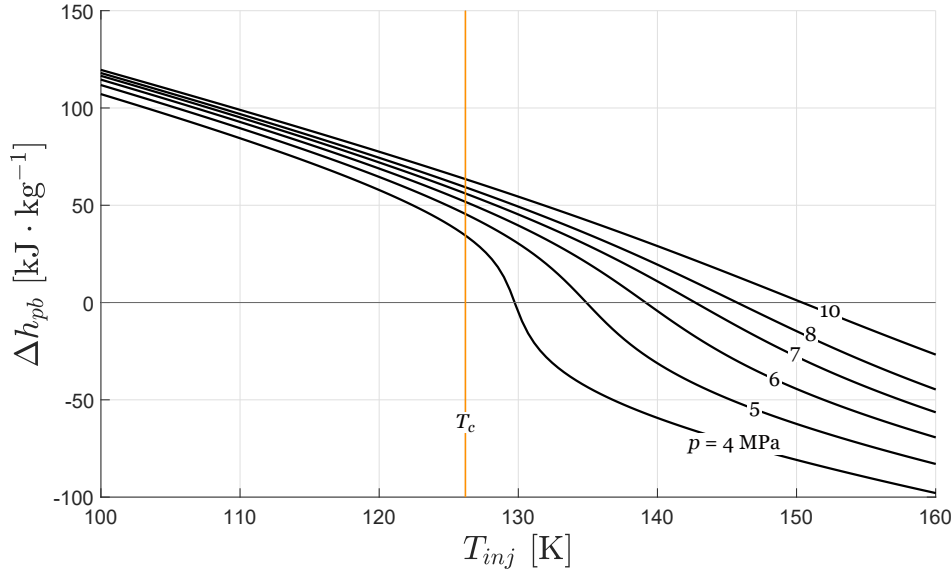
Figure 2.11: Required pseudo-vaporization enthalpy for the nitrogen case for injection at different states (data from the NIST database) [26].

Figure 2.11 has several intriguing properties. The plots for the various pressures intersect the ordinate zero line at the pseudo-boiling temperature, T_{pb}, of the corresponding pressure. In addition, it shows that, for low supercritical pressure values, fluid behavior near the pseudo-boiling temperature is considerably sensitive to temperature. In that case, a reduced temperature variation has a noticeable influence on the enthalpy of the fluid and, as a result, density. Additionally, no significant dependence of isobaric specific heat, i.e., the slope of the plot, on temperature, can be seen for a pressure of $10\,\mathrm{MPa}$, corresponding to a reduced pressure of $p_r = 2.9$. This fact strengthens the previously obtained results of Banuti [32, 35], which specify that pseudo-boiling effects are bounded superiorly at $p_r = 3$.

Figure 2.11 also clearly demonstrates the previously stated by Banuti [32] that the critical temperature is no longer the transition marker at supercritical pressures. As the steepest gradient is always centered near the pseudo-boiling temperature and no distinct changes arise at the critical temperature, T_{pb} is then the transition criterion. Lastly, another observation is that, for a given subcritical injection temperature, the Δh_{pb} value increases for increasing pressure values. Nevertheless, this is not obvious, as the local maxima of the isobaric specific heat are significantly reduced towards higher pressures (see Figure 2.5). However, such is distinctly compensated by the increasing pseudo-boiling temperature to be reached with increasing pressure.

In a case where injection occurs without significant pressure variation, the classical core length characterizes the quickness of the propagation of the expanding shear layer towards the centerline. Thus, as the potential core can be considered an enclosed region, this region is not yet influenced by the mechanical interaction. In the mechanical formulation framework, this mechanical interaction inevitably starts as the jet enters the chamber, and the interac-

tion occurs between the jet and the fluid in that environment. Thus, the potential core ends where the mixing between the injected fluid and the warmer environment has reached the centerline, thus triggering a rapid density drop. Therefore, density distributions that present a noticeable decrease upon entering the chamber cannot be explained by this formulation.

With the introduction of a thermal disintegration mechanism, based on the pseudo-boiling theory, this large drop in density can then be explained by the heat transfer to the super-critical fluid, not by the fluid entrainment. A large density gradient can be expected near the pseudo-boiling temperature. Therefore, pseudo-boiling reaching the centerline can then cause this drop. The main difference between the mechanical breakup and the thermal disintegration is that the latter may already occur in the injector, even before entering the chamber.

Banuti and Hannemann [36] then introduced a parameter Λ that assesses the possibility of thermal disintegration during the injection, defined as

$$\Lambda = \frac{\Delta \dot{H}_{pb}}{\dot{Q}} \quad (2.3)$$

This parameter compares the energy per unit time required to reach pseudo-boiling, $\Delta \dot{H}_{pb}$, to the supplied energy per unit time, $\dot{Q}$.

If a higher energy amount than Δh_{pb} is provided, the density core is terminated since fluid gasification is complete prior to the shear layers reaching the centerline, and a thermal breakup mechanism prevails ($\Lambda \ll 1$). If the supplied energy to the injected fluid is not enough, then mechanical breakup dominates ($\Lambda \gg 1$).

Unfortunately, there is no available data concerning heat transfer $\dot{Q}$ however, the $\Delta \dot{H}_{pb}$ comparison for different conditions can convey important information. Since, in the thermal disintegration framework, the existence of a constant density core should be associated with a high required thermal disintegration power $\dot{H}_{pb}$, a potential core/subsided core case classification could then be performed.

The ideal gas EoS is not appropriate to describe fluid behavior in the supercritical regime and thus must be replaced by more accurate formulations. As depicted in Figure 2.5, the strong density gradients have a tremendous impact on density evolution where, e.g., for a pressure level of $p = 4 \, \text{MPa}$, a 1 K increase at the temperature of 129 K leads to an approximately 21% reduction in density values.

Park [22] investigated liquid nitrogen jets at near-critical and supercritical pressures resorting to the Reynolds-averaged Navier-Stokes (RANS) and Large Eddy Simulation (LES) methods, where two real gas EoS are implemented to consider this departure from ideal gas behavior to real gas behavior. The results using the ideal EoS are then compared with those based on the two real gas EoS, the modified Soave-Redlich-Kwong (SRK) [46, 47] and Peng-

Numerical study on nitrogen injection at trans- and supercritical conditions

Robinson (PR) [48].

Although some discrepancies exist in the results of the SRK and PR EoS, the pseudo-boiling behavior is distinctly observed. As a result, it can be recognized that the real fluid EoS are adequately reproduced by the author's procedure. Regarding the performances of the three EoS, the results using the SRK and PR EoS are in good agreement with the experiment, while the ideal EoS presented lower density values without real fluid effects. Park also concluded that considering the predicted results, the choice of the suitable EoS plays a more preponderant role in the performance of the numerical simulations than numerics or turbulence modeling. The same conclusion is also verified in the LES results. The conclusion is consistent with the work of Kim et al. [27].

In a RANS-based numerical study conducted by Kim et al. [27], simulations are performed for cryogenic nitrogen jets at near-critical and supercritical pressures. To account for the non-ideal thermodynamic effects, the authors resorted to the modified SRK [46, 47] and PR [48] real gas EoS. Special attention is provided to sensitivity analyses for both EoS. The numerical results demonstrate that the present real gas formulation is capable of simulating the fundamental features of the cryogenic liquid nitrogen jets. The study also shows that the choice of a suitable real gas EoS is a preponderant factor for the performance of the simulations. In addition, the results show that the PR EoS predictions are in slightly better agreement with measured nitrogen density profiles than those of the SRK EoS.

In order to deal with this challenge in density evaluation, several real gas EoS can be applied, considering their respective advantages and inconveniences. These equations can be cubic EoS, multi-parameter EoS, or formulations based on the Helmholtz energy.

Characteristics like simplicity, computational efficiency, optimization, accuracy, or versatility are just some of the desired characteristics for the EoS. For example, some studies aim to develop optimized EoS for a given representative group of fluids with the same characteristics. For instance, the work of Span and Wagner [49] is an example where the resulting EoS is not the one that provides the best results for a single fluid. Instead, it is the one that provides the best results, in general, for the whole representative group.

Multi-parameter Equations of State can produce considerably accurate results however, they do not present a significant computational efficiency. To overcome this obstacle, an alternative is to resort to a multi-parameter EoS to calculate thermophysical properties before the numerical simulation begins and store these values in a library. The initial computational cost necessary to build this library for a broad range of temperature and pressure values, with the desired resolution, is considerable, but still, it proves rewarding since this work only has to be performed once. As a result, it allows an increasing accuracy with a lower associated computational cost since the values of interest are obtained before the computations, thus removing the need to calculate these properties in each iteration.

Numerical study on nitrogen injection at trans- and supercritical conditions

Associated to this alternative of solving the EoS before the computations, by generating lookup tables, complex multi-parameter EoS have been employed by Banuti et al. [50], using a modified Benedict-Webb-Rubin (MBWR) EoS [36] or formulations based on the Helmholtz energy [51] in a RANS-based study by Magalhães et al. [20].

Multi-parameter EoS can be developed through polynomial and exponential expansions in a data fitting method based on detailed and accurate data sets, where the coefficients multiplied by each term are specific to each fluid. In addition, these coefficients must be fitted through the available experimental data for the operating conditions in which the EoS is to be valid. The 32-term MBWR EoS [52] presents a relative error of density prediction smaller than 0.5% above and below the critical point. While Span and Wagner [49] propose a 12-term EoS with coefficients suitable for several substances, nitrogen included, Span et al. [51, 53] introduce a highly accurate 18-term EoS optimized directly for nitrogen. The main inconvenience of this approach is the computational cost, which can sometimes prohibit its usage.

Cubic Equations of State, such as the SRK EoS [46] and the PR EoS [48], are widely used in supercritical fluid flows modeling. Some arguments that contribute to this usage are based on their simplicity and compromise between accuracy and computational efficiency. Cubic EoS, hence this designation, only resort to three parameters for characterizing a given thermophysical parameter: the critical point temperature and pressure, and the acentric factor (a measure of the nonsphericity of the molecules). However, the accuracy of these cubic EoS and the respective operating range of the dependent variables must be monitored and considered when evaluating numerical simulations results.

This fact is justified by the results of Yang [54], where the author reports a considerable relative error of density prediction for the SRK EoS and PR EoS in the critical region. On the other hand, considering the same region, the noticeable performance of the multi-parameter MBWR EoS stands out due to its reduced maximum relative error. Whereas the SRK EoS and PR EoS register maximum relative errors of density prediction near 13% and 17%, respectively, the MBWR EoS only produces a 1.5% maximum relative error, at approximately $10\,\mathrm{MPa}$. Since these relative errors are not for nitrogen but oxygen instead and are registered at a very high reduced pressure ($p_r \approx 3$), they only serve as a warning. The Equation of State used in the present study and its formulation are presented in Section 3.6.

The CFD tools need to be validated by experimental results due to the absence of a general, efficient, and accurate mathematical model. Nevertheless, experimental studies have errors and uncertainties associated with the user, the equipment, or the involved techniques. Especially in the present case, where it resorts to supercritical fluids, the theoretical test conditions can be challenging to fulfill and maintain from an experimental point of view. As a result, the available measuring and visualization techniques become more restricted and, such errors can have a substantial impact on the legitimacy of measurements or visualizations. Therefore, when using numerical tools such as CFD to validate experimental results, it is essential to be aware of the phenomena involved to allow a critical and informed analysis

throughout the process.

The experimental studies presented in this section employ two of the principal standard diagnostic techniques: Shadowgraphy and Raman spectroscopy [17,55–58]. While the Shadowgraphy technique is used to provide qualitative information, as a consequence of its operating principles, it is most of the time complemented with Raman spectroscopy. While resorting to spontaneous Raman scattering, quantitative information, such as species concentration measurements, can be retrieved.

In the last decades, systematic research programs have been deployed to obtain a better insight into the injection of cryogenic liquids at sub- and supercritical pressures in laboratory quasi-isobaric experiments, with application to LREs. Two laboratories stood out in this exhaustive research, the Deutsches Zentrum für Luft- und Raumfahrt (DLR) in Germany and the Air Force Research Laboratory (AFRL) in the USA. Some examples of pioneering works at these laboratories are the ones of Oschwald and Schik [17], Oschwald and Micci [59] at the DLR, and Chehroudi et al. [60] at the AFRL. Since each laboratory has constructed unique facilities, such benefited the knowledge deepening. With the realization of different studies, knowledge will have been extended in a way that would not be possible individually for each laboratory. Concerning similar studies, it will have allowed conclusions to be drawn regarding the degree of corroboration of the results of each laboratory.

One of the most distinguished experimental studies is that of Mayer et al. [61]. The work of [61] on the injection of single species nitrogen at supercritical conditions has become one of the most noticeable sources of experimental data and a canonical set of test cases for the validation of numerical solvers whose objective is to predict supercritical fluid behavior. As a result, there are numerous examples of numerical solvers that resort to the experimental data of [61] for their validation [20–22, 27, 36, 40–42, 44, 45, 62–69].

In [61], the injection of a single liquid nitrogen jet at supercritical conditions into a chamber filled with gaseous nitrogen is studied. Several test cases are considered since the experimental conditions include different chamber pressure, velocity, and temperature levels. Then, the authors resort to Raman scattering to obtain density profiles, measure the axial evolution of density and evaluate the jet divergence angle. Following the nomenclature of this study, although attention has been paid to the evaluation of the computational models' suitability for the description of liquid- and gas-like supercritical behavior, usually, only cases 3 and 4 are simulated. Furthermore, the experimentally measured temperature values of [61] suggested the presence of significant heat transfer in the injector region that would affect jet development. Nevertheless, heat transfer inside the injector is regularly not considered in the simulations [40, 45, 62, 66, 68].

However, as [61] presented, the injection temperature measurements have some associated uncertainties. Since these present a strong influence on the jet development for the given operating conditions, this subject needs to be evaluated. In the experiments of Mayer et

al. [61], the experimental temperature was not controlled accurately due to the nonexistence of a temperature regulation system in the experimental setup. As a result, e.g., the temperature at the injector's exit could not be measured during the testing being instead measured during a separate measurement campaign. [61] presents in more detail the two approaches used in this temperature measurement process. Furthermore, despite evidence supporting the importance of accounting for heat transfer in the injector region, such is usually not considered.

The handling of the well-known closure problem through turbulence modeling is still one of the most prominent topics in numerical studies. Above a critical value of the Reynolds number (Re), the existence of advective terms in the governing equations leads to a chaotic solution due to their nonlinear behavior [70]. Hence, turbulence modeling is performed resorting to computational methods ranging from RANS to LES and Direct Numerical Simulation (DNS). However, the performance of a given computational method while predicting the behavior of flows under supercritical conditions is conditioned by various factors. Limitations such as the methods' performance associated with their respective backbone, where they aim to accurately capture the nonlinear behavior of the different thermophysical properties, particularly in the Widom line vicinity, to the existence of pertinent experimental data in the literature for their validation and mathematical models capable of predicting the flow behavior. In this sense, Bellan [71] presents some considerations on the various challenges that arise from the computations, from the associated consequences of employing different numerical and modeling approaches to the difficulties in establishing common initial and boundary conditions to the various sets of experimental data. As a result, in a quest for knowledge deepening in the description of supercritical fluid flows, several studies have employed RANS [18, 20–22, 27, 36, 72–75], LES [41, 42, 62, 63, 68, 76], and DNS [44, 45, 77, 78] methods in that sense.

Numerical study on nitrogen injection at trans- and supercritical conditions

Chapter 3

Mathematical Model

This chapter presents the mathematical model adopted in this study. Section 3.1 introduces the general form of a given conservation law. In Section 3.2, the governing equations are presented, including the conservation equations of mass, momentum, and energy. Section 3.3 reviews the approximations that have to be made to specific terms to simplify their resolution. Turbulence modeling is discussed in Section 3.4, while a brief review concerning near-wall modeling is made in Section 3.5. Section 3.6 reviews the adopted formulation to account for real gas behavior using a real gas EoS, while Section 3.7 presents the model implemented for describing the transport properties.

3.1   General form of a conservation law

To understand the concept of a conservation law, it may be worth considering a scalar quantity per unit volume U as a related property of a given flow.

Subsequently, it is necessary to define an arbitrary volume Ω, stationary in space, that has its boundaries delimited by an arbitrary closed surface S. This closed surface S is crossed by the fluid flow and can also be designated control surface; similarly, the arbitrary volume Ω can be named control volume. As it was called arbitrary, this control volume can be located anywhere in the flow domain and have any shape and size [70].

In order to write the conservation law associated with U, it is necessary to describe all quantities involved by doing a balance of the variation of U in the arbitrary domain Ω. The first term is related to the variation per unit time of the total amount of U in Ω and is given by

$$\frac{\partial}{\partial t} \int_{\Omega} U \, \mathrm{d}\Omega \quad (3.1)$$

Following that, it is necessary to write the term that expresses the amount of the quantity U that enters and leaves the domain. But, before the term is presented, it must be taken into account that the intensity of U changes from point to point in the domain due to the effect of quantities called fluxes.

A flux expresses the contribution from the surrounding points to the local value of U, therefore describing how the quantity U is transported by the flow. Flux is a quantity related to a conserved flow variable U and is characterized as the amount of U crossing the unit of surface per unit of time. Consequently, a flux is a directional quantity, being represented as a vector,

with a direction and an amplitude. Considering that flux is represented as a vector it is of interest to clarify that in the cases where this vector is parallel to the local surface, nothing will enter the domain. Therefore, only the component of the flux that is in the direction of the normal to the surface will enter the domain and consequently affect the rate of change of U. For that reason, there is the need to define a surface element vector $\mathrm{d}S_i$ that represents the local vector that is normal to the surface [70]. Additionally, this vector will be represented pointing along the outward normal to maintain the generally accepted convention.

Flux production has two different contributions. One contribution is related to the passive transport by the bulk of the fluid; the other is related to the molecular agitation that can exist even in cases where the fluid is at rest.

The first contributor, which is always present, is named advective flux F_A and is described as the passive transport of U by the flow and is defined as

$$F_{A_i} = U u_i \quad (3.2)$$

The second one is the diffusive flux F_D, characterized as the contribution that exists in fluids at rest as a consequence of the macroscopic effect of the molecular thermal agitation

$$F_{D_i} = -\Gamma \frac{\partial U}{\partial x} \quad (3.3)$$

where Γ is the diffusivity coefficient.

The result of the molecular motion appears as the tendency that a fluid has to the equilibrium and uniformity, given that different intensities of the considered quantity will originate changes in the spatial distribution to reach homogeneity. Therefore, the contribution of the diffusive component to the total flux is proportional to the gradient of the associated quantity since when uniformity is reached, this can not exist.

Considering all the domain and all the surface elements $\mathrm{d}S_i$ of the closed surface S, the net total contribution from the fluxes that cross the surface is given by

$$-\oint_S F_i \, \mathrm{d}S_i \quad (3.4)$$

The minus sign is used in this equation to preserve the convention that also considers the flux contribution as positive when it enters the domain.

Lastly, the term that represents the contributions from the sources of U is presented. The sources here are divided into two parts, volume and surface sources

$$\int_\Omega Q_{V_i} \, \mathrm{d}\Omega + \oint_S Q_{S_i} \, \mathrm{d}S_i \quad (3.5)$$

Therefore, the general integral form of the conservation law for the scalar quantity per unit volume U after applying the Gauss theorem is given by

$$\int_{\Omega} \frac{\partial U}{\partial t} \, \mathrm{d}\Omega + \int_{S} F_i \, \mathrm{d}S_i = \int_{\Omega} Q_{V_i} \, \mathrm{d}\Omega + \int_{S} Q_{S_i} \, \mathrm{d}S_i \quad (3.6)$$

In addition, it can be written as

$$\int_{\Omega} \frac{\partial U}{\partial t} \, \mathrm{d}\Omega + \int_{S} (F_i - Q_{S_i}) \, \mathrm{d}S_i = \int_{\Omega} Q_{V_i} \, \mathrm{d}\Omega \quad (3.7)$$

In the last equation, the flux and the surface sources terms were grouped since the last one has the same effect on the system as the flux term. Consequently, the term $(F_i - Q_{S_i})$ can be considered as an effective flux.

Equation (3.6) has some noteworthy properties. The first one is that this equation is valid for any fixed surface S and volume Ω. Secondly, the internal variation of U, when no volume sources exist, depends only on the flux contribution through the surface S and not on the flux values inside the volume Ω. Another property is that the fluxes are not written under the form of a derivative or gradient operator and may, for that reason, be discontinuous [70].

These properties are considered important, with particular attention to the second one since it will be required that this property is still valid after discretization, thus guaranteeing the fulfillment of the conservation law at the discrete level. When such a property is verified, it is said that we are in the presence of a conservative numerical scheme. For example, when dealing with a case of an internal flow calculation, this property is essential to ensure mass conservation in all regions at study.

3.2   Governing equations

3.2.1   Mass conservation

The mass conservation law consists of a relation of kinematic nature, i.e., it does not depend on the nature of the fluid nor on the forces that act on it. This law conveys that mass cannot be destroyed nor be created in a fluid system. Therefore, no diffusive flux exists for the mass transport, meaning that the only term present is the one concerning advection.

Defining the advective flux as

$$F_A = \rho u_i \quad (3.8)$$

and in absence of external mass sources, the general integral mass conservation equation is

given by

$$\int_\Omega \frac{\partial \rho}{\partial t}\, d\Omega + \int_\Omega \frac{\partial}{\partial x_i}(\rho u_i)\, d\Omega = 0 \quad (3.9)$$

Equation (3.9) is also known as the continuity equation.

3.2.2 Momentum conservation

Momentum is a vector quantity characterized as the product of mass and velocity. When expressed per unit of volume, momentum appears as the product of density and velocity

$$U = \rho u_j \quad (3.10)$$

The momentum conservation law is the expression of the generalized Newton law, defining the equation of motion of a fluid.

In resemblance to the mass conservation equations, the only contribution to the flux production is due to advective nature. Since the conservative property is a vector quantity, the advective flux term will appear under the form of a tensor and is defined by

$$F_{A_i} = \rho u_j u_i \quad (3.11)$$

Regarding the other terms present in the conservation equation, it is necessary to identify the sources that affect momentum. The sources for the variation of momentum in a physical system are the forces acting on it. In this work, those are represented, per unit mass, as the external volume forces f_{ext} and the internal forces f_{int}.

While the external volume forces per unit volume ρf_{ext} are associated with Q_V, the internal forces per unit volume ρf_{int} are associated with Q_S. This last relation is because, since internal forces cancel two per two in every point inside the volume as a result of Newton's third law of motion, only the internal forces acting on the points of the surface S contribute. This phenomenon happens because the internal forces acting on these points do not have an opposite counterpart within the volume Ω.

As a consequence, the surface source term is given by

$$Q_{S_i} = \sigma_{ij} \quad (3.12)$$

where σ_{ij} is the total internal stress tensor being defined by

$$\sigma_{ij} = -p\delta_{ij} + \tau_{ij} \quad (3.13)$$

Additionally, in this last equation, τ_{ij} represents the viscous shear stress tensor which can be

written in its most general form

$$\tau_{ij} = 2\mu s_{ij} + \zeta \frac{\partial u_k}{\partial x_k} \delta_{ij} \quad (3.14)$$

where s_{ij} represents the strain-rate tensor, μ the dynamic viscosity, and ζ the second viscosity coefficient.

The strain-rate tensor is given by

$$s_{ij} = \frac{1}{2}\left(\frac{\partial u_i}{\partial x_j} + \frac{\partial u_j}{\partial x_i}\right) \quad (3.15)$$

Therefore, the general momentum conservation or Navier-Stokes equations in their integral form is given by

$$\int_\Omega \frac{\partial}{\partial t}(\rho u_i)\, d\Omega + \int_\Omega \frac{\partial}{\partial x_j}(\rho u_j u_i)\, d\Omega = \int_\Omega \rho f_i\, d\Omega - \int_\Omega \frac{\partial}{\partial x_i}(p)\, d\Omega + \int_\Omega \frac{\partial}{\partial x_j}(\tau_{ij})\, d\Omega \quad (3.16)$$

3.2.3 Energy conservation

While studying a fluid, its total energy is defined as the sum of two terms. The first term consists of the internal energy of the fluid, while the second represents its kinetic energy per unit mass

$$E = e + \frac{u_i u_i}{2} \quad (3.17)$$

If the conservative property is $U = \rho E$, then the advective flux contribution of energy is

$$F_{A_i} = \rho E u_i \quad (3.18)$$

In addition, the diffusive flux contribution, under the form of Fourier's law of heat conduction, is given by

$$F_{D_i} = \frac{\partial q_i}{\partial x_i} = -\kappa \frac{\partial T}{\partial x_i} \quad (3.19)$$

where T is the absolute temperature and κ the thermal conductivity coefficient defined by

$$\kappa = \rho c_p \alpha \quad (3.20)$$

In equation 3.20, α represents the thermal diffusivity coefficient that can be used to introduce the Prandtl number (Pr), defined by

$$\mathrm{Pr} = \frac{\mu c_p}{\kappa} = \frac{\upsilon}{\alpha} \quad (3.21)$$

where υ is the kinematic viscosity given by μ/ρ. The Prandtl number can be interpreted as the ratio of momentum to thermal diffusivity.

To conclude the writing of the conservation equation, a distinction has to be made between the volume and surface sources. Regarding the volume sources' contribution to energy variation, it appears as the sum of the work of the volume forces and the heat sources other than conduction, the latter represented by q_H

$$Q_{V_i} = \rho u_i f_i + q_H \quad (3.22)$$

Lastly, the surface sources appear as the consequence of the work done on the fluid by the internal shear stresses acting on the surface of the volume. In the absence of external surface heat sources, the surface sources are represented by

$$Q_{S_i} = u_i \sigma_{ij} = -u_i p \delta_{ij} + u_i \tau_{ij} \quad (3.23)$$

With all the above terms considered, the energy conservation equation in its integral form is given by

$$
\int_\Omega \frac{\partial}{\partial t}(\rho E)\, \mathrm{d}\Omega + \int_\Omega \frac{\partial}{\partial x_j}(\rho E u_j)\, \mathrm{d}\Omega = \; -\int_\Omega \frac{\partial q_j}{\partial x_j}\, \mathrm{d}\Omega + \int_\Omega (\rho u_i f_i + q_H)\, \mathrm{d}\Omega - \\
-\int_\Omega \frac{\partial}{\partial x_j}(u_i p)\, \mathrm{d}\Omega + \int_\Omega \frac{\partial}{\partial x_j}(u_i \tau_{ij})\, \mathrm{d}\Omega \quad (3.24)
$$

It is also possible to introduce the definition of total enthalpy H in the last equation resorting to the following relation

$$H = e + \frac{p}{\rho} + \frac{u_i u_i}{2} = h + \frac{u_i u_i}{2} = E + \frac{p}{\rho} \quad (3.25)$$

The energy conservation law is also referred to as the expression of the first principle of Thermodynamics.

3.3   Approximations

The conservation equations obtained in Sections 3.2.1, 3.2.2, and 3.2.3 cannot be discretized straightaway. In addition, it has resorted to a statistical approach since turbulence can be described as random fluctuations of the several flow properties. As a result, we follow the method introduced in 1895 by Osborn Reynolds, where he developed a procedure where all quantities are defined as the sum of mean and fluctuating terms. According to this method, averages are then applied to the governing equations.

Nevertheless, after applying such a procedure to the governing equations, additional unknown quantities appear, which will translate to having more unknowns than transport equations, i.e., the closure problem. The solution to this problem can be achieved using turbu-

lence modeling, where new transport equations are introduced to represent the previous un-known quantities, thus establishing a sufficient number of equations for all of the involved unknowns.

In this section, two methods regarding the governing equations averaging are presented. Regarding the Reynolds averaging techniques, we introduce a brief explanation of two of its forms: the ensemble and the time averages. Subsequently, the Favre averaging and the Favre averaged equations, adequate for variable density flows, are presented.

3.3.1 Reynolds averaging

Regarding the averaging concepts introduced by Reynolds, several formulations exist how-ever, the most relevant when dealing with turbulence models are the time average, the spatial average, and the ensemble average [79]. The latter appears as one of the most general forms of Reynolds averaging suitable for, e.g., flows that decay in time and is defined as

$$F_E(x,t) = \lim_{N \to \infty} \left[\frac{1}{N} \sum_{n=1}^{N} f_n(x,t) \right] \quad (3.26)$$

where $f_n(x,t)$ is the instantaneous flow variable in the nth experiment of f and N represents the number of identical experiments. That is to say, it consists of the average of the instan-taneous values of the property at a given point in space x and time t over a large number of repeated identical experiments.

Concerning time-averaging, when applied to stationary random cases, it can be defined as

$$F_T(x) = \lim_{\Delta t \to \infty} \left[\frac{1}{\Delta t} \int_t^{t+\Delta t} f(x,t) \, \mathrm{d}t \right] \quad (3.27)$$

The assumption in statistical mechanics where time averages of macroscopic variables are equivalent to ensemble averages, for stationary random processes, in the limit as $\Delta t \to \infty$, is known as the ergodic hypothesis [71, 80].

3.3.2 Reynolds time-averaging

The Reynolds time-averaging consists of decomposing, in time, a quantity as the sum of two terms, a mean term and a fluctuating term, respectively

$$\phi_i = \overline{\phi}_i + \phi_i' \quad (3.28)$$

where

$$\overline{\phi}_i = \lim_{\Delta t \to \infty} \left[\frac{1}{\Delta t} \int_t^{t+\Delta t} \phi_i \, \mathrm{d}t \right] \quad (3.29)$$

and

$$\overline{\phi_i'} = \lim_{\Delta t \to \infty} \left[\frac{1}{\Delta t} \int_t^{t+\Delta t} (\phi_i - \overline{\phi_i}) \ \mathrm{d}t \right] = 0 \quad (3.30)$$

A noteworthy relation of the Reynolds averaging is that the averaging in time of the spatial variation of a certain quantity is equal to the spatial variation of the mean quantity, i.e.,

$$\overline{\frac{\partial \phi_i}{\partial x_j}} = \lim_{\Delta t \to \infty} \left[\frac{1}{\Delta t} \int_t^{t+\Delta t} \frac{\partial \phi_i}{\partial x_j} \ \mathrm{d}t \right] = \frac{\partial}{\partial x_j} \left[\lim_{\Delta t \to \infty} \left(\frac{1}{\Delta t} \int_t^{t+\Delta t} \phi_i \ \mathrm{d}t \right) \right] = \frac{\partial}{\partial x_j} (\overline{\phi_i}) \quad (3.31)$$

therefore,

$$\overline{\frac{\partial \phi_i}{\partial x_j}} = \frac{\partial \overline{\phi_i}}{\partial x_j} \quad (3.32)$$

Another remarkable relation is that the averaging in time of a product of two quantities is not necessarily equal to the product of each mean, i.e.,

$$\overline{\phi_i \phi_j} = \overline{\left(\overline{\phi_i} + \phi_i' \right) \left(\overline{\phi_j} + \phi_j' \right)} = \overline{\overline{\phi_i} \ \overline{\phi_j}} + \overline{\overline{\phi_i} \phi_j'} + \overline{\overline{\phi_j} \phi_i'} + \overline{\phi_i' \phi_j'} \quad (3.33)$$

Using the relation of the equation (3.30) and the following property

$$\overline{\overline{\phi_i \phi_j}} = \overline{\phi_i} \ \overline{\phi_j} \quad (3.34)$$

we have

$$\overline{\phi_i \phi_j} = \overline{\phi_i} \ \overline{\phi_j} + \overline{\phi_i' \phi_j'} \quad (3.35)$$

3.3.3   Favre averaging

This work adopted the simplification of an incompressible but variable density approach. This simplification was a hypothesis investigated by Barata et al. [18] based on the results of Chehroudi et al. [12], where supercritical flows revealed a quantitative similarity to gas jet-like behavior. Considering these similarities, [18] studied the hypothesis of using the same mathematical and numerical models for gaseous flows in numerical simulations involving supercritical flows. The obtained results for different supercritical density ratios revealed a good agreement with the available experimental data for liquid/gaseous jets and mixing layers.

To deal with the incompressible but variable density conditions, characteristic of the test cases at study, the Reynolds time-averaging technique is replaced by the Favre averaging method. Thus, the density-weighted conservation equations are presented to introduce the density variation effects.

If the condition $\rho = \overline{\rho} + \rho'$ was added to the Reynolds time-averaging procedure that would

lead to the appearance of several terms involving products of fluctuations between density and other variables. Consequently, that would increase the complexity of determining suitable closure approximations (additional models). For that purpose, Favre averaging is used to rule out the density fluctuations from the averaged equations while maintaining their effect on the turbulence.

The Favre averaging decomposes a quantity as the sum of two terms, a density-weighted average term and a density-weighted fluctuation term, being respectively

$$\phi_i = \tilde{\phi}_i + \phi_i'' \quad (3.36)$$

Analogously to equation (3.29), $\tilde{\phi}_i$ is defined as

$$\tilde{\phi}_i = \frac{1}{\bar{\rho}} \lim_{\Delta t \to \infty} \left[\frac{1}{\Delta t} \int_t^{t+\Delta t} (\rho \phi_i) \, \mathrm{d}t \right] \quad (3.37)$$

where $\bar{\rho}$ represents the Reynolds time-averaged density.

Another notable definition of $\tilde{\phi}_i$ can also be presented while resorting to some properties of Favre averaging, such as

$$\overline{\rho \phi_i} = \overline{\rho(\tilde{\phi}_i + \phi_i'')} = \overline{\rho \tilde{\phi}_i} + \overline{\rho \phi_i''} = \bar{\rho} \tilde{\phi}_i + \overline{\rho \phi_i''} \quad (3.38)$$

and

$$\overline{\rho \phi_i''} = 0 \quad (3.39)$$

what leads to

$$\overline{\rho \phi_i} = \bar{\rho} \tilde{\phi}_i$$
$$\tilde{\phi}_i = \frac{\overline{\rho \phi_i}}{\bar{\rho}} \quad (3.40)$$

where the overbar notation defines a Reynolds time average.

On the other side, while resorting to the Reynolds time-averaging, we would have

$$\overline{\rho \phi_i} = \bar{\rho} \bar{\phi}_i + \overline{\rho' \phi_i'} \quad (3.41)$$

That is, the use of Reynolds time-averaging would lead to the appearance of an additional term which would lead to several other operations, thus increasing the complexity of expressions when applied to governing equations.

Numerical study on nitrogen injection at trans- and supercritical conditions

Another rule of Favre averaging consists of

$$\overline{\phi_j \tilde{\phi}_i} = \overline{\phi_j \left(\frac{\overline{\rho \phi_i}}{\overline{\rho}} \right)} = \overline{\phi}_j \left(\frac{\overline{\rho \phi_i}}{\overline{\rho}} \right) = \overline{\phi}_j \tilde{\phi}_i \quad (3.42)$$

In addition, analogously to that presented in equation (3.33), if Favre averaging is used, we have

$$\overline{\rho \phi_i \phi_j} = \overline{\rho \left(\tilde{\phi}_i + \phi_i'' \right) \left(\tilde{\phi}_j + \phi_j'' \right)} = \overline{\rho \tilde{\phi}_i \tilde{\phi}_j + \rho \tilde{\phi}_i \phi_j'' + \rho \tilde{\phi}_j \phi_i'' + \rho \phi_i'' \phi_j''}$$
$$= \overline{\rho} \tilde{\phi}_i \tilde{\phi}_j + \overline{\rho \phi_j''} \tilde{\phi}_i + \overline{\rho \phi_i''} \tilde{\phi}_j + \overline{\rho \phi_i'' \phi_j''} \qquad (3.43)$$
$$= \overline{\rho} \tilde{\phi}_i \tilde{\phi}_j + \overline{\rho \phi_i'' \phi_j''}$$

After applying the Favre averaging technique to equations (3.9), (3.16), and (3.24), we have, respectively

$$\int_{\Omega} \frac{\partial \overline{\rho}}{\partial t} \, d\Omega + \int_{\Omega} \frac{\partial}{\partial x_i} \left(\overline{\rho} \tilde{u}_i \right) d\Omega = 0 \quad (3.44)$$

$$\int_{\Omega} \frac{\partial}{\partial t} \left(\overline{\rho} \tilde{u}_i \right) d\Omega + \int_{\Omega} \frac{\partial}{\partial x_j} \left(\overline{\rho} \tilde{u}_i \tilde{u}_j \right) d\Omega = -\int_{\Omega} \frac{\partial}{\partial x_i} \left(\overline{p} \right) d\Omega + \int_{\Omega} \frac{\partial}{\partial x_j} \left(\overline{\tau}_{ji} + t_{ij} \right) d\Omega + \int_{\Omega} \left(\overline{\rho} f_i \right) d\Omega \quad (3.45)$$

$$\int_{\Omega} \frac{\partial}{\partial t} \left(\overline{\rho} \tilde{E} \right) d\Omega + \int_{\Omega} \frac{\partial}{\partial x_j} \left(\overline{\rho} \tilde{u}_j \tilde{H} \right) d\Omega = \int_{\Omega} \frac{\partial}{\partial x_j} \left(-q_j - q_{t_j} + \overline{\tau_{ji} u_i''} - \overline{\frac{1}{2} \rho u_i'' u_i'' u_j''} \right) d\Omega + $$
$$+ \int_{\Omega} \frac{\partial}{\partial x_j} \left[\tilde{u}_i \left(\overline{\tau}_{ij} + t_{ij} \right) \right] d\Omega \qquad (3.46)$$

While equation (3.44) is identical to its laminar counterpart, equation (3.45) differs only by the appearance of the average pressure term, $\overline{p}$, substituting the instant pressure term, p, and the appearance of the Favre-averaged Reynolds stress tensor

$$t_{ij} = -\overline{\rho u_i'' u_j''} \quad (3.47)$$

In addition, the viscous shear stress tensor from equation (3.14) is averaged to

$$\tilde{\tau}_{ij} = 2\mu \tilde{s}_{ij} + \zeta \frac{\partial \tilde{u}_k}{\partial x_k} \delta_{ij} \quad (3.48)$$

where the mean strain-rate tensor, $\tilde{s}_{ij}$, is

$$\tilde{s}_{ij} = \frac{1}{2} \left(\frac{\partial \tilde{u}_i}{\partial x_j} + \frac{\partial \tilde{u}_j}{\partial x_i} \right) \quad (3.49)$$

Regarding equation (3.46), several additional terms appear, each of which representing a

noticeable physical process or property, such as $\tilde{E}$ and $\tilde{H}$, defined by

$$\tilde{E} = \tilde{e} + \frac{1}{2}\tilde{u}_i\tilde{u}_i + k \quad (3.50)$$

$$\tilde{H} = \tilde{h} + \frac{1}{2}\tilde{u}_i\tilde{u}_i + k \quad (3.51)$$

where k is the turbulent kinetic energy per unit volume

$$\bar{\rho}k = \frac{1}{2}\overline{\rho u_i'' u_i''} \quad (3.52)$$

Additionally, the turbulent heat flux, q_{t_j}, is also defined as

$$q_{t_j} = \overline{\rho u_j'' h''} \quad (3.53)$$

Through an analysis of equations (3.45) and (3.46), it is possible to notice the presence of double and triple correlations, this being a consequence of the averaging technique. The Reynolds stress tensor alone, defined in equation (3.47), adds three additional independent variables to the previous four equation system evidencing that the system is still not closed. This fact reiterates the closure problem. For that reason, there is still the need to define some terms, which is the purpose of the following section.

3.3.4 Closure approximations

Terms such as t_{ij}, q_j, q_{t_j}, and $\overline{\tau_{ji}u_i''}$ from equations (3.45) and (3.46) remain undefined.

In what the definition of the Reynolds stress tensor concerns, one of the most used approximations is the Boussinesq hypothesis. Boussinesq, in 1877, presented the notion of eddy or turbulent viscosity, μ_t, which accounts for momentum transport by turbulent eddies, relating t_{ij} to τ_{ij}. The concept was based on the resemblance of the random eddy motion of groups of particles and the random motion of molecules in a gas, where molecules collide transferring momentum in the process. Hence, momentum transfer by eddies in turbulent flows is analogous to molecular momentum diffusion. Consequently, equation (3.48) assumes the form

$$t_{ij} \approx 2\mu_t\left(\tilde{s}_{ij} - \frac{1}{3}\frac{\partial \tilde{u}_k}{\partial x_k}\delta_{ij}\right) - \frac{2}{3}\bar{\rho}k\delta_{ij} \quad (3.54)$$

When using this equation, it should be noted that the terms of the tensor with $i \neq j$ are modeled through μ_t, while the trace of t_{ij} is defined according to equation (3.47), thus involving the specific turbulent kinetic energy, that is given by

$$t_{ii} = -\overline{\rho u_i'' u_i''} = -2\bar{\rho}k \quad (3.55)$$

Bearing these considerations in mind, turbulence models can concentrate on the calculation of μ_t and k.

Regarding the laminar and turbulent heat transport terms, q_j and q_{t_j}, these are written using Fourier's law of heat conduction, presented in equation (3.19), resulting in

$$q_j = -\frac{\mu c_p}{\mathrm{Pr}} \frac{\partial \tilde{T}}{\partial x_j} = -\frac{\mu}{\mathrm{Pr}} \frac{\partial \tilde{h}}{\partial x_j} \quad (3.56)$$

$$q_{t_j} = -\frac{\mu_t c_p}{\mathrm{Pr}_t} \frac{\partial \tilde{T}}{\partial x_j} = -\frac{\mu_t}{\mathrm{Pr}_t} \frac{\partial \tilde{h}}{\partial x_j} \quad (3.57)$$

where Pr_t is the turbulent Prandtl number, defined as the ratio of turbulent kinematic viscosity to turbulent thermal diffusivity, i.e.,

$$\mathrm{Pr}_t = \frac{\nu_t}{\alpha_t} \quad (3.58)$$

Lastly, the term $\overline{\tau_{ji} u_i''}$ is coupled with $-\overline{\frac{1}{2}\rho u_i'' u_i'' u_j''}$, and consequently, the molecular diffusion and turbulent transport term is modeled by

$$\overline{\tau_{ji} u_i''} - \overline{\frac{1}{2}\rho u_i'' u_i'' u_j''} = \left(\mu + \frac{\mu_t}{\sigma_k}\right) \frac{\partial k}{\partial x_j} \quad (3.59)$$

where σ_ϕ is the Pr_t for any variable ϕ.

Introducing the above approximations in equation (3.46), we have

$$\int_\Omega \frac{\partial}{\partial t}\left(\bar{\rho}\tilde{E}\right)\mathrm{d}\Omega + \int_\Omega \frac{\partial}{\partial x_j}\left(\bar{\rho}\tilde{u}_j \tilde{H}\right)\mathrm{d}\Omega = \int_\Omega \frac{\partial}{\partial x_j}\left[\left(\frac{\mu}{\mathrm{Pr}} + \frac{\mu_t}{\mathrm{Pr}_t}\right)\frac{\partial \tilde{h}}{\partial x_j} + \left(\mu + \frac{\mu_t}{\sigma_k}\right)\frac{\partial k}{\partial x_j}\right]\mathrm{d}\Omega +$$
$$+ \int_\Omega \frac{\partial}{\partial x_j}\left[\tilde{u}_i\left(\bar{\tau}_{ij} + t_{ij}\right)\right]\mathrm{d}\Omega \quad (3.60)$$

The system of governing equations is still not closed at this stage. Attention has to be taken yet of μ_t, k, Pr_t, and in defining material properties.

3.4   Turbulence modeling

Regarding turbulence modeling, there are several models each using different approximations or assumptions. Turbulence models can be grouped into two main groups: first-order and second-order models.

Concerning first-order models, these are based on the Boussinesq hypothesis and therefore are also named eddy viscosity models. First-order models include zero, one, and two-equation models. In turbulence modeling, when the concept of an n-equation model is used it portraits the group of n additional transport equations apart from those representing the conservation of mass, momentum, and energy required to solve the closure problem [79].

Numerical study on nitrogen injection at trans- and supercritical conditions

In 1925, Prandtl introduced the mixing length hypothesis, inspired by an analogy of the mean free path of a gas. Prandtl also suggested a straightforward method for computing the eddy or turbulent viscosity in terms of the mixing length. That resulted from the observation of a simplified model for turbulent motion where fluid particles agglutinate into lumps that hang together and move as one entity. As a result, Prandtl assumed that the x-momentum of the fluid conserves its value for a given length in the y direction, being represented as l_{mix}. Here, l_{mix} represents the mixing length defined as a characteristic length scale of the turbulent flow that differs from each flow geometry as does the characteristic velocity. These scales need to be defined *a priori*.

Zero-equation models use algebraic relations to relate the turbulent fluctuating correlations to the mean flow field quantities. It is also assumed that the local rate of turbulence production is equal to the rate of turbulence dissipation. In these models, the length and velocity scales are specified in terms of the mean flow, therefore assuming an equilibrium between mean motion and turbulence. However, the physical effect of the past history of the flow is not included in these algebraic models ('convection of turbulence').

Nevertheless, one and two-equation models take the previous effect into account by employing transport equations for past history-dependent variables of the flow that can represent a length and a velocity scale. These transport equations may be derived from the Navier-Stokes equation, where when one such equation is employed, we refer to it as a one-equation model whereas when two transport equations are used, it is said to be a two-equation model.

With regard to second-order models, its central concept consists of deriving a transport equation for t_{ij} that is coupled with an equation for either the turbulent dissipation rate, ε, or the specific dissipation rate, ω, instead of resorting to the Boussinesq hypothesis.

The two-equation turbulence model used in the present work defines the velocity scale by resorting to the turbulent kinetic energy, thus including non-local and flow history in the turbulent viscosity considerations. Therefore, the corresponding transport equation for k is based on the transport equation of the trace of the Reynolds stress tensor, presented in equation (3.55), resulting in

$$
\frac{\partial}{\partial t}\left(\overline{\rho}k\right) + \frac{\partial}{\partial x_j}\left(\overline{\rho}\tilde{u}_j k\right) = t_{ij}\frac{\partial \tilde{u}_i}{\partial x_j} - \overline{\tau_{ji}\frac{\partial u_i''}{\partial x_j}} + \frac{\partial}{\partial x_j}\left(\overline{\tau_{ji}u_i''} - \overline{\frac{1}{2}\rho u_i'' u_i'' u_j''} - \overline{p'u_j''}\right) - \\
- \overline{u_i''}\frac{\partial \overline{p}}{\partial x_i} + \overline{p'\frac{\partial u_i''}{\partial x_i}}
\tag{3.61}
$$

where the averaged dissipation rate is given by

$$
\overline{\rho}\varepsilon = \overline{\tau_{ji}\frac{\partial u_i''}{\partial x_j}} \quad (3.62)
$$

As it was previously conducted, the term that resulted from the coupling of the molecular diffusion and turbulent transport is approximated according to equation (3.59). Concerning

37

the terms $\overline{p'u_j''}$ and $\overline{p'\left(\partial u_i''/\partial x_i\right)}$, these are neglected as a consequence of the lack of knowledge on its behavior and the conviction of its negligible impact on the flow. In addition, the term $\overline{u_i''}\partial\overline{p}/\partial x_i$ is also neglected. Consequently, equation (3.61) is rewritten into

$$\frac{\partial}{\partial t}\left(\overline{\rho}k\right) + \frac{\partial}{\partial x_j}\left(\overline{\rho}\tilde{u}_j k\right) = t_{ij}\frac{\partial\tilde{u}_i}{\partial x_j} - \overline{\rho}\varepsilon + \frac{\partial}{\partial x_j}\left[\left(\mu + \frac{\mu_t}{\sigma_k}\right)\frac{\partial k}{\partial x_j}\right] \quad (3.63)$$

The turbulent kinetic energy is used to define the velocity scale however, there is still the need to define the length scale so that the system can be closed

$$\mu_t = \overline{\rho}k^{1/2}l \quad (3.64)$$

To define the turbulent length scale l, an additional transport equation for the turbulent dissipation rate is introduced, resulting in

$$\begin{aligned}\mu_t &\sim \overline{\rho}k^2/\varepsilon \\ l &\sim k^{3/2}/\varepsilon\end{aligned} \quad (3.65)$$

Regarding k, a definition was already presented in equation (3.63), however, it is still necessary to introduce a definition of ε.

Magalhães et al. [20] performed a RANS-based study, following the incompressible but variable density approach investigated by Barata et al. [18], on which the behavior of turbulence modeling under supercritical conditions is studied. For that purpose, through the computation of cases 3 and 4 of [61], the performance of several one and two-equation turbulence models are compared. The authors concluded that no direct correlation exists between turbulence model complexity and the quality of the numerically obtained results, in what supercritical fluid flows are regarded. The authors also concluded that computational time could be saved when resorting to simpler turbulence models.

Therefore, based on the results of [20], to achieve a computational time reduction, a compromise between turbulence model complexity and the consequent quality of the results and, having been previously validated for supercritical conditions by Magalhães et al. and Park [20, 22], we resort to the standard $k - \varepsilon$ turbulence model of [81] to close the governing equations system.

As a result, the standard $k - \varepsilon$ turbulence model [81] consists of

$$\frac{\partial}{\partial t}\left(\overline{\rho}k\right) + \frac{\partial}{\partial x_i}\left(\overline{\rho}\tilde{u}_i k\right) = t_{ij}\frac{\partial\tilde{u}_j}{\partial x_i} - \overline{\rho}\varepsilon + \frac{\partial}{\partial x_j}\left[\left(\mu + \frac{\mu_t}{\sigma_k}\right)\frac{\partial k}{\partial x_j}\right] \quad (3.66)$$

$$\frac{\partial}{\partial t}\left(\overline{\rho}\varepsilon\right) + \frac{\partial}{\partial x_i}\left(\overline{\rho}\tilde{u}_i\varepsilon\right) = C_{\varepsilon 1}\frac{\varepsilon}{k}t_{ij}\frac{\partial\tilde{u}_j}{\partial x_i} - C_{\varepsilon 2}\overline{\rho}\frac{\varepsilon^2}{k} + \frac{\partial}{\partial x_j}\left[\left(\mu + \frac{\mu_t}{\sigma_\varepsilon}\right)\frac{\partial\varepsilon}{\partial x_j}\right] \quad (3.67)$$

The turbulent viscosity is defined by

$$\mu_t = C_\mu \frac{\overline{\rho} k^2}{\varepsilon}$$
$$l = C_\mu \frac{k^{3/2}}{\varepsilon} \quad (3.68)$$

where C_μ represents a model constant. The remaining constants of the standard $k - \varepsilon$ turbulence model are presented in Table 3.1. Additionally, it is relevant to add that this model is only valid for fully turbulent flows since, in its derivation, the effects of viscosity on the turbulence structure are considered negligible.

Table 3.1: Standard $k - \varepsilon$ turbulence model constants [81].

Constant	Value
$C_{\varepsilon 1}$	1.44
$C_{\varepsilon 2}$	1.92
C_μ	0.09
σ_k	1.0
σ_ε	1.3

Before addressing a new topic, it is relevant to introduce additional considerations regarding heat transfer modeling. Given the preponderance of this phenomenon in a supercritical fluid injection context, several researchers have put considerable effort into its modeling. From a general point of view, heat transfer is modeled according to equation (3.60) where, depending on the adopted turbulence model, small changes concerning Pr_t are introduced (equations (3.67) to (3.68)). Regarding the Pr_t, owing to those studies, it appears that this variable has a significant impact on the development of the flow structure.

While Magalhães et al. [82] concluded that a constant value of 1 for Pr_t provides the best approximation, Mayer et al. [61] came to the same conclusion, justifying it due to the better consistency of their numerical results with the experimental data. Sierra-Pallares et al. [73] implemented a variable Pr_t model, using the experimental setup of [17], comparing it with constant Pr_t formulations. The authors concluded that the variable Pr_t model was unsuccessful, in contrast to a constant Pr_t formulation. Therefore, a constant value of 1 for Pr_t is adopted.

3.5 Near-wall modeling

The region close to the injector arouses great interest in studying, as it plays a preponderant role in the numerical solutions, considering the interactions and phenomena observed there.

In the region close to the wall, significant variations of the local Re are noted and, considering

that the adopted approximation depends on the value of the local Re, the y^+ parameter gains interest.

The y^+ is a function of the density, ρ, the friction velocity, u_τ, the absolute distance to the wall, y, and the dynamic viscosity, μ,

$$y^+ = \frac{\rho u_\tau y}{\mu} \quad (3.69)$$

Where the friction velocity is defined by

$$u_\tau = \sqrt{\frac{\tau_w}{\rho}} \quad (3.70)$$

with

$$\tau_w = \mu \left(\frac{\partial u}{\partial y} \right)_{y=0} \quad (3.71)$$

It is also relevant to introduce the concept of a dimensionless velocity, u^+, defined by

$$u^+ = \frac{u}{u_\tau} \quad (3.72)$$

The near-wall region of a flow consists of three main zones [83]. The closest zone to the wall is named the viscous sublayer, where in terms of y^+, it ranges between $0 < y^+ < 5$. In this zone, the flow is almost laminar, and the viscous effects dominate, consequently leading the dynamic viscosity to play a dominant role in mass, momentum, and heat transfer. Regarding the furthest zone, it is termed inertial sublayer or fully turbulent zone $(30 < y^+ < 400)$ as it is assumed that the flow is completely turbulent while considering that $\tau \approx \tau_w$. In between these two is the transition or 'buffer' zone $(5 < y^+ < 30)$ of vigorous turbulence dynamics where the flow is assumed not to be completely dominated by viscous effects nor completely turbulent. Figure 3.1 portrays a turbulent boundary layer typical dimensionless velocity profile, depicting the several zones.

Traditionally, there are two approaches regarding near-wall region modeling [79].
In one approach, the turbulence models can resolve the flow in all of the three zones of the near-wall region, therefore including the viscous sublayer. In this approach, $y^+ \approx 1$ is desirable, where a noticeable mesh resolution must exist due to the presence of large gradients of the solution variables and the vigorous occurrence of momentum and other scalar transports in the wall direction.

Regarding the alternative approach, the inner zone affected by viscosity (viscous sublayer and transition or buffer zone) is not resolved. Alternatively, this method resorts to semi-empirical equations named wall functions, whose objective is to 'act as a bridge' between the inner zone affected by viscosity and the fully turbulent zone. With the use of wall functions, the mesh resolution does not need to be that high, the y^+ should assume higher values, and there is
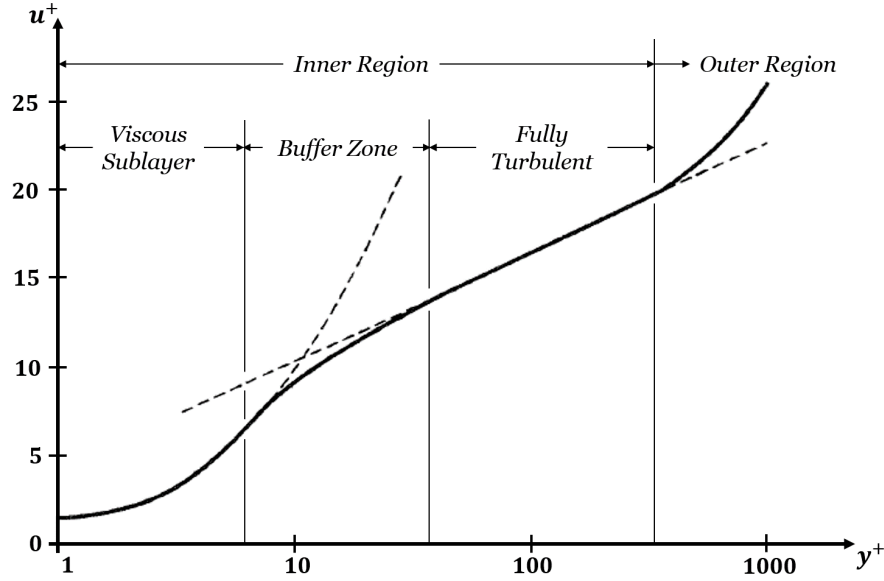
Figure 3.1: Turbulent boundary layer typical dimensionless velocity profile (adapted from [83]).

no need to modify turbulence models to account for the presence of the wall. However, the same mesh cannot be used for turbulence models of these two different approaches.

Regarding the adopted wall function approach used in this work, as is done in several engineering calculations, the 'buffer' zone is neglected and a point is defined where below that point the flow is considered to be purely viscous and above it is purely turbulent. Therefore, the momentum equation finally reduces for $y^+ \leq 11.63$ and $y^+ > 11.63$, where the value of 11.63 is the y^+ value at which equations (3.73) and (3.74) intersect. That can be seen in Figure 3.1, where equations (3.73) and (3.74) are represented resorting to dashed lines.

The equation which describes the velocity profile in the fully turbulent zone ($y^+ > 11.63$) is

$$u^+ = \frac{1}{\kappa} \ln(y^+) + \text{constant} \equiv \frac{1}{\kappa} \ln(Ey^+) \quad (3.73)$$

where κ is the von Kármán constant, and E is an integration constant that depends on the magnitude of the variation of shear stress across the layer and on the roughness of the wall [79].

While, in the viscous sublayer ($y^+ \leq 11.63$),

$$u^+ = y^+ \quad (3.74)$$

The equations that describe the velocity profile in the inner region are collectively termed the "law of the wall".

However, while achieving specific y^+ values has its importance, the overall mesh resolution inside the boundary layer is essential to obtain high-quality numerical results for the wall boundary layer. Therefore, an aimed y^+ value of 11.63 was considered for the first cells ad-

jacent to the walls and, whenever not possible, never lower. Furthermore, besides selecting the y^+ value, it is also imperative to define a minimum number of points in the mesh that are located inside the boundary layer. So, to guarantee sufficient mesh resolution in this region, it was defined that, in the wall-normal direction, there were at least 20 points inside the boundary layer.

Both the y^+ selection process and setting the minimum number of grid points inside the boundary layer are parameters that need to be preserved during the mesh refinement process and when testing different grid configurations. Nevertheless, other regions in the computational domain will be subjected to higher gradients of several thermophysical properties or will be more affected by the Boundary conditions. Therefore, as a consequence, during the mesh refinement process, the injector region and the jet centerline demand a higher concentration of cells than the rest of the computational domain.

3.6   Equation of State

As a consequence of operating in the supercritical regime where a slight temperature variation can lead to an abrupt variation of physical properties, attention must be taken to describe their evolution. Therefore, thermophysical properties like density, dynamic viscosity, thermal conductivity, and isobaric specific heat have to be modeled as close as possible to reality.

The EoS appears as the mathematical expression that relates pressure, molar or specific volume, and temperature for a pure homogeneous fluid in equilibrium states. The simplest EoS is the ideal gas EoS, being approximately valid for the low-pressure gas regions of the $p-T$ and p-v diagrams. Nevertheless, this formulation is no longer appropriate to describe fluid behavior, near and beyond the critical point, considering that diffusion coefficients become functions of pressure besides temperature [22].

Several equations are available in the literature to consider the departure from ideal gas to real gas behavior. After analyzing numerical studies that aim to describe supercritical fluid behavior, a significant preference for cubic EoS is noticeable. While several studies resorted to some PR EoS formulation [41, 42, 44, 45, 84], others introduced a correction to the PR EoS to considerably reduce the error in density prediction near the critical region [42, 44, 45, 68]. In contrast, [22, 27, 82, 85, 86] have used the SRK EoS. On the other side, while Branam and Mayer [43] have employed the MBWR model, [35, 72, 73] resort to a real gas library. In the present work, we resort to the cubic Peng-Robinson EoS since it is widely used in the literature and represents a compromise between accuracy and computational efficiency.

In a quest for improved reliability of the results, Peng and Robinson [48] proposed a two-parameter EoS, based on the van der Waals equation, with an enhanced prediction of the liquid density values. As the term refers, the cubic Peng-Robinson EoS resorts to three parameters for the characterization of a given thermophysical parameter: the critical point

temperature and pressure, and the acentric factor ω (a measure of the nonsphericity of the molecules).

While the ideal gas equation does not consider, two-parameter EoS take into account both the intermolecular attraction forces and the finite volume of the molecules through the parameters a and b, respectively

$$p = \frac{RT}{v-b} - \frac{a(T)}{v\left(v+b\right)+b\left(v-b\right)} \quad (3.75)$$

where v is the molar volume and R the molar gas constant.

The variables a and b are defined by

$$a\left(T\right) = a\left(T_c\right)\beta\left(\tau,\omega\right)$$
$$a\left(T_c\right) = 0.45724\frac{R^2T_c^2}{p_c} \quad (3.76)$$
$$b = 0.07780\frac{RT_c}{p_c}$$

where τ is the inverse reduced temperature, i.e., equal to T_c/T.

The dimensionless function $\beta\left(\tau,\omega\right)$ is defined by

$$\beta\left(\tau,\omega\right)^{0.5} = 1 + m\left(1 - \tau^{-0.5}\right)$$
$$m = 0.37464 + 1.54226\omega - 0.26992\omega^2 \quad (3.77)$$

To employ this EoS, the required variables are only the critical parameters (T_c and p_c) and the acentric factor ω, thus revealing the simplicity of this formulation, especially when compared to more complex multi-parameter EoS. For the nitrogen case, the critical properties are listed in Table 2.1 and the acentric factor ω is equal to 0.0372. Thus, it is possible to verify why one of the major arguments for using the Peng-Robinson EoS is simplicity.

However, equation (3.75) can be rewritten into

$$Z^3 - (1-B)Z^2 + (A - 3B^2 - 2B)Z - (AB - B^2 - B^3) = 0 \quad (3.78)$$

where

$$A = \frac{ap}{R^2T^2}$$
$$B = \frac{bp}{RT} \quad (3.79)$$
$$Z = \frac{pv}{RT}$$

In the last set of equations, Z represents the compressibility factor, and it is the variable to

be solved in the polynomial of equation (3.78). The referred equation has three roots, where only the smallest positive root is of interest.

3.7 Transport properties

Transport properties have a preponderant impact on the governing equations through such terms as those in equations (3.21) and (3.48) that must, therefore, be properly defined.

The substantial variation of transport properties is already discussed in Section 2.1 and in Figures 2.1 and 2.2, where a strong decrease in dynamic viscosity and thermal conductivity is evident approaching and entering supercritical conditions. To surpass this nonlinear behavior, it resorts to the work of Lemmon and Jacobsen [87] to define both μ and κ. Since we use a cubic EoS, User Defined Functions (UDFs) are written to define these properties.

The work conducted by Lemmon and Jacobsen [87] proposes a method for the calculation of transport properties, such as dynamic viscosity and thermal conductivity. The adopted transport property equations for μ and κ resort to the independent properties of temperature and density as input conditions. In addition, accurate EoS for pure fluids must be used to obtain the necessary density. The associated error with these formulations is within 2% for both the dynamic viscosity and thermal conductivity.

The dynamic viscosity, μ, is expressed as the sum of two terms, where the first term is the dilute gas viscosity, and the second is the residual fluid viscosity. In equation (3.80), the dynamic viscosity in $\mu\mathrm{Pa} \cdot \mathrm{s}$ is set as a function of T, τ and $\delta = \rho/\rho_c$,

$$\mu = \mu^0 (T) + \mu^r (\tau, \delta) \quad (3.80)$$

The dilute gas contribution, $\mu^0 (T)$, is given by

$$\mu^0 (T) = \frac{0.0266958\sqrt{MT}}{\sigma^2 \, \Phi (T^*)} \quad (3.81)$$

where M is the molar mass, σ the Lennard-Jones size parameter, and Φ the collision integral. In addition, $\Phi (T^*)$ is given by

$$\Phi (T^*) = \exp \left(\sum_{i=0}^{4} b_i \left[\ln (T^*) \right]^i \right) \quad (3.82)$$
$$T^* = T/\theta$$

where θ represents the Lennard-Jones energy parameter. The Lennard-Jones parameters are presented in Table 3.5, and the coefficients b_i in Table 3.2.

The residual fluid contribution, $\mu^r(\tau, \delta)$, is calculated through

$$\mu^r(\tau, \delta) = \sum_{i=1}^{n} N_i \tau^{t_i} \delta^{d_i} \, \exp(-\gamma_i \delta^{l_i}) \quad (3.83)$$

where $\gamma_i = 0$ when $l_i = 0$ and $\gamma_i = 1$ when $l_i \neq 0$. The coefficients and exponents used in equation (3.83) are given in Table 3.3.

The evolution of dynamic viscosity for different pressure levels is depicted in Figure 2.1. It is possible to notice that the $4\,\mathrm{MPa}$ pressure level (the critical point of nitrogen) still has some influence, despite becoming less pronounced as pressure increases.

Table 3.2: Coefficients of the collision integral equation for nitrogen [87].

i	b_i
0	0.431
1	−0.4623
2	0.08406
3	0.005341
4	−0.00331

Table 3.3: Coefficients and exponents of the residual fluid viscosity utilized in equation (3.83) for nitrogen [87].

i	N_i	t_i	d_i	l_i
1	10.72	0.1	2	0
2	0.03989	0.25	10	1
3	0.001208	3.2	12	1
4	−7.402	0.9	2	2
5	4.620	0.3	1	3

Similar to the dynamic viscosity formulation, the authors also presented a model to calculate the thermal conductivity, κ, expressed in $\mathrm{mW \cdot m^{-1} \cdot K^{-1}}$, being defined as

$$\kappa = \kappa^0(T) + \kappa^r(\tau, \delta) + \kappa^c(\tau, \delta) \quad (3.84)$$

The present model calculates thermal conductivity as the sum of three distinct terms.

The first term, $\kappa^0(T)$, refers to the dilute gas thermal conductivity

$$\kappa^0(T) = N_1 \left[\frac{\mu^0(T)}{1 \times 10^{-6}} \right] + N_2 \tau^{t_2} + N_3 \tau^{t_3} \quad (3.85)$$

The second term, $\kappa^r(\tau, \delta)$, refers to the residual fluid thermal conductivity

$$\kappa^r(\tau, \delta) = \sum_{i=4}^{n} N_i \tau^{t_i} \delta^{d_i} \exp(-\gamma_i \delta^{l_i}) \quad (3.86)$$

The coefficients and exponents used in equations (3.85) and (3.86) are given in Table 3.4. Regarding γ_i, it maintains the same definition as that presented for equation (3.83).

Lastly, the third term, $\kappa^c(\tau, \delta)$, resorts to the thermal conductivity critical enhancement model proposed by Olchowy and Sengers [88] used to evaluate the singular behavior of thermal conductivity in the critical point vicinity

$$\kappa^c(\tau, \delta) = \rho c_p \frac{k_B R_0 T}{6\pi \xi \mu} \left(\hat{\Phi} - \hat{\Phi}_0 \right) \quad (3.87)$$

In equation 3.87, μ is the dynamic viscosity already presented in equation (3.80), whereas $\hat{\Phi}$, $\hat{\Phi}_0$, and ξ are defined by

$$\hat{\Phi} = \frac{2}{\pi} \left[\left(\frac{c_p - c_v}{c_p} \right) \tan^{-1} \left(\frac{\xi}{q_D} \right) + \frac{c_v}{c_p} \left(\frac{\xi}{q_D} \right) \right] \quad (3.88)$$

$$\hat{\Phi}_0 = \frac{2}{\pi} \left\{ 1 - \exp \left[\frac{-1}{(\xi/q_D)^{-1} + \frac{1}{3}(\xi/q_D)^2 (\rho_c/\rho)^2} \right] \right\} \quad (3.89)$$

$$\xi = \xi_0 \left[\frac{\widetilde{\chi}(T, \rho) - \widetilde{\chi}(T_{\text{ref}}, \rho)(T_{\text{ref}}/T)}{\Gamma} \right]^{v/\gamma} \quad (3.90)$$

where $\widetilde{\chi}(T, \rho)$ is given by

$$\widetilde{\chi}(T, \rho) = \frac{p_c \rho}{\rho_c^2} \left(\frac{\partial \rho}{\partial p} \right)_T \quad (3.91)$$

The isobaric and isochoric specific heats, c_p and c_v, along with $\widetilde{\chi}$ are calculated from the EoS at the specified temperature and density. The remaining parameters both used in the viscosity and thermal equations are presented in Tables 2.1 and 3.5. In addition, κ^c is set to zero when ξ is negative or zero.

Figure 2.2 portrays the thermal conductivity evolution for different pressure levels. It is possible to observe that, in Figure 2.2, the effect of the critical point is considerably more pronounced than for the dynamic viscosity case in Figure 2.1, as suggested by the $4\,\mathrm{MPa}$ pressure plot. Hence, the mathematical model could benefit from the addition of a critical enhancement term in the thermal conductivity modeling to deal with the critical point singularity.

Table 3.4: Coefficients and exponents of the thermal conductivity equation for nitrogen [87].

i	N_i	t_i	d_i	l_i
1	1.511	–	–	–
2	2.117	−1.0	–	–
3	−3.332	−0.7	–	–
4	8.862	0.0	1	0
5	31.11	0.03	2	0
6	−73.13	0.2	3	1
7	20.03	0.8	4	2
8	−0.7096	0.6	8	2
9	0.2672	1.9	10	2

Table 3.5: Parameters used in the viscosity and thermal conductivity equations for nitrogen [87].

Parameter	Value
$\rho_c \ [\mathrm{mol} \cdot \mathrm{dm}^{-3}]$	11.1839
$M \ [\mathrm{g} \cdot \mathrm{mol}^{-1}]$	28.01348
$\theta \ [\mathrm{K}]$	98.94
$\sigma \ [\mathrm{nm}]$	0.3656
$\xi_0 \ [\mathrm{nm}]$	0.17
$q_D \ [\mathrm{nm}]$	0.40
$T_{\mathrm{ref}} \ [\mathrm{K}]$	252.384
$k_B \ [\mathrm{J} \cdot \mathrm{K}^{-1}]$	1.380658×10^{-23}
$R \ [\mathrm{J} \cdot \mathrm{mol}^{-1} \cdot \mathrm{K}^{-1}]$	8.3145
R_0	1.01
Γ	0.055
γ	1.2415
v	0.63

For the Peng-Robinson EoS, the isobaric specific heat, c_p, is calculated resorting to the departure function formulation, i.e., is calculated as the sum of the ideal contribution with a departure isobaric specific heat function. In the same way, as it was performed for the dynamic viscosity and thermal conductivity, this formulation is implemented through a UDF.

The ideal contribution, $c_{p,\mathrm{ideal}}$, adopted in this work is based on the formulation of Span et al. [53] for nitrogen. According to the authors, this definition presents an average error of less than 0.02% from the triple point to temperatures of 523 K and pressures up to 12 MPa. $c_{p,\mathrm{ideal}}$ is defined in equation (3.92), where $u = 3364.011/T$ K.

$$\frac{c_{p,\mathrm{ideal}}}{R} = 3.5 + 3.066469 \times 10^{-6}T + 4.701240 \times 10^{-9}T^2 - 3.987984 \times 10^{-13}T^3 +$$
$$+ 1.012941\frac{u^2 \exp(u)}{[\exp(u) - 1]^2} \quad (3.92)$$

Additionally, the departure isobaric specific heat function, $c_{p,\text{departure}}$, is calculated as presented in equation (3.93).

$$c_{p,\text{departure}} = c_{v,\text{departure}} - R - T\frac{(\partial V/\partial T)^2}{(\partial V/\partial p)} \quad (3.93)$$

In equation (3.93), the departure isochoric specific heat function, $c_{v,\text{departure}}$, is calculated by differentiating the equation for the departure of the internal energy with respect to the temperature. Regarding the partial derivatives, they are calculated by differentiating the EoS (equation (3.75)).

Ultimately, when resorting to a cubic EoS, the isobaric specific heat is given by

$$c_p = c_{p,\text{ideal}} - \frac{c_{p,\text{departure}}}{M} \quad (3.94)$$

The use of real gas formulations for the transport and thermodynamic properties enables the mathematical model to capture the weak compressibility effects when resorting to an incompressible but variable density approach. As the departure function formulation is used to account for real gas effects in the evaluation of transport properties, thermodynamic properties, e.g., enthalpy, are also evaluated by the same principle.

Chapter 4

Numerical Algorithm

The governing equations presented in the last chapter can be affected by a considerable amount of error as a consequence of the adopted approximations. Albeit these can be responsible for a significant amount of error, they are not the only source of error. Having defined the system of governing equations, they must be applied to a finite computational domain. However, this process has an associated numerical error. As a result, this chapter reviews the work performed in the numerical algorithm field. Section 4.1 introduces the Finite Volume Method (FVM) used to discretize the governing equations system, where we aim to maintain the numerical error as low as possible. Then, Section 4.2 presents a brief explanation of the algorithm that defines the order in which every equation is calculated as well as the methods used to prevent the appearance of the odd-even decoupling of pressure and velocity. Finally, Section 4.3 reviews the initialization method employed and the defined convergence criteria, while Section 4.4 discusses the under-relaxation used to control the stability and convergence rate of the numerical computations.

4.1   Discretization

In this work, the Finite Volume Method (FVM) is utilized, where the integral formulation of the conservation laws is discretized directly in the considered physical domain. This technique is considerably used in CFD, where one of its most notable advantages is associated with the concept of conservative discretization.

Under the concept of the conservative formulation of the flow equations, it is now of the utmost importance to preserve the global conservation of the basic flow quantities (mass, momentum, and energy) at the discrete level. Nevertheless, such has an impact on the way the discretization process is performed. In this sense, it has resorted to the noticeable advantage of the FVM, where the conservative discretization is automatically satisfied through the direct discretization of the integral formulation of the conservation laws [70].

Considering an arbitrary subdivision of the control volume Ω into n subvolumes, in such a way that Ω is equal to $\Omega_1 + \Omega_2 + ... + \Omega_n$, the conservation equation is applied to each of the n finite subvolumes leading to the mutual cancellation of the internal surface fluxes, leaving only the external contributions. By doing so, the scheme will remain conservative [70].

To introduce the discretization subject, let us consider the theoretical definition of the deriva-

tive of a given function $\phi(x)$ at point x

$$\frac{\partial \phi}{\partial x} = \lim_{\Delta x \to 0} \frac{\phi(x + \Delta x) - \phi(x)}{\Delta x} \quad (4.1)$$

By removing the limit in equation (4.1), the result is a finite difference, thus portraying the finite difference approximation used to obtain numerical solutions of differential equations.

With the application of a Taylor series development of $\phi(x + \Delta x)$ around $\phi(x)$, with $\Delta x \neq 0$, we have

$$\phi(x + \Delta x) = \phi(x) + \Delta x \frac{\partial \phi}{\partial x} + \frac{\Delta x^2}{2!} \frac{\partial^2 \phi}{\partial x^2} + \frac{\Delta x^3}{3!} \frac{\partial^3 \phi}{\partial x^3} + \ldots \quad (4.2)$$

or, alternatively,

$$\frac{\phi(x + \Delta x) - \phi(x)}{\Delta x} = \frac{\partial \phi}{\partial x} + \frac{\Delta x}{2!} \frac{\partial^2 \phi}{\partial x^2} + \frac{\Delta x^2}{3!} \frac{\partial^3 \phi}{\partial x^3} + \ldots = \frac{\partial \phi}{\partial x} + O(\Delta x) \quad (4.3)$$

In addition, if the truncation error $O(x)$ is restricted to its dominant term, i.e., to the lower power in Δx, it is said that the truncation error goes to zero like the first power in Δx and the approximation is first order in Δx.

Equation (4.3) can still be rewritten for the case of a discrete domain with a finite number of points, as represented in Figure 4.1, where we obtain

$$\frac{\partial \phi_C}{\partial x} = \frac{\phi_E - \phi_C}{\Delta x_e} - \frac{\Delta x}{2!} \frac{\partial^2 \phi_C}{\partial x^2} - \frac{\Delta x^2}{3!} \frac{\partial^3 \phi_C}{\partial x^3} = \frac{\phi_E - \phi_C}{\Delta x_e} + O(\Delta x) \quad (4.4)$$

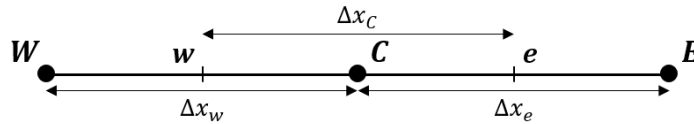This equation is considered a first-order forward difference.

Figure 4.1: Representation of a discrete domain with cell center values associated and its face values.

Furthermore, by replacing Δx with $(-\Delta x)$ in the previous equation, the resulting relation is termed a first-order backward difference

$$\frac{\partial \phi_C}{\partial x} = \frac{\phi_C - \phi_W}{\Delta x_w} + \frac{\Delta x}{2!} \frac{\partial^2 \phi_C}{\partial x^2} - \frac{\Delta x^2}{3!} \frac{\partial^3 \phi_C}{\partial x^3} = \frac{\phi_C - \phi_W}{\Delta x_w} + O(\Delta x) \quad (4.5)$$

Additionally, still with some interest, equations (4.4) and (4.5) can be added, thus leading to a relation known as a second-order central difference

$$\frac{\partial \phi_C}{\partial x} = \frac{\phi_E - \phi_W}{\Delta x_w + \Delta x_e} - \frac{\Delta x^2}{3!} \frac{\partial^3 \phi_C}{\partial x^3} = \frac{\phi_E - \phi_W}{\Delta x_w + \Delta x_e} + O(\Delta x^2) \quad (4.6)$$

or

$$\frac{\partial \phi_C}{\partial x} = \frac{\phi_e - \phi_w}{\Delta x_C} + O(\Delta x^2) \quad (4.7)$$

While the principal numerical quantities, when resorting to the Finite Difference Method, are the local function values at the mesh points, the FVM relies on a cell-averaged values approach. In the FVM, a local finite volume (control volume) is associated with each mesh point of a given grid. Then, the integral conservation laws are applied to each of these local volumes. While in a finite difference approach, the discretized space is considered a set of points, in the FVM, the discretized space is formed by a finite volume cells set, where each cell is associated with each mesh point. This difference between the FVM and the Finite Difference Method is of the utmost importance. However, it is also necessary to know the face values ϕ_w and ϕ_e, which are obtained, through interpolations, from the cell-centered values. There are several possibilities regarding the type of interpolation scheme to use where crucial factors like the number of points used and their relative position preponderantly affect the order of accuracy of the discretization scheme and how it handles different physical phenomena [70].

Regarding the diffusion phenomenon, the diffusion of a given quantity is proportional to the gradient of the corresponding quantity, where this phenomenon presents an isotropic behavior in all directions of the considered domain. With that in mind and one of the most fundamental guidelines of numerical discretization, which states that the properties of a numerical discretization scheme may never contradict the physical phenomena it intends to describe, a central difference formula seems most appropriate to describe this phenomenon. Therefore, the diffusive terms in the governing equations are discretized following a second-order central scheme.

Concerning the discretization of the advective terms, the QUICK scheme [89] is employed. This scheme is used to reduce the oscillatory and unstable behavior of the second-order schemes and to handle the numerical diffusion that affects the first-order upwind schemes.

Due to the lack of extensive knowledge regarding mixing under supercritical conditions, efforts have been made in the modeling area to complement the experimental research. However, one of the main difficulties that have been noted is the ability of numerical solvers to maintain accuracy and stability in regions where large gradients of density and thermodynamic quantities exist [90].

As a consequence of the strong thermodynamic nonlinearities in the vicinity of the Widom line, small variations of density and/or energy may create pressure oscillations. In addition, due to nonlinearities in the EoS and strong field gradients, the reconstructed pressure may differ from the real physical pressure and, consequently, result in artificial pressure variations [90]. As a result, these non-physical pressure oscillations can pollute the accuracy of

the solutions or even lead to the divergence of the calculation.

It is intended that, with the use of the QUICK scheme, the appearance of these non-physical pressure oscillations is attenuated by the introduction of first-order upwinding. Such tends to occur when a second-order central scheme is applied to the advective terms when the grid Péclet number (Pe) is higher than two, i.e., advection is two times greater than diffusion.

The QUICK scheme introduced by Leonard [89] has the peculiarity of combining the high-order accuracy with the directional behavior of upwind schemes, thus providing additional stability for the advective terms in coarser meshes.
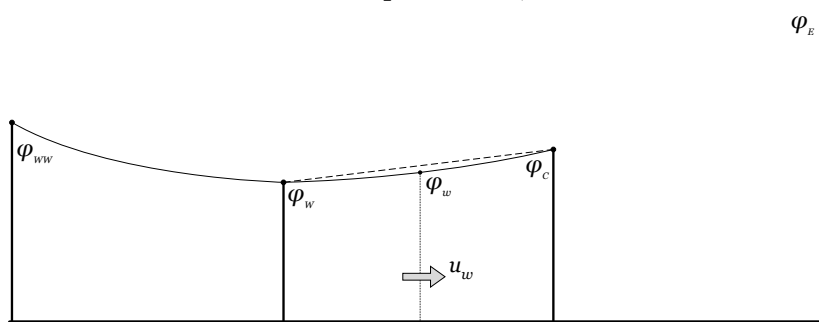
According to the illustrations in Figures 4.2a and 4.2b, the face values ϕ_e and ϕ_w are defined by

$$\phi_e = \frac{1}{2}(\phi_C + \phi_E) - \frac{1}{8}(\phi_W + \phi_E - 2\phi_C) \quad (4.8)$$

$$\phi_w = \frac{1}{2}(\phi_W + \phi_C) - \frac{1}{8}(\phi_{WW} + \phi_C - 2\phi_W) \quad (4.9)$$
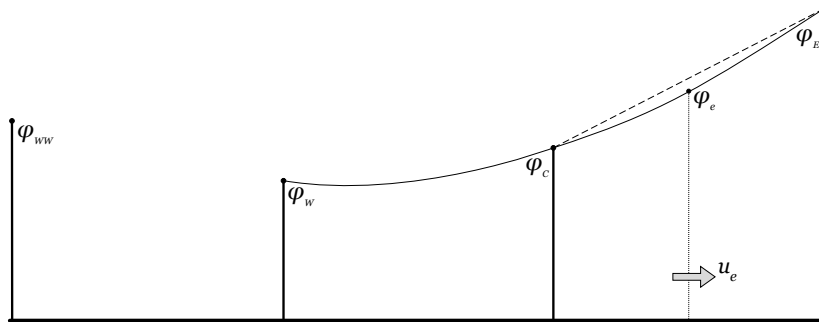
(a) Interpolation of ϕ_e.

(b) Interpolation of ϕ_w.

Figure 4.2: Quadratic interpolation (adapted from [89]).

In addition, as can be observed, the slope of the parabola at ϕ_e is identical to the slope of the chord linking ϕ_C with ϕ_E, thus meaning that the gradient can be defined as presented in equation (4.7). In analogy to the upwind scheme, the direction of the interpolation is based

on the velocity values. As a result, with this technique, the QUICK scheme achieves third-order accuracy for the advective terms in a FVM approach [91].

4.2 Solution approach

A pressure-based algorithm is implemented in which the conservation of mass is achieved not resorting to the continuity equation (3.44) but implicitly achieved through a pressure-based continuity equation instead. This equation is obtained by taking the divergent of the momentum equation (3.45) and introducing the condition $\frac{\partial \overline{\rho} \tilde{u}_i}{\partial x_i} = 0$.

Müller et al. [42] performed LES simulations, where a comparison is made between a density-based and a pressure-based solution. The results comparison from the two solution approaches does not show any significant difference in the mean centerline density profiles.

The rationale for this method is presented by Jarczyk and Pfitzner [68], where a pressure-based approach is chosen to avoid extra efforts in correcting the ill-conditioned solution matrix while implementing a density-based solution approach.

In a first instance, fluid properties are calculated through the equations presented in Sections 3.6 and 3.7 with either the initial conditions or the current solution values. In this group of properties to be calculated, turbulent viscosity is also included. Subsequently, a system of equations that includes the momentum and pressure-based continuity equations is solved to obtain the velocity and pressure fields simultaneously. At a later stage, the energy equation (3.60) and the transport equations for turbulent variables, introduced in Section 3.4, are solved until convergence is reached. A flowchart of the numerical procedure is presented in Figure 4.3.

However, the pressure values at the cell faces in equation (3.45) are still required, hence these must be interpolated from the cell-centered values. In a collocated grid scheme, both the velocity and the pressure values needed for the interpolation are selected from the same cell. Nevertheless, when calculating the pressure field on a collocated grid, oscillations in the pressure field may arise as a consequence of an odd-even decoupling of pressure and velocity, i.e., that pressure and velocity do not affect one another on a specific point [70].

As a result, a staggered grid configuration [92] is used in this work, thus benefiting from the consequence of eliminating the decoupling of the pressure and velocity fields as well as with any possible oscillations. A peculiarity of this configuration is that the velocity and pressure values are stored in different positions and for which the control volumes are no longer equal. In addition, the pressure values are calculated directly for the cell face, thus eliminating the need for interpolations.
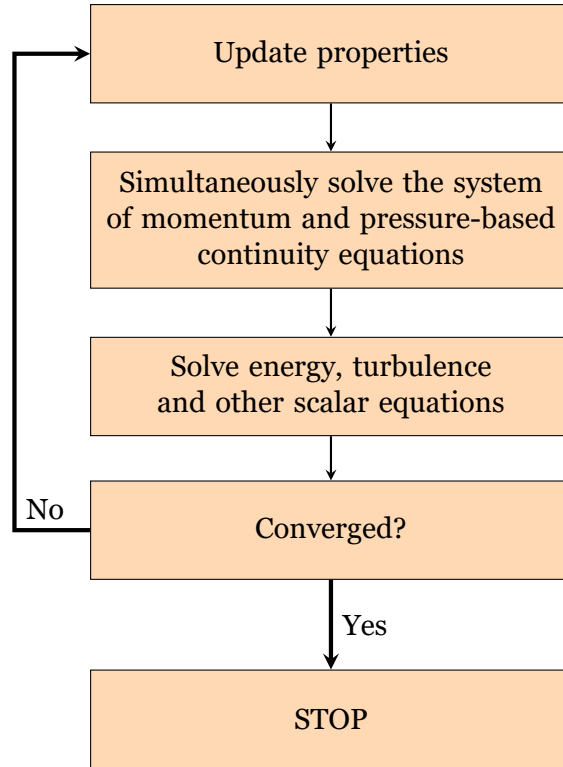
Figure 4.3: Pressure-based solution algorithm [68].

4.3 Initialization method and convergence criteria

Regarding the initialization method, a hybrid method is employed where boundary conditions are introduced, such as the inlet velocity set to u_0 from Table 5.1 and the absolute pressure at the outlet set to p_∞. The velocity and pressure fields calculated with the previous methods are then introduced in the first cycle of the pressure-based algorithm represented in Figure 4.3.

In the present work, convergence is achieved when all the conditions for the various equations in Table 4.1 are reached. The residuals perform a significant role, as they are used as convergence criteria due to their link to the solution error. Such is related to the fact that when this error tends to zero, so the residuals do [70]. This procedure is necessary considering that the exact solution is not known, making it impossible for the solution error to be directly calculated.

Table 4.1: Convergence criteria.

Equation	Absolute criteria
Continuity	1×10^{-4}
Momentum	1×10^{-5}
Energy	1×10^{-5}
Turbulent Kinetic Energy	1×10^{-5}
Turbulent Dissipation Rate	1×10^{-5}

4.4   Under-relaxation

In this work, we have also resorted to the application of explicit under-relaxation, whose purpose is to control the change in the value of a variable U, from a given iteration to the following. Consequently, under-relaxation plays a preponderant role in the convergence rate, as well as in the possible instabilities and oscillations that may arise (from its application).

Under-relaxation is then implemented through the introduction of an under-relaxation factor, θ, in such a way that

$$U = U^{\text{old}} + \theta(U^{\text{calculated}} - U^{\text{old}}) \quad (4.10)$$

where $U^{\text{calculated}}$ is the calculated solution and U^{old} is the solution obtained at the previous iteration. The under-relaxation factors used are presented in Table 4.2.

However, the solutions must be independent of the under-relaxation. In this way, under-relaxation is applied in two distinct phases. In the first phase, a high level of under-relaxation is applied to the variables that have reached convergence (Initial Relaxation Factors). Then, a lower level of under-relaxation (Verification Relaxation Factor) is applied, letting the iterative solver restart from the last solution for about 100-200 iterations. If this lower level of under-relaxation has no significant influence on the residuals, the solution is considered independent. Considering that there is no noticeable disturbance in the residuals, it can be concluded that the solution is independent. The influence of under-relaxation is only verified on the speed and stability of convergence.

Table 4.2: Under-relaxation factors.

Variable	Initial Relaxation Factor	Verification Relaxation Factor
p	0.4	0.7
ρ	0.4	0.5
μ_t	0.4	0.7
k	0.4	0.7
ε	0.4	0.7
Momentum	0.4	0.7
Energy	0.4	0.5
Body Forces	0.5	0.7

Chapter 5

Implementation

This chapter presents the experimental conditions of Oschwald and Schik [17] that are studied in this work. Therefore, this chapter is dedicated to the definition of the experimental conditions to be numerically computed, where their distribution in relation to the Widom line is clarified. Furthermore, the definition of the corresponding finite computational domain is presented in addition to the initial and boundary conditions.

5.1 Initial and boundary conditions

The experimental conditions of Oschwald and Schik [17] are the basis of comparison for the present numerical study. In the experimental work, cryogenic nitrogen is injected at trans-critical and supercritical conditions into a chamber filled with gaseous nitrogen at ambient temperature. The injection and chamber conditions are presented in Table 5.1, where the subscript inj concerns the injection conditions while subscript ∞ regards the chamber conditions.

Table 5.1: Experimental test matrix [17].

Case	p_∞ [MPa]	u_{inj} [m $\cdot$ s^{-1}]	T_{inj} [K]	T_∞ [K]	ρ_{inj} [kg $\cdot$ m^{-3}]	ρ_∞ [kg $\cdot$ m^{-3}]
A4	4	5	140	298	150.70	45.42
B4	4	5	118	298	584.43	45.42
C4	4	20	100	298	707.65	45.42
A6	6	5	140	298	340.77	68.08
B6	6	5	118	298	610.03	68.08
C6	6	20	100	298	717.19	68.08

The experimental data of [17] was obtained resorting to the Raman scattering technique and four windows in the test facility, thus allowing optical diagnostics.

In the present numerical study, six experimental cases are considered, divided between supercritical and transcritical conditions for two different pressure levels in the chamber, p_∞, 4 and 6 MPa. There are also two levels for the injection velocity, u_{inj}, of 5 and 20 m $\cdot$ s^{-1}. Regarding the injection temperatures, T_{inj}, there are three distinct temperature levels of 140 K, considerably above the critical temperature of nitrogen, and the levels of 118 K and 100 K, characterizing the transcritical jet behavior. Figure 5.1 depicts the experimental data distribution in relation to the Widom line.
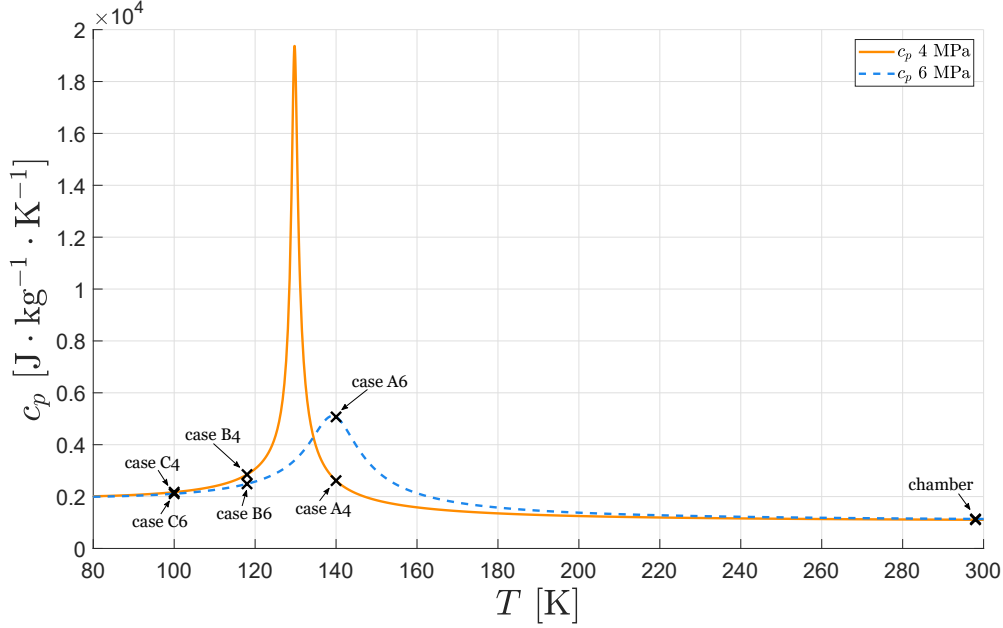
Figure 5.1: Experimental data distribution in relation to the Widom line (data from the NIST database) [26].

The experimental test case conditions can also be presented in dimensionless variables being introduced in Table 5.2. The presented values include the reduced values of pressure, with respect to the pressure in the chamber and temperature, in relation to its value at the injection. In addition, the ratio between density at injection and in the chamber is also presented.

With this representation, it is possible to identify every single test case position in relation to the conditions at the critical point of nitrogen and substantiate that the injection conditions have a dominant role and will determine jet behavior.

Table 5.2: Experimental test case conditions expressed as dimensionless variables.

Case	p_∞/p_c	T_{inj}/T_c	ρ_{inj}/ρ_∞
A4	1.17	1.11	3.34
B4	1.17	0.94	12.5
C4	1.17	0.79	15.7
A6	1.76	1.11	5.01
B6	1.76	0.94	8.99
C6	1.76	0.79	10.6

Based on the experimental setup of [17] depicted in Figure 5.2, the corresponding computational domain is portrayed in Figure 5.3, detailing the boundary conditions.

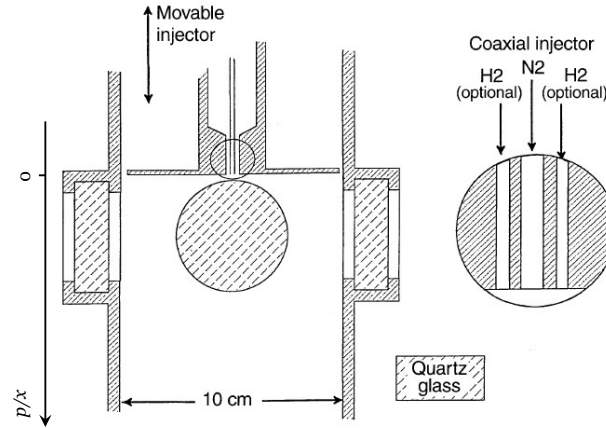**Numerical study on nitrogen injection at trans- and supercritical conditions**

Figure 5.2: Test chamber [17].

A two-dimensional axisymmetric configuration is selected over a three-dimensional to reduce computational costs. The experiments presented by the authors were performed with a nitrogen-free jet without any coaxial injection and, for this reason, the adopted geometry only contains the central injector. The depicted chamber and injector have a diameter of 100 mm and 1.9 mm and a length of 250 mm and 88 mm, respectively. Assuming that the chamber is vertically aligned, the parameter f_x in equation (3.45) is set to $9.81 \text{ m} \cdot \text{s}^{-2}$.
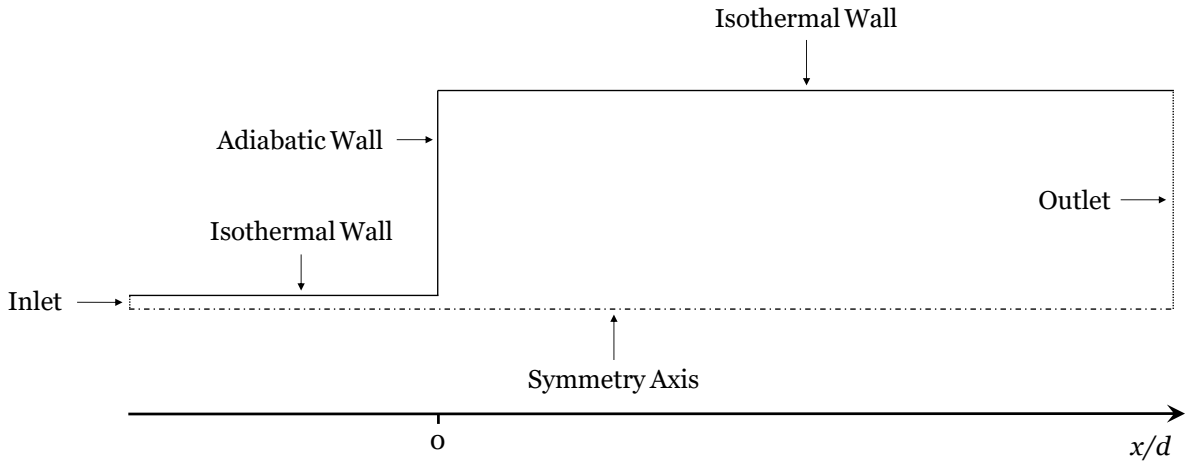

Figure 5.3: Boundary conditions.

The computational domain contains five different boundary conditions. A constant axial velocity profile equal to u_{inj} is imposed at the inlet, following the values presented in Table 5.1. In addition, the radial velocity component is set to zero. At the chamber and injector walls, a no-slip condition is applied, where both the normal and tangential components of velocity are set to zero.

A pressure outlet is defined with a gauge pressure of 0 MPa. In addition, the pressure values at the outlet face are calculated by averaging the specified operating pressure of p_∞ with the internal pressure. Regarding the symmetry axis, the value of any specific property is equaled

to that of the adjacent cell, and the normal derivatives are zero.

Concerning the boundary conditions, in the adiabatic chamber face-plate, the heat flux, defined in equations (3.56) and (3.57), is set to zero. However, in the case of the isothermal walls, i.e., the injector and chamber walls, the heat transfer is calculated through a Dirichlet boundary condition, presented in equation (5.1), by imposing a constant wall temperature of 298 K,

$$q = h_f(T_w - T_\infty) \quad (5.1)$$

where h_f represents the fluid heat transfer coefficient, T_w is the temperature at the wall, and T_∞ is the local fluid temperature.

The initial conditions for the turbulence quantities, the turbulent kinetic energy and turbulent dissipation rate, are presented according to equations (5.2) and (5.3), respectively

$$k_0 = \frac{3}{2}(Iu)^2 \quad (5.2)$$

$$\varepsilon_0 = \frac{C_\mu^{3/4} k^{3/2}}{0.014l} \quad (5.3)$$

In the previous equations, I is the turbulence intensity, set to 5%, per a preliminary study. In addition, l is the characteristic length scale, considered to be equal to the injector diameter, and the velocity scale, u, is equal to the injection velocity.

Chapter 6

Results

This chapter presents the numerically obtained results for the experimental conditions of Oschwald and Schik [17]. The chapter is divided into two sections: Section 6.1 reviews the results concerning the supercritical injection cases (cases A4 and A6) and Section 6.2, where the results regarding the transcritical injection cases (cases B4, B6, and C4, C6) are presented. Considering certain experimental case conditions operate in different regimes, several grid independence studies are performed to assure that the numerically obtained results are highly accurate and independent of the grid resolution. The numerically obtained axial density distributions are presented as dimensionless variables, through a variable ρ^*, widely used in the literature since it provides researchers with a common scale for comparison. The injection and chamber conditions values are specific for each experimental case condition and are presented in Tables 5.1 and 5.2. In addition, density field comparisons are performed using the respective absolute density values.

6.1   Supercritical conditions

Figure 6.1 portrays the comparison between the results obtained for the axial density distribution at the jet centerline for case A4 and the experimental data of Oschwald and Schik [17]. As a result, a new variable, ρ^*, widely used in the literature, thus allowing the comparison between different existing studies, is introduced to describe the dimensionless density distribution. This variable is then defined by

$$\rho^* = \frac{\rho - \rho_\infty}{\rho_{inj} - \rho_\infty} \quad (6.1)$$

The values used to perform the nondimensionalization in each case, respectively, are presented in Table 5.1. Still, in the referred figure, x/d represents the axial distance from the injector normalized by the injector's diameter, d.

Among the results obtained, three different mesh refinement levels were evaluated to guarantee that grid resolution did not influence the results. In this sense, three structured orthogonal meshes of rectangular elements were studied: a coarse mesh with about 185 000 points, a fine one with 281 000, and a more refined mesh with 497 000 points. Considering that no significant variation between the slopes of the three configurations is depicted, grid independence is achieved for the fine mesh. Resorting to the finest configuration does not seem to justify considering that the gain in accuracy does not outweigh the additional computational cost.
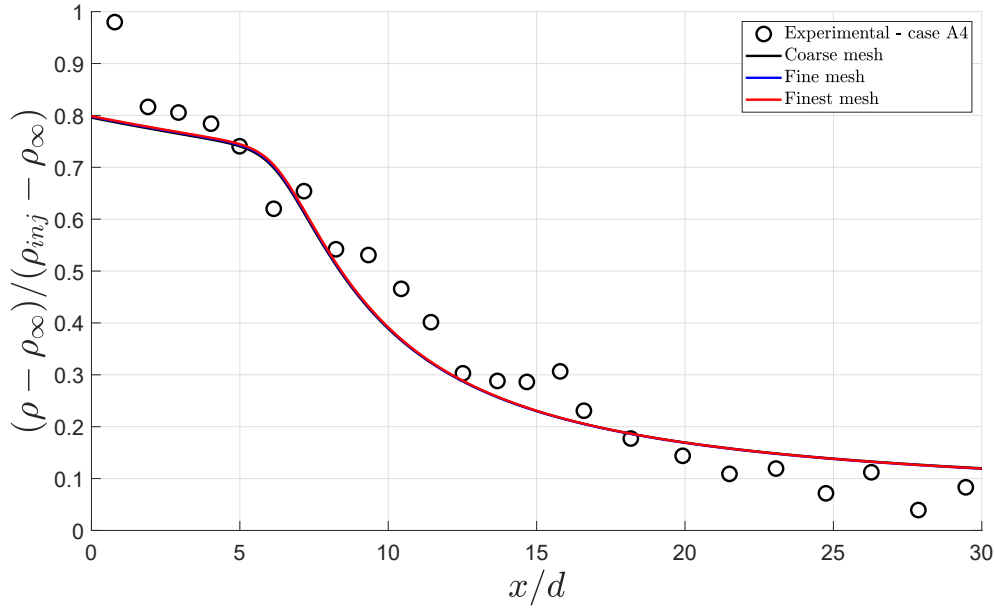
Figure 6.1: Axial density distribution for case A4.

The case represented in Figure 6.1 is positioned in the gas-like supercritical regime, having the crossing of the Widom line as a characteristic feature. As a consequence of crossing the Widom line, a thermal breakup mechanism dominates over the mechanical breakup, where it is no longer predominantly moved due to the entrainment of fluid, rather by large density gradients consequent from temperature effects.

After a thorough analysis, a disintegrated core can be observed until $x/d \approx 6$, where the axial density starts to decrease right after the beginning of the chamber. It can also be noted that the numerically obtained rate of decay until $x/d \approx 6$ is slower than that of the experimental data. Although there is no total agreement with the experimental data, a similar trend can be observed from $x/d \approx 6$, where the jet evolution starts to be dominated by the conditions inside the chamber. This outcome is to be predicted, considering that no dense potential core is formed.

Considering that the Widom line has already been crossed in gas-like supercritical conditions, the pseudo-boiling phenomenon is not noted as it would be in the case of liquid-like supercritical conditions. As a consequence, since pseudo-boiling effects do not need to be overcome in gas-like conditions, less thermal energy is required to increase the temperature of the system and decrease the density as it would when compared to a liquid-like case scenario [27].

The axial density distribution for case A6 is represented in Figure 6.2, where the pressure is increased from $4\,\mathrm{MPa}$ to $6\,\mathrm{MPa}$. After analyzing the figure, it can be seen that the increase in pressure conducts to a higher density of the nitrogen jet in the chamber. Such is expected as the ratio ρ_{inj}/ρ_∞ has increased from 3.34 to 5.01 from case A4 to case A6. Several dimen-
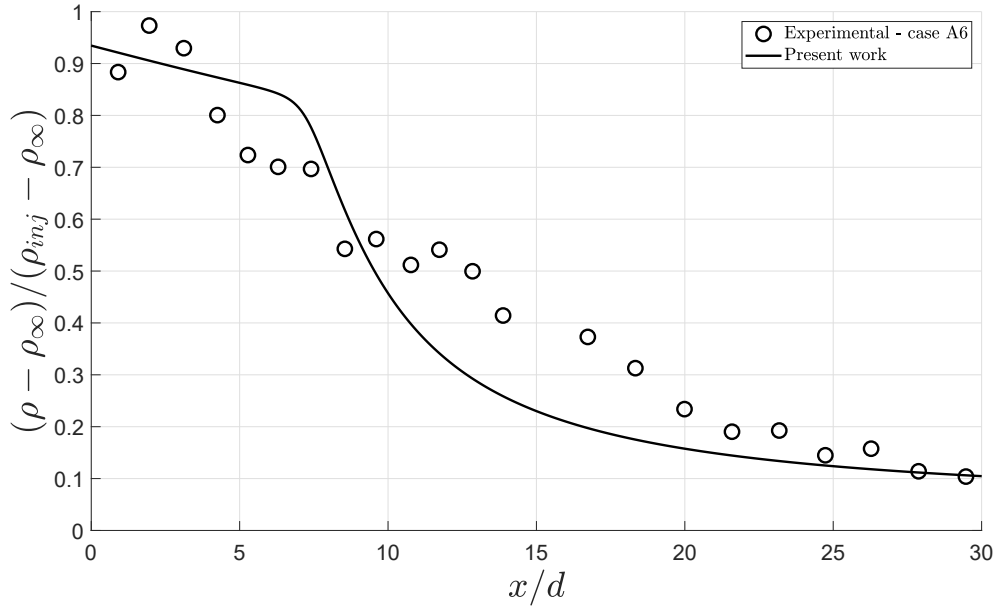
Figure 6.2: Axial density distribution for case A6.

sionless variables of interest for the test cases at study can be consulted in Table 5.2. A direct consequence of this pressure increase is the higher length of the disintegrated core, which is now seen until $x/d \approx 7$. After this stage, the conditions inside the chamber prevail once again, thus dominating the jet development. Again a decrease in axial density is seen as soon as the beginning of the combustion chamber.

From the analysis of Figures 6.1 and 6.2 it can be concluded that despite the different values of pressure and density for cases A4 and A6 (see Table 5.1), they share some resemblance in nature. The fact that both cases share a similar distribution in relation to the pseudo-boiling point is also key for that resemblance. Figure 5.1 portrays the different test cases distribution concerning the pseudo-boiling point.

For further comparison, the density fields of cases A4 and A6 are presented in Figure 6.3, where the differences in density are emphasized. A new variable, r/d, is introduced, where r is the radial distance measured from the origin set at the injector's exit plane, normalized by the injector's diameter, d.

After examining both density fields, it is possible to verify that, inside the injector, i.e., $-15 < x/d < 0$, the heat transfer between the injector walls and the nitrogen jet preponderantly affects the whole field and, in particular, the field at the jet centerline. As a consequence, such leads to the presence of the disintegrated core observed in the previous results.
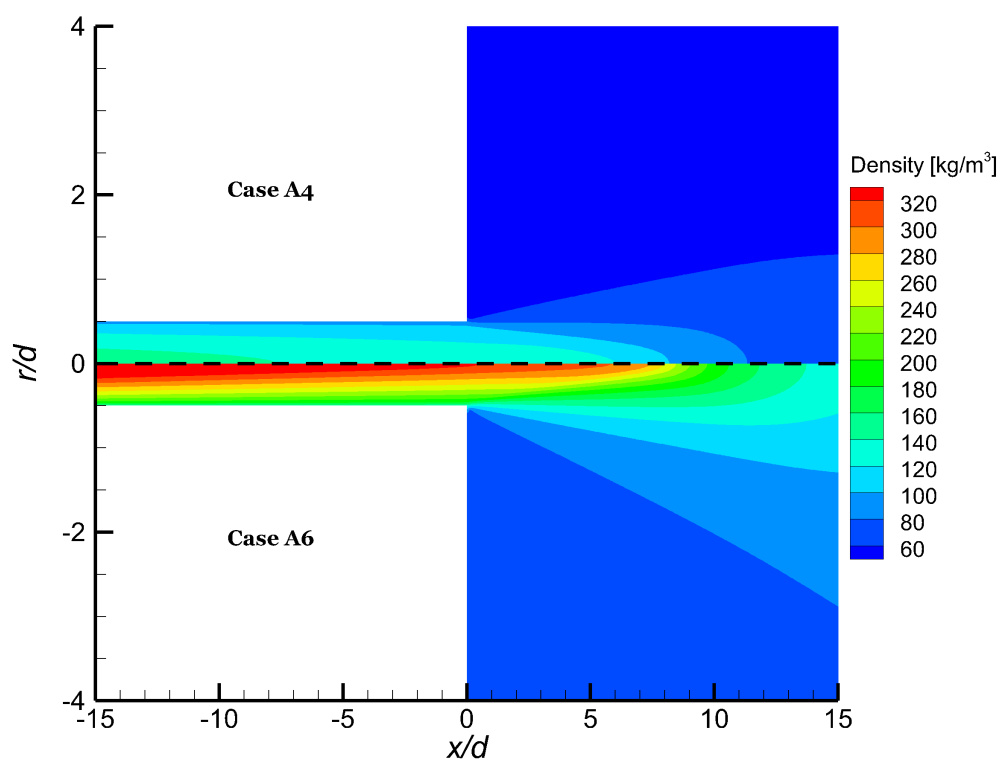
Figure 6.3: Density field comparison between cases A4 and A6.

6.2 Transcritical conditions

Figure 6.4 illustrates the results obtained for the axial density distribution at the jet centerline for the experimental transcritical case B4. In the same way, as it was performed previously, a new grid independence study was conducted owing to operating in a different regime. Thus, it is intended that the new evaluated levels of mesh refinement are capable of assessing the problem in such a way that highly accurate results are generated and, consequently, are independent of the grid resolution.
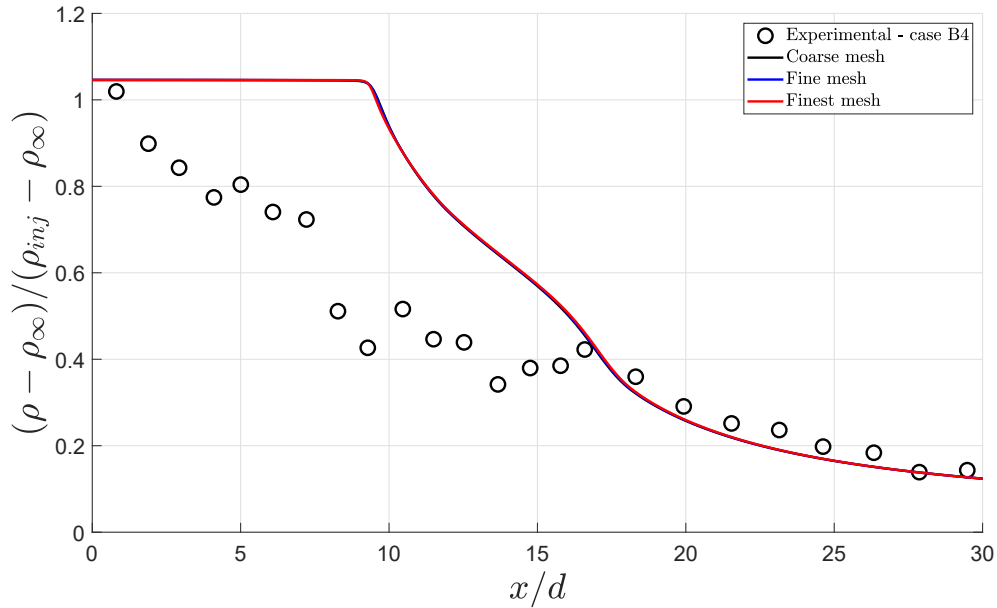

Figure 6.4: Axial density distribution for case B4.

As it can be noted by an analysis of the experimental data, there are considerable fluctuations in the experimental curve. In addition to the change in the second derivative, there is a sudden increase of about 25% in the value of ρ^* over a relatively small space interval at about $x/d = 10$.

According to the definition introduced by Branam and Mayer [43] that define the potential core as the region that contains some portion consisting of only injected fluid and the potential core length as the distance at which the centerline properties remain relatively constant (specifically, density), a potential core length of about $x/d \approx 9.2$ is observed. However, according to the above definitions and the experimental evidence, no potential core is formed.

In this first section (until $x/d \approx 9.2$), the transcritical jet develops until the critical value of temperature is reached. After passing the critical point, the liquid-like supercritical jet will, at a first stage, be unaffected by the conditions inside the chamber. Nevertheless, after that, the conditions in the chamber finally dominate the jet evolution due to the increasing preponderance of the large density gradients ($\rho_{inj}/\rho_\infty = 12.5$) at about $x/d \approx 16$, causing pockets of dense fluid to start to smear the potential core.

Numerical study on nitrogen injection at trans- and supercritical conditions

The axial density distribution for case B6 in contrast to the experimental data is represented in Figure 6.5, where some differences are noted when compared to case B4.
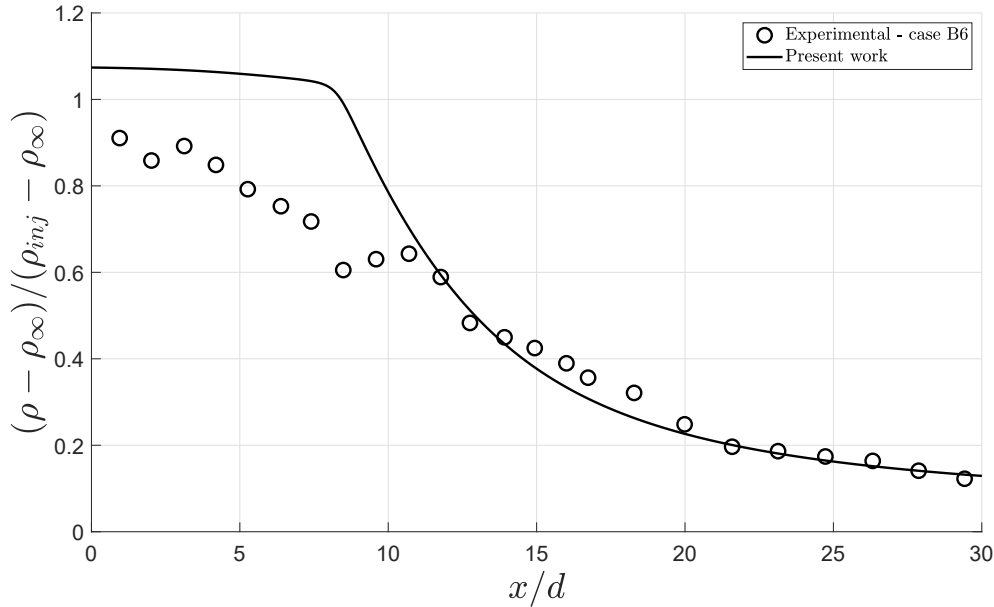

Figure 6.5: Axial density distribution for case B6.

In the first section of case B6, although the density ratio is not as high as in case B4 ($\rho_{inj}/\rho_\infty = 8.99$), the high-density values lead to the same non-concordance between the experimental and the numerical results. As noted in case B4, a slower decay of the centerline density, when compared to the experimental results, is observed until $x/d \approx 7$. After this point, the critical temperature is surpassed, leading the jet to a supercritical liquid-like behavior, where the density starts to decrease owing to the influence of the conditions in the chamber.

After comparing Figures 6.4 and 6.5, it can be seen that, from an overall point of view, a better agreement is found between the experimental and the obtained numerical results for case B6 than for case B4. This outcome could be justified by the closer proximity to the critical pressure of nitrogen ($p_{crit} \approx 3.40$ MPa) of case B4 than case B6, thus portraying that case B4 is more susceptible to experience the influence of the critical point and the region around it.

Furthermore, it is possible to verify that, for both cases, the ability to predict transcritical jet behavior plays a crucial role in the outcome of the simulations, since after the critical temperature is reached and the jets enter a supercritical regime, the numerically obtained results can reproduce its characteristics. However, such happens at higher density levels than those reported in the experimental evidence as a consequence of the lower rate of decay observed for the transcritical region of the jets.

For further analysis, both cases' density fields are represented in Figure 6.6. In this figure, it is possible to see the reason for the referred low-density decay rates, as the evolution of the jets occurs over a broader x/d interval and with reduced differences in density values when

compared to cases A4 and A6, as a consequence of the heat transfer between the injector walls and the nitrogen jets.
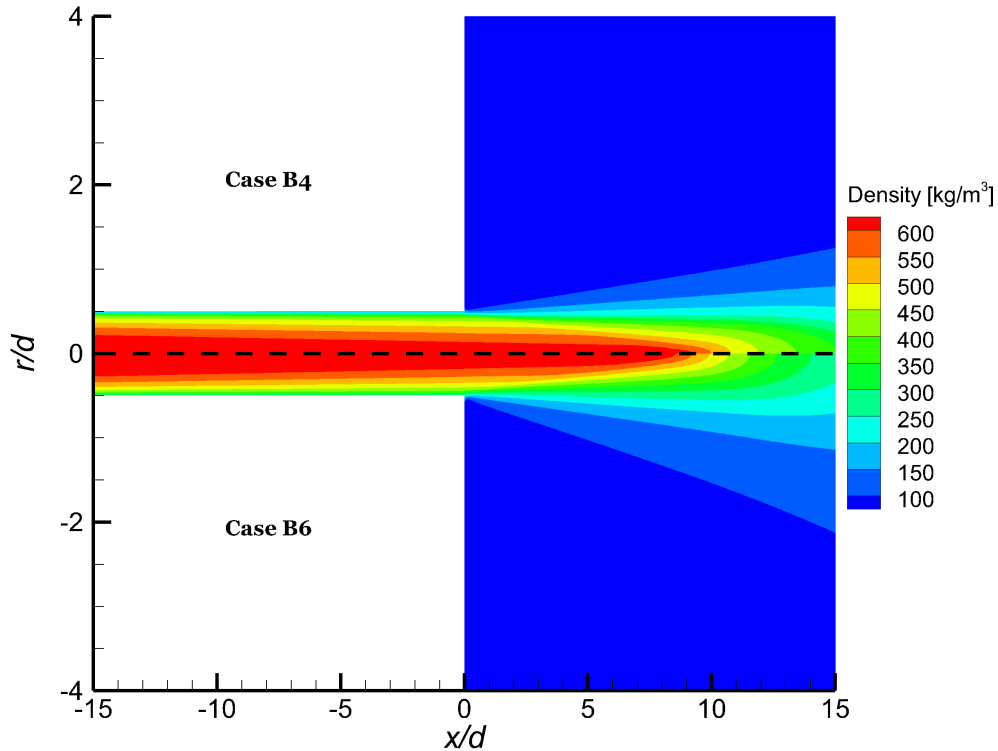

Figure 6.6: Density field comparison between cases B4 and B6.

Figure 6.7 depicts the numerical computed axial density distribution at the jet centerline for the experimental transcritical case C4. As it was carried out previously, a new grid independence study was conducted due to the presence of a different regime, thus ensuring that the results are not only highly accurate but also independent of the grid resolution. For the rationale previously presented, grid independence is achieved for the fine mesh.

As previously seen, a considerable fluctuation of the experimental curve can be observed with the change in the second derivative and a rapid decrease of about 25% near $x/d \approx 2$. The rate of decrease of the computed density is much faster until $x/d \approx 15$, where the calculated density values continue to decrease even further approaching the experimental data.

From the interpretation of the figure, a potential core of about $x/d \approx 8.6$ can be observed. However, according to the experimental data, no potential core is formed. Until this point, the transcritical jet develops until reaching the critical temperature value. However, the rate of decay obtained from the computations does not match the experimental results.

After surpassing the critical point, the nitrogen is then in a supercritical liquid-like state where it will, at first, be unaffected by the conditions in the chamber. Nevertheless, as it
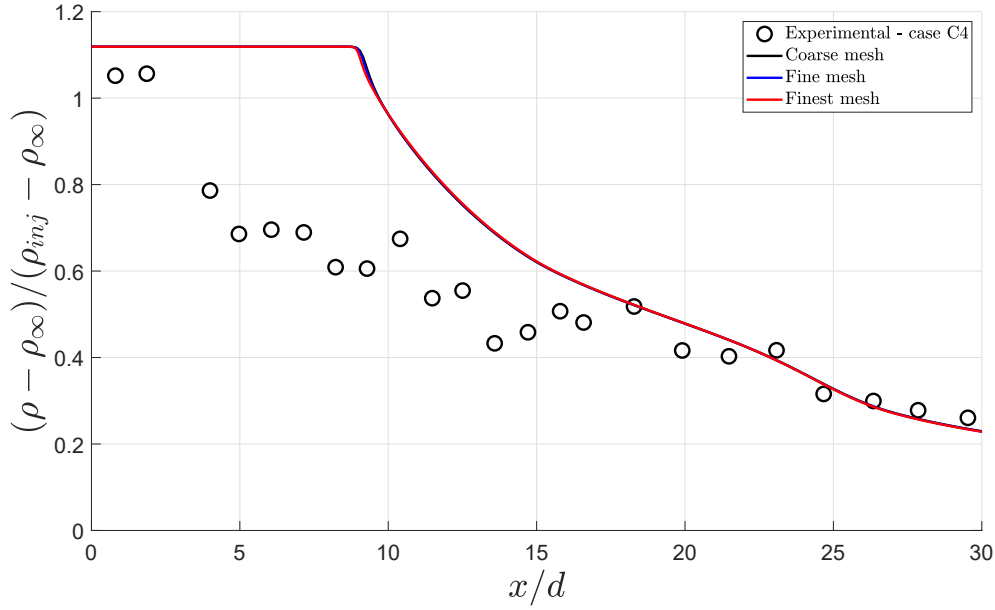
Figure 6.7: Axial density distribution for case C4.

happened for case B4, the conditions in the chamber ultimately dominate over the jet evolution, as the large density gradients ($\rho_{inj}/\rho_\infty = 15.7$) start to prevail in the jet disintegration mechanism, leading to pockets of dense fluid to break.

Figure 6.8 shows a comparison between the computed axial density distribution for case C6 and the experimental evidence, that when in contrast to case C4, some resemblances and differences are noted.
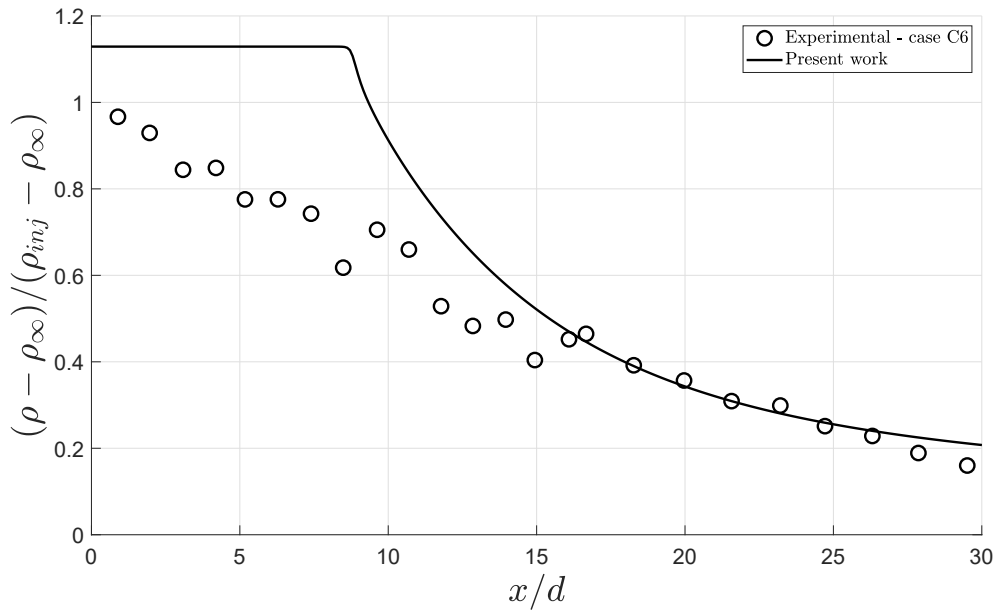

Figure 6.8: Axial density distribution for case C6.

Numerical study on nitrogen injection at trans- and supercritical conditions

In the first section of case C6, the high-density values ($\rho_{inj}/\rho_\infty = 10.06$) lead to a similar disparity between the experimental and numerical results. While analyzing the numerical results, it can be observed a potential core until $x/d \approx 8.2$, as opposed to the corresponding experimental data. Experimentally, no core is predicted, and as soon as the combustion chamber begins, the axial density starts to decrease. Nevertheless, after this point, the temperature exceeds the critical temperature value, where a decrease in density can be seen due to the influence of the conditions in the chamber, thus leading the jet to a liquid-like supercritical behavior.

This time, when comparing cases C4 and C6, similar conclusions can be drawn from the analysis of both axial density distributions. From a general perspective, case C6 presents a better agreement between the experimental and numerical computations than case C4. Such could be justified once more by the closer proximity to the critical pressure of nitrogen of case C4 than case C6, thus contributing to the possibility that this proximity can have a preponderant role in the results.

Analogously, the comparison of both density fields of cases C4 and C6 is made in Figure 6.9. As heat transfer between the injector walls and the nitrogen jets can be observed, it is also possible to see the density stratification and the different jet evolution in space, considering both cases use distinct injection values (see Tables 5.1 and 5.2).
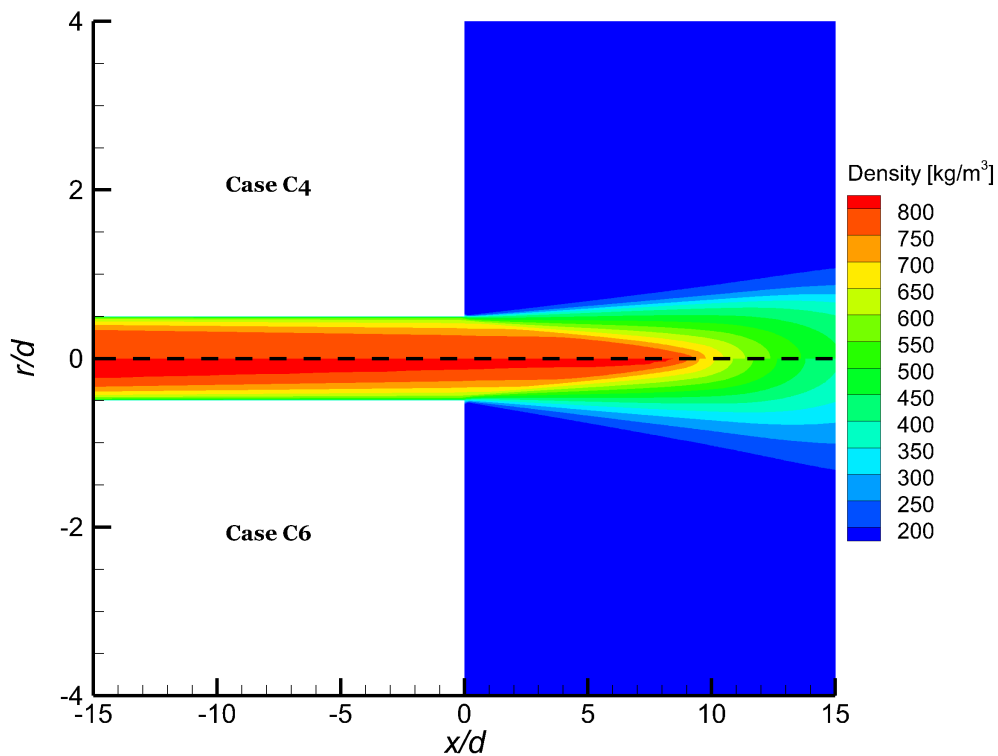

Figure 6.9: Density field comparison between cases C4 and C6.

Numerical study on nitrogen injection at trans- and supercritical conditions

During the presentation and comparison of the numerically obtained results with the experiments, some considerable differences were noticed for transcritical conditions. These differences may be related to the nature of the measurements and the employed measurement technique, the Raman scattering technique. Additionally, it must be taken into account that the experimental measurements carried out by Oschwald and Schik [17] rely on the usage of a considerably complex measurement technique, for which some assumptions need to be considered. For instance, the authors assume that the Raman cross-section is constant.

Under the authors' procedure, density is determined using the following relation

$$\rho(r) = \frac{\rho_\infty}{I_\infty} \cdot I(r) \quad (6.2)$$

where I is the measured Raman signal intensity, and I_∞ is the average signal at specific radial positions.

However, the Raman signal intensity calculation may present some challenges. The radial distribution of the Raman signal is obtained by integrating the detected signal perpendicular to the direction of the laser beam. Thus, the measured Raman signal intensity, I, can be expressed, in a simplified way, as

$$I = \beta \vartheta \rho E_{\text{laser}} \quad (6.3)$$

where β is a constant that includes equipment efficiency, geometry, and dependent factors that is determined by experimental calibration, ϑ the Raman cross-section, ρ the species density, and E_{laser} the laser energy.

Despite the authors' knowledge of the dependence of the Raman cross-section on density, they did not correct their measurements due to a lack of accurate data. Thus, the densities presented by the authors are derived from Raman intensities under the assumption of a constant Raman cross-section.

Regarding the experimental results, the authors point out that this assumption does not affect the results of cases A4 and A6. However, that is not observed for cases B and C, where an underestimation of the determined densities in the cold, dense flow region is expected. According to the authors' prediction, the obtained results may have an associated error of 30% for the worst cases. As a result, the experimental axial density distributions of cases B and C can be seriously under-predicted, thus potentially leading to the noticeable disparity of the results.

Another possibility that can explain the accentuated over-prediction of the numerical computations over the experimental data is related to Raman scattering constraints [61]. For the correction of the Raman images, it is required the separation of the Raman signal from any background signal contribution. However, under these experimental conditions, there are sharp density gradients that consequently result in large gradients of the refractive index. In

addition, there are more effects of focussing within the cryogenic jet that play a significant role in leading to an optical breakdown. In these regions, the isolation of the Raman signal is not possible, where a reduction in laser power must exist so that no breakdown occurs.

Furthermore, under partially supercritical conditions, difficulties arise from the fact that the Raman cross-section of liquid nitrogen is different from that of gaseous nitrogen. In addition, there is no way to distinguish in a camera image where the transition lies between liquid and gas and where to apply the respective cross-section. The reduction in laser power is also a reality in these conditions to prevent any optical breakdown. In this subject, Mayer et al. [61] also adds that in experiments close to critical conditions, it is not possible to avoid optical breakdown completely. Thus, we could be confronting the image saturation issue of Raman scattering, which has the proneness to under-predict density when dealing with large density values as the ones we operate in this work.

In the description of the measurement procedure, Oschwald and Schik [17] report that the cryogenic nitrogen was only injected during the time of a measurement at one location to avoid the waste of nitrogen when moving the optics to a new measurement position. As a result, after the beginning of the measurement procedure at a new location, there was a transient time during which the fluid system cooled down. Figure 2.5 highlights the possibility that a minor temperature variation may be associated with a considerable density variation. Despite the care taken by the authors, a slight variation in the temperature determination may be associated with the observed fluctuations in the experimental evidence. The authors also add that the experimental case C4 suffers from beam steering and high background signal, thus affecting the accuracy of measurements. As a consequence of the large density gradients in the near injector region, the evidence retrieved at the first location downstream of the injector is not trustworthy [17].

Additionally, Oschwald et al. and Mayer et al. [17, 61] pointed out that measurements resorting to the Raman scattering technique in high-density regions can also face additional challenges due to the associated reduction of refracted radiation.

When radiation, e.g., a light beam irradiates a transparent medium, some fraction of the light is scattered in different directions. If the transparent medium contains particles of molecular dimension, reduced scattered radiation with the same wavelength is detected. When such happens, i.e., inelastic collisions where the energy of the impacting photon remains unaltered, it is termed as Rayleigh scattering [58]. Raman and Krishnan [93] discovered in 1928 that additional diffuse radiation, besides that of Rayleigh scattering, is also present, having a different wavelength. This wavelength shift represents the energy that is emitted or absorbed by molecules. However, the resultant frequency depends upon the chemical structure of the molecules responsible for the scattering. Such represents a fundamental feature of Raman scattering, as in this way, the resultant frequency can be used to identify the medium, i.e., the substance in question. Furthermore, the widespread use of this technique in experimental campaigns involving nitrogen injection under conditions such as those in this study

can be explained, considering that nitrogen is one of the substances identifiable by Raman scattering.

Considering the working principles of the Raman scattering, the referred reduction in refracted radiation is due to the high refraction index that redirects a fraction of the signal along the jet axis. Therefore, the density values measured in this region can be reasonably underestimated. Mayer et al. [61] reported that the measured maximum density is often lower than the density that corresponds to the measured temperature and pressure. The authors then exemplify stating that in case 3, the maximum measured density is $400 \text{ kg} \cdot \text{m}^{-3}$, whereas, for the reported injection temperature of 126.9 K and pressure of 4 MPa, the corresponding density value is $457.82 \text{ kg} \cdot \text{m}^{-3}$ (data from [26]). Such represents a density prediction relative error of 13.1%. While such constitutes a significant source of error along the potential core, it has less influence downstream, considering that both the density gradients and the refraction effects start to decrease. As a result, such can explain the overestimation of the numerically obtained density values in the injector near region when compared to the experimental data and the better agreement between both towards downstream.

Chapter 7

Conclusions and Future Work

In the present numerical study, the behavior of nitrogen jets under transcritical and super-critical gas-like conditions was numerically predicted, resorting to a RANS-based approach. As a result, following the experimental data of [17], the injection of a single liquid nitrogen jet into a chamber filled with supercritical nitrogen was investigated for different experimental cases, varying the chamber pressure levels and the temperature and velocity injection levels. Both the injector and the combustion chamber were considered in the computational domain, with emphasis on the inclusion of the isothermal injector wall boundary condition.

The steady-state Favre-averaged conservation equations of mass, momentum, and energy were used to deal with the incompressible but variable density conditions, characteristic of the test cases at study. Hence, the density-weighted conservation equations were employed to account for the density variation effects. Concerning the turbulence modeling, the adopted method was through the Boussinesq hypothesis and consequent modeling of the turbulent viscosity, resorting to the standard $k - \varepsilon$ turbulence model. As the ideal gas law is no longer valid to describe the fluid behavior due to the highly nonlinear behavior of the thermophysical properties at these conditions, the real gas behavior is addressed by resorting to the cubic Peng-Robinson EoS and applying an accurate formulation to the transport properties. A pressure-based algorithm was adopted where the velocity and pressure fields were solved simultaneously. A staggered grid configuration was implemented along with the QUICK scheme for the advective terms and second-order central differencing scheme for the diffusive terms to prevent the appearance of non-physical pressure oscillations and the odd-even decoupling of pressure and velocity.

With this, a mathematical formulation based on an incompressible but variable density approach capable of dealing with the strong temperature and density gradients and the non-linear behavior of the thermodynamic properties characteristic of the flows inside the combustion chamber of liquid rocket engines was proposed. Following the recent breakthroughs in the literature, the inclusion of a thermal breakup mechanism based on the pseudo-boiling theory to the classical mechanical breakup mechanism provided valuable insights into the supercritical fluid behavior.

Six experimental conditions were analyzed, where two of those (cases A4 and A6) concerned supercritical injection cases, and the remaining four (cases B4, B6, and C4, C6) regarded transcritical injection configurations. For each experimental condition, a comparison between the numerically obtained axial density distributions at the jet centerline and the exper-

imental results of Oschwald was conducted. In addition, density field comparisons between each pair of the respective experimental conditions were performed where the effects of the two used different chamber pressure levels (4 and 6 MPa) on the supercritical fluid behavior could also be assessed.

Regarding the gas-like supercritical injection cases (cases A4 and A6), the numerically obtained results attained a good approximation with the experimental data, both in terms of the predicted jet behavior and magnitude of the experimental evidence. Albeit some differences in the near injector region where the axial density started to decrease right after the beginning of the chamber, a disintegrated core was predicted in both cases. Considering the predictions of disintegrated cores and that both cases are positioned in the gas-like supercritical regime, with a characteristic feature of having already crossed the Widom line, these may evidence the preponderance of the thermal breakdown mechanism under these conditions. As the analysis of both cases' density fields depicted, the heat transfer between the injector walls and the cryogenic nitrogen jet inside the injector preponderantly affected the entire field and, in particular, the field at the jet centerline. Such led to the presence of the disintegrated cores. Despite the slightly higher disintegrated core length prediction for the A6 case as a consequence of the pressure increase, both cases share a resemblance in nature, albeit the different pressure and density values. The similar distribution concerning the pseudo-boiling point of both cases was also crucial for this resemblance.

With regard to the transcritical injection cases (cases B4, B6, and C4, C6), only an approximation in jet behavior was achieved. Significant fluctuations were found in the experimental curve for each of these case conditions. In addition, against the experimental data in every experimental condition, a potential core was numerically predicted. Concerning the transcritical portion of the jet, a slower rate of decay of the axial density distribution was attained in relation to the experimental evidence. The reason for these low-density decay rates is a consequence of the heat transfer between the injector walls and the nitrogen jets, as jet evolution takes place over broader intervals and with reduced differences in density when compared to supercritical injection cases A4 and A6. After the potential core region, the critical temperature is exceeded, where the jet presents a liquid-like supercritical behavior, and density starts to decrease owing to the influence of the conditions inside the chamber.

From a general point of view, the axial density distributions obtained from the numerical computations for cases B6 and C6 were in better agreement with the experimental evidence than those of cases B4 and C4, respectively. This consequence could be justified by the closer proximity to the critical pressure of nitrogen of cases B4 and C4 than those of cases B6 and C6, thus revealing the more proneness of cases B4 and C4 to suffer the influence of the critical point and the region around it.

It was seen for these four transcritical injection cases that the capability to predict transcritical jet behavior is preponderant in the obtained numerical results. After the critical temperature value was attained and the nitrogen jets entered the supercritical domain the numerical

solver could replicate their characteristics. However, such happened at higher density levels than those of the experimental data owed to the lower-density decay rates obtained for the transcritical portions of the jets.

In addition, some challenges arose from the use of Raman scattering, which was the measurement technique used in the experimental study [17]. Between some simplifications employed and the nature of the measurements, some considerable differences were obtained for the transcritical injection conditions. Some possible causes for these differences were presented, e.g., possible measurements errors owed to the measurement technique complexity and associated constraints under these severe conditions. However, the authors recognized the admittance of some errors in the measurements, resulting from the considered assumptions. Although these assumptions did not affect the results of cases A4 and A6, the authors predicted that the results obtained for cases B4, B6, and C4, C6 may have an associated error of 30% for the worst cases. As a result, the experimental axial density distributions for these cases could be severely under-predicted, thus potentially leading to the noticeable disparity of the experimental evidence. Therefore, the overestimation of the numerically obtained density values in the injector near region when compared to the experimental evidence and the better agreement between both towards downstream thus could be explained.

With the validation of the proposed thermodynamic and numerical formulations for the injection of nitrogen jets at transcritical and supercritical gas-like conditions, the following step could be the acquisition of more accurate experimental data sets to allow the proper assessment of the numerical solver performance in the capture of transcritical fluid behavior. In particular, the experimental evidence improvement inside the injector and at the combustion chamber entrance would be of the utmost importance, considering that it was demonstrated the global preponderance of the phenomena that occur there.

Bibliography

[1] Ito, Y., "Heat Transfer of Supercritical Fluid Flows and Compressible Flows," in *Heat Exchangers - Advanced Features and Applications*, 2017, no. 6, doi: http://dx.doi.org/10.5772/65931. 1, 9

[2] Sengers, J. M. H. L., *Supercritical Fluids: Their Properties and Applications*, ser. NATO Science Series (Series E: Applied Sciences). Springer, Dordrecht, 2000, vol. 366, ch. 1, pp. 1–29, doi: http://dx.doi.org/10.1007/978-94-011-3929-8_1. 1

[3] Lockwood, J. and Hazlett, R., *Volcanoes: Global Perspectives*, 1st ed. Wiley-Blackwell, Oxford, England, 2010, ISBN: 978-1-405-16249-4. 1

[4] Esposito, W., *Venus II: Geology, Geophysics, Atmosphere, and Solar Wind Environment*. University of Arizona Press, Tucson, Arizona, 1997, ISBN: 978-0816518302. 1

[5] Lebonnois, S. and Schubert, G., "The deep atmosphere of Venus and the possible role of density-driven separation of CO2 and N2," *Nature Geoscience*, vol. 10, no. 7, pp. 473–477, 2017, doi: http://dx.doi.org/10.1038/ngeo2971. 1

[6] Pioro, I. and Mokry, S., "Thermophysical Properties at Critical and Supercritical Conditions," in *Heat Transfer - Theoretical Analysis, Experimental Investigations and Industrial Systems*, 2011, no. 22, doi: http://dx.doi.org/10.5772/13790. 1, 7

[7] Knez, Z., Markočič, E., Leitgeb, M., Primožič, M., Hrnčič, M. K., and Škerget, M., "Industrial applications of supercritical fluids: A review," *Energy*, vol. 77, pp. 235–243, 2014, doi: http://dx.doi.org/10.1016/j.energy.2014.07.044. 2

[8] Brunner, G., "Applications of Supercritical Fluids," *Annual Review of Chemical and Biomolecular Engineering*, vol. 1, no. 1, pp. 321–342, 2010, doi: http://dx.doi.org/10.1146/annurev-chembioeng-073009-101311. 2

[9] Lacaze, G., Misdariis, A., and Ruiz, A. and Oefelein, J., "Analysis of high-pressure Diesel fuel injection processes using LES with real-fluid thermodynamics and transport," *Proceedings of the Combustion Institute*, vol. 35, no. 2, pp. 1603–1611, 2015, doi: http://dx.doi.org/10.1016/j.proci.2014.06.072. 2

[10] Oschwald, M., Smith, J. J., Branam, R., Hussong, J., Schik, A., and Chehroudi, B. and Talley, D., "Injection of Fluids into Supercritical Environments," *Combustion Science and Technology*, vol. 178, no. 1-3, pp. 49–100, 2006, doi: http://dx.doi.org/10.1080/00102200500292464. 2, 3, 7, 9, 10, 11, 14

[11] Yang, V., Habiballah, M., and Hulka, J. and Popp, M. (Eds.), *Liquid Rocket Thrust Chambers - Aspects of Modeling, Analysis, and Design - Progress in Astronautics and Aeronautics, Volume 200.* American Institute of Aeronautics and Astronautics, 2004, ISBN: 978-1-56347-223-7. 2

[12] Chehroudi, B., Talley, D., and Coy, E., "Initial Growth Rate and Visual Characteristics of a Round Jet into a Sub- to Supercritical Environment of Relevance to Rocket, Gas Turbine, and Diesel Engines," in *37th Aerospace Sciences Meeting and Exhibit.* American Institute of Aeronautics and Astronautics, 1999, doi: http://dx.doi.org/10.2514/6.1999-206. 2, 14, 32

[13] Anderson Jr., J., *Introduction to Flight*, 8th ed. McGraw-Hill Education, 2016, ISBN: 978-0078027673. 2

[14] Aerojet Rocketdyne, Los Angeles, California, "RS-25 Propulsion System," Aerojet Rocketdyne, Tech. Rep., 2019. 3

[15] Azuma, N., Kojima, M., Kobayashi, T., Okita, K., and Motomura, T. and Niiyama, K., "The Development Status of LE-9 Engine Turbopumps for H3 Launch Vehicle," in *AIAA Propulsion and Energy 2019 Forum.* American Institute of Aeronautics and Astronautics, 2019, doi: http://dx.doi.org/10.2514/6.2019-4430. 3

[16] Office of Safety and Mission Assurance, National Aeronautics and Space Administration, *Space Launch Report: SpaceX Falcon 9 v1.1 Data Sheet*, September 2017. 3

[17] Oschwald, M. and Schik, A., "Supercritical nitrogen free jet investigated by spontaneous Raman scattering," *Experiments in Fluids*, vol. 27, no. 6, pp. 497–506, 1999, doi: http://dx.doi.org/10.1007/s003480050374. 3, 22, 39, 57, 58, 59, 61, 70, 71, 73, 75

[18] Barata, J. M. M. and Gökalp, I. and Silva, A. R. R., "Numerical study of cryogenic jets under supercritical conditions," *Journal of Propulsion and Power*, vol. 19, no. 1, pp. 142–147, 2003, doi: http://dx.doi.org/10.2514/2.6090. 4, 23, 32, 38

[19] Antunes, E., "Modelling of Transcritical Jets by the use of a Real Fluid Equation of State," PhD thesis, University of Beira Interior, 2018. 4

[20] Magalhães, L., Carvalho, F., and Silva, A. and Barata, J., "Turbulence Modeling Insights into Supercritical Nitrogen Mixing Layers," *Energies*, vol. 13, no. 7, p. 1586, 2020, doi: http://dx.doi.org/10.3390/en13071586. 4, 21, 22, 23, 38

[21] Magalhães, L. B. and Silva, A. R. R. and Barata, J. M. M., "Contribution to the physical description of supercritical cold flow injection: The case of nitrogen," *Acta Astronautica*, vol. 190, pp. 251–260, 2022, doi:

http://dx.doi.org/10.1016/j.actaastro.2021.09.044. 4, 22, 23

[22] Park, T. S., "LES and RANS simulations of cryogenic liquid nitrogen jets," *The Journal of Supercritical Fluids*, vol. 72, pp. 232–247, 2012, doi: http://dx.doi.org/10.1016/j.supflu.2012.09.004. 7, 19, 22, 23, 38, 42

[23] Zong, N., Meng, H., Hsieh, S.-Y., and Yang, V., "A numerical study of cryogenic fluid injection and mixing under supercritical conditions," *Physics of Fluids*, vol. 16, no. 12, pp. 4248–4261, 2004, doi: http://dx.doi.org/10.1063/1.1795011. 7

[24] Banuti, D. T., Raju, M., Ma, P., and Ihme, M. and Hickey, J., "Seven questions about supercritical fluids - towards a new fluid state diagram," in *55th AIAA Aerospace Sciences Meeting*. American Institute of Aeronautics and Astronautics, 2017, doi: http://dx.doi.org/10.2514/6.2017-1106. 7

[25] Bellan, J., "Supercritical (and subcritical) fluid behavior and modeling: drops, streams, shear and mixing layers, jets and sprays," *Progress in Energy and Combustion Science*, vol. 26, no. 4-6, pp. 329–366, 2000, doi: http://dx.doi.org/10.1016/s0360-1285(00)00008-3. 7

[26] Linstrom, P. and Mallard, W. (Eds.), "NIST Chemistry WebBook, NIST Standard Reference Database 69," *National Institute of Standards and Technology*, 1997, doi: http://dx.doi.org/10.18434/T4D303. 8, 10, 11, 12, 18, 58, 72

[27] Kim, T. and Kim, Y. and Kim, S., "Numerical study of cryogenic liquid nitrogen jets at supercritical pressures," *The Journal of Supercritical Fluids*, vol. 56, no. 2, pp. 152–163, 2011, doi: http://dx.doi.org/10.1016/j.supflu.2010.12.008. 9, 20, 22, 23, 42, 62

[28] Banuti, D. T. and Raju, M. and Ihme, M., "Between supercritical liquids and gases – Reconciling dynamic and thermodynamic state transitions," *The Journal of Supercritical Fluids*, vol. 165, p. 104895, 2020, doi: http://dx.doi.org/10.1016/j.supflu.2020.104895. 10

[29] Santoro, M. and Gorelli, F. A., "Structural changes in supercritical fluids at high pressures," *Physical Review B*, vol. 77, no. 21, 2008, doi: http://dx.doi.org/10.1103/PhysRevB.77.212103. 10

[30] Simeoni, G. G., Bryk, T., Gorelli, F. A., Krisch, M., Ruocco, G., and Santoro, M. and Scopigno, T., "The Widom line as the crossover between liquid-like and gas-like behaviour in supercritical fluids," *Nature Physics*, vol. 6, no. 7, pp. 503–507, 2010, doi: http://dx.doi.org/10.1038/NPHYS1683. 10

[31] Maxim, F., Contescu, C., Boillat, P., Niceno, B., Karalis, K., and Testino,

A. and Ludwig, C., "Visualization of supercritical water pseudo-boiling at Widom line crossover," *Nature Communications*, vol. 10, no. 1, 2019, doi: http://dx.doi.org/10.1038/s41467-019-12117-5. 10

[32] Banuti, D. T., "Crossing the Widom-line – supercritical pseudo-boiling," *The Journal of Supercritical Fluids*, vol. 98, pp. 12–16, 2015, doi: http://dx.doi.org/10.1016/j.supflu.2014.12.019. 11, 12, 18

[33] Mayer, W. and Tamura, H., "Propellant Injection in a Liquid Oxygen/Gaseous Hydrogen Rocket Engine," *Journal of Propulsion and Power*, vol. 12, no. 6, pp. 1137–1147, 1996, doi: http://dx.doi.org/10.2514/3.24154. 11

[34] Mayer, W., Schik, A., and Schäffler, M. and Tamura, H., "Injection and Mixing Processes in High-Pressure Liquid Oxygen/Gaseous Hydrogen Rocket Combustors," *Journal of Propulsion and Power*, vol. 16, no. 5, pp. 823–828, 2000, doi: http://dx.doi.org/10.2514/2.5647. 11

[35] Banuti, D., "Thermodynamic Analysis and Numerical Modeling of Supercritical Injection," PhD thesis, University of Stuttgart, 2015. 12, 15, 18, 42

[36] Banuti, D. T. and Hannemann, K., "The absence of a dense potential core in supercritical injection: A thermal break-up mechanism," *Physics of Fluids*, vol. 28, no. 3, p. 035103, 2016, doi: http://dx.doi.org/10.1063/1.4943038. 12, 13, 16, 17, 19, 21, 22, 23

[37] Chehroudi, B., "Recent Experimental Efforts on High-Pressure Supercritical Injection for Liquid Rockets and Their Implications," *International Journal of Aerospace Engineering*, vol. 2012, pp. 1–31, 2012, doi: http://dx.doi.org/10.1155/2012/121802. 13, 14, 15

[38] Reitz, R. and Bracco, F., "On the Dependence of Spray Angle and Other Spray Parameters on Nozzle Design and Operating Conditions," 1979, doi: http://dx.doi.org/10.4271/790494. 14

[39] Rayleigh, L., "On The Instability Of Jets," *Proceedings of the London Mathematical Society*, vol. s1-10, no. 1, pp. 4–13, 1878, doi: http://dx.doi.org/10.1112/plms/s1-10.1.4. 14

[40] Lagarza-Cortés, C., Ramírez-Cruz, J., Salinas-Vázquez, M., and Vicente-Rodríguez, W. and Cubos-Ramírez, J. M., "Large-eddy simulation of transcritical and supercritical jets immersed in a quiescent environment," *Physics of Fluids*, vol. 31, no. 2, p. 025104, 2019, doi: http://dx.doi.org/10.1063/1.5054797. 14, 22

[41] Schmitt, T., Selle, L., and Cuenot, B. and Poinsot, T., "Large-Eddy Simulation of tran-

scritical flows," *Comptes Rendus Mecanique*, vol. 337, no. 6, pp. 528–538, 2009, doi: http://dx.doi.org/10.1016/j.crme.2009.06.022. 14, 22, 23, 42

[42] Müller, H., Niedermeier, C. A., Jarczyk, M., Pfitzner, M., and Hickel, S. and Adams, N. A., "Large Eddy Simulation of Trans- and Supercritical Injection," *Progress in Propulsion Physics*, vol. 8, pp. 5–24, 2016, doi: http://dx.doi.org/10.2514/6.2012-1270. 14, 22, 23, 42, 53

[43] Branam, R. and Mayer, W., "Characterization of Cryogenic Injection at Supercritical Pressure," *Journal of Propulsion and Power*, vol. 19, no. 3, pp. 342–355, 2003, doi: http://dx.doi.org/10.2514/2.6138. 15, 42, 65

[44] Ries, F. and Janicka, J. and Sadiki, A., "Thermal Transport and Entropy Production Mechanisms in a Turbulent Round Jet at Supercritical Thermodynamic Conditions," *Entropy*, vol. 19, no. 8, p. 404, 2017, doi: http://dx.doi.org/10.3390/e19080404. 16, 22, 23, 42

[45] Ries, F., Obando, P., Shevchuck, I., and Janicka, J. and Sadiki, A., "Numerical analysis of turbulent flow dynamics and heat transport in a round jet at supercritical conditions," *International Journal of Heat and Fluid Flow*, vol. 66, pp. 172–184, 2017, doi: http://dx.doi.org/10.1016/j.ijheatfluidflow.2017.06.007. 16, 22, 23, 42

[46] Soave, G., "Equilibrium constants from a modified Redlich-Kwong equation of state," *Chemical Engineering Science*, vol. 27, no. 6, pp. 1197–1203, 1972, doi: http://dx.doi.org/10.1016/0009-2509(72)80096-4. 19, 20, 21

[47] Graboski, M. S. and Daubert, T. E., "A Modified Soave Equation of State for Phase Equilibrium Calculations. 1. Hydrocarbon Systems," *Industrial & Engineering Chemistry Process Design and Development*, vol. 17, no. 4, pp. 443–448, 1978, doi: http://dx.doi.org/10.1021/i260068a009. 19, 20

[48] Peng, D. and Robinson, D. B., "A new two-constant equation of state," *Industrial & Engineering Chemistry Fundamentals*, vol. 15, no. 1, pp. 59–64, 1976, doi: http://dx.doi.org/10.1021/i160057a011. 20, 21, 42

[49] Span, R. and Wagner, W., "Equations of State for Technical Applications. I. Simultaneously Optimized Functional Forms for Nonpolar and Polar Fluids," *International Journal of Thermophysics*, vol. 24, no. 1, pp. 1–39, 2003, doi: http://dx.doi.org/10.1023/A:1022390430888. 20, 21

[50] Banuti, D. T. and Hannemann, K., "Real Gas Library in Continuous Phase Propellant Injection Model for Liquid Rocket Engines," in *49th AIAA/ASME/SAE/ASEE Joint Propulsion Conference*, ser. (AIAA 2016-4068),

2013, doi: http://dx.doi.org/10.2514/6.2013-4068. 21

[51] Span, R., Lemmon, E. W., Jacobsen, R. T., and Wagner, W. and Yokozeki, A., "A Reference Equation of State for the Thermodynamic Properties of Nitrogen for Temperatures from 63.151 to 1000 K and Pressures to 2200 MPa," *Journal of Physical and Chemical Reference Data*, vol. 29, no. 6, pp. 1361–1433, 2000, doi: http://dx.doi.org/10.1063/1.1349047. 21

[52] Younglove, B. A., "Thermophysical properties of fluids. I. Argon, ethylene, parahydrogen, nitrogen, nitrogen rifluoride and oxygen," *Journal of Physical and Chemical Reference Data*, vol. 11, 1982, doi: http://dx.doi.org/10.1063/1.555731. 21

[53] Span, R., Lemmon, E. W., and Jacobsen, R. T. and Wagner, W., "A Reference Quality Equation of State for Nitrogen," *International Journal of Thermophysics*, vol. 19, no. 4, pp. 1121–1132, 1998, doi: http://dx.doi.org/10.1023/A:1022689625833. 21, 47

[54] Yang, V., "Modeling of supercritical vaporization, mixing, and combustion processes in liquid-fueled propulsion systems," *Proceedings of the Combustion Institute*, vol. 28, no. 1, pp. 925–942, 2000, doi: http://dx.doi.org/10.1016/S0082-0784(00)80299-4. 21

[55] Oschwald, M. and Schneider, G. and Clauss, W., "Application of Visualization Techniques and Quantitative Optical Diagnostics for the Investigation of Supercritical Jet Atomization," 2005. 22

[56] Decker, M., Schik, A., and Meier, U. E. and Stricker, W., "Quantitative Raman imaging investigations of mixing phenomena in high-pressure cryogenic jets," *Applied Optics*, vol. 37, no. 24, p. 5620, 1998, doi: http://dx.doi.org/10.1364/ao.37.005620. 22

[57] Castrejón-García, R., Castrejón-Pita, R., and Martin, G. D. and Hutchings, I. M., "The shadowgraph imaging technique and its modern application to fluid jets and drops," *Revista Mexicana de Física*, vol. 57, no. 3, pp. 266–275, 2011. 22

[58] Chehroudi, B., Cohn, R., and Talley, D. and Badakhshan, A., "Raman Scattering Measurements in the Initial Region of Sub- and Supercritical Jets," in *36th AIAA/ASME/SAE/ASEE Joint Propulsion Conference and Exhibit*. American Institute of Aeronautics and Astronautics, 2000, doi: http://dx.doi.org/10.2514/6.2000-3392. 22, 71

[59] Oschwald, M. and Micci, M. M., "Spreading Angle and Centerline Variation of Density of Supercritical Nitrogen Jets," vol. 12, no. 1-3, 2002, pp. 91–106, doi: http://dx.doi.org/10.1615/AtomizSpr.v12.i123.50. 22

[60] Chehroudi, B. and Talley, D. and Coy, E., "Visual characteristics and initial growth rates of round cryogenic jets at subcritical and supercritical pressures," *Physics of Fluids*, vol. 14, no. 2, pp. 850–861, 2002, doi: http://dx.doi.org/10.1063/1.1430735. 22

[61] Mayer, W., Telaar, J., Branam, R., and Schneider, G. and Hussong, J., "Raman Measurements of Cryogenic Injection at Supercritical Pressure," *Heat and Mass Transfer*, vol. 39, no. 8-9, pp. 709–719, 2003, doi: http://dx.doi.org/10.1007/s00231-002-0315-x. 22, 23, 38, 39, 70, 71, 72

[62] Schmitt, T., Selle, L., and Ruiz, A. and Cuenot, B., "Large-Eddy Simulation of Supercritical-Pressure Round Jets," *AIAA Journal*, vol. 48, no. 9, pp. 2133–2144, 2010, doi: http://dx.doi.org/10.2514/1.J050288. 22, 23

[63] Schmitt, T., Ruiz, A., and Selle, L. and Cuenot, B., "Numerical investigation of destabilization of supercritical round turbulent jets using large Eddy simulation," in *Progress in Propulsion Physics*, vol. 2, 2011, pp. 225–238, doi: http://dx.doi.org/10.1051/eucass/201102225. 22, 23

[64] Petit, X., Ribert, G., and Lartigue, G. and Domingo, P., "Large-eddy simulation of supercritical fluid injection," *The Journal of Supercritical Fluids*, vol. 84, pp. 61–73, 2013, doi: http://dx.doi.org/10.1016/j.supflu.2013.09.011. 22

[65] Gnanaskandan, A. and Bellan, J., "Large Eddy Simulations of high pressure jets: Effect of subgrid scale modeling," in *55th AIAA Aerospace Sciences Meeting*. American Institute of Aeronautics and Astronautics, 2017, pp. 461–483, doi: http://dx.doi.org/10.2514/6.2017-1105. 22

[66] Ma, P. C. and Lv, Y. and Ihme, M., "An entropy-stable hybrid scheme for simulations of transcritical real-fluid flows," *Journal of Computational Physics*, vol. 340, pp. 330–357, 2017, doi: http://dx.doi.org/10.1016/j.jcp.2017.03.022. 22

[67] Ningegowda, B. M., Rahantamialisoa, F., Zembi, J., Pandal, A., and Im, H. G. and Battistoni, M., "Large Eddy Simulations of Supercritical and Transcritical Jet Flows Using Real Fluid Thermophysical Properties," in *SAE Technical Paper Series*, 2020, doi: http://dx.doi.org/10.4271/2020-01-1153. 22

[68] Jarczyk, M. and Pfitzner, M., "Large Eddy Simulation of Supercritical Nitrogen Jets," in *50th AIAA Aerospace Sciences Meeting including the New Horizons Forum and Aerospace Exposition*. American Institute of Aeronautics and Astronautics, 2012, doi: http://dx.doi.org/10.2514/6.2012-1270. 22, 23, 42, 53, 54

[69] Antunes, E. L. S. F. and Silva, A. R. R. and Barata, J. M. M., "RANS Modeling of Transcritical and Supercritical Nitrogen Jets," in *53rd AIAA Aerospace Sciences Meeting*,

ser. AIAA 2015-0469. American Institute of Aeronautics and Astronautics, 2015, doi: http://dx.doi.org/10.2514/6.2015-0469. 22

[70] Hirsch, C., *Numerical Computation of Internal and External Flows*, 2nd ed. Elsevier, Burlington, Massachusetts, 2007, vol. 1, ISBN: 978-0750665940. 23, 25, 26, 27, 49, 51, 53, 54

[71] Bellan, J., "Future Challenges in the Modelling and Simulations of High-pressure Flows," *Combustion Science and Technology*, vol. 192, no. 7, pp. 1199–1218, 2020, doi: http://dx.doi.org/10.1080/00102202.2020.1719404. 23, 31

[72] Sierra-Pallares, J., Parra-Santos, M., García-Serna, J., and Castro, F. and Cocero, M. J., "Numerical analysis of high-pressure fluid jets: Application to RTD prediction in supercritical reactors," *The Journal of Supercritical Fluids*, vol. 49, no. 2, pp. 249–255, 2009, doi: http://dx.doi.org/10.1016/j.supflu.2009.01.009. 23, 42

[73] Sierra-Pallares, J., García del Valle, J., and García-Carrascal, P. and Castro Ruiz, F., "Numerical study of supercritical and transcritical injection using different turbulent Prandlt numbers: A second law analysis," *The Journal of Supercritical Fluids*, vol. 115, pp. 86–98, 2016, doi: http://dx.doi.org/10.1016/j.supflu.2016.05.001. 23, 39, 42

[74] Kawai, S. and Oikawa, Y., "Turbulence Modeling for Turbulent Boundary Layers at Supercritical Pressure: A Model for Turbulent Mass Flux," *Flow Turbulence and Combustion*, vol. 104, no. 2-3, pp. 625–641, 2019, doi: http://dx.doi.org/10.1007/s10494-019-00079-z. 23

[75] Park, T. S., "Application of k-ε turbulence models with density corrections to variable density jets under subcritical/supercritical conditions," *Numerical Heat Transfer*, vol. 77, no. 2, pp. 162–178, 2019, doi: http://dx.doi.org/10.1080/10407782.2019.1685817. 23

[76] Poormahmood, A. and Farshchi, M., "Numerical study of the mixing dynamics of trans- and supercritical coaxial jets," *Physics of Fluids*, vol. 32, no. 12, p. 125105, 2020, doi: http://dx.doi.org/10.1063/5.0030183. 23

[77] Lapenna, P. E., "Characterization of pseudo-boiling in a transcritical nitrogen jet," *Physics of Fluids*, vol. 30, no. 7, p. 077106, 2018, doi: http://dx.doi.org/10.1063/1.5038674. 23

[78] Lapenna, P. E. and Creta, F., "Direct Numerical Simulation of Transcritical Jets at Moderate Reynolds Number," *AIAA Journal*, vol. 57, no. 6, pp. 2254–2263, 2019, doi: http://dx.doi.org/10.2514/1.J058360. 23

[79] Wilcox, D., *Turbulence Modeling for CFD*, 3rd ed. DCW Industries, Inc., La Cañada, CA, 2006, ISBN: 978-1928729082. 31, 36, 40, 41

[80] Moore, C., "Ergodic theorem, ergodic theory, and statistical mechanics," *Proceedings of the National Academy of Sciences*, vol. 112, no. 7, pp. 1907–1911, 2015, doi: http://dx.doi.org/10.1073/pnas.1421798112. 31

[81] Launder, B. E. and Spalding, D. B., *Lectures in mathematical models of turbulence*. Academic Press, London, UK, 1972, ISBN: 978-0124380509. 38, 39

[82] Magalhães, L., Antunes, E., and Silva, A. and Barata, J., "Cubic and multiparameter equations of state evaluation for supercritical flow modeling," in *4th Thermal and Fluids Engineering Conference (TFEC)*, ser. TFEC-2019-28385, 2019, doi: http://dx.doi.org/10.1615/TFEC2019.ref.028385. 39, 42

[83] Hoffmann, K. and Chiang, S., *Computational fluid dynamics*, 4th ed. Engineering Education System, 2000, vol. 3, ISBN: 978-0962373107. 40, 41

[84] Taghizadeh, S. and Jarrahbashi, J., "Proper Orthogonal Decomposition Analysis of Turbulent Cryogenic Liquid Jet Injection Under Transcritical and Supercritical Conditions," *Atomization and Sprays*, vol. 28, no. 10, pp. 875–900, 2018, doi: http://dx.doi.org/10.1615/AtomizSpr.2018028999. 42

[85] Li, L., Xie, M., Wei, W., and Jia, M. and Liu, H., "Numerical investigation on cryogenic liquid jet under transcritical and supercritical conditions," *Cryogenics*, vol. 89, pp. 16–28, 2018, doi: http://dx.doi.org/10.1016/j.cryogenics.2017.10.021. 42

[86] Antunes, E. and Silva, A. and Barata, J., "Modelling of transcritical and supercritical nitrogen jets," *Combustion Engines*, vol. 169, no. 2, pp. 125–132, 2017, doi: http://dx.doi.org/10.19206/CE-2017-222. 42

[87] Lemmon, E. W. and Jacobsen, R. T., "Viscosity and Thermal Conductivity Equations for Nitrogen, Oxygen, Argon, and Air," *International Journal of Thermophysics*, vol. 25, no. 1, pp. 21–69, 2004, doi: http://dx.doi.org/10.1023/B:IJOT.0000022327.04529.f3. 44, 45, 47

[88] Olchowy, G. A. and Sengers, J. V., "A simplified representation for the thermal conductivity of fluids in the critical region," *International Journal of Thermophysics*, vol. 10, no. 2, pp. 417–426, 1989, doi: http://dx.doi.org/10.1007/BF01133538. 46

[89] Leonard, B., "A stable and accurate convective modelling procedure based on quadratic upstream interpolation," *Computer Methods in Applied Mechanics and Engineering*, vol. 19, no. 1, pp. 59–98, 1979, doi: http://dx.doi.org/10.1016/0045-7825(79)90034-3.

51, 52

[90] Lacaze, G., Schmitt, T., and Ruiz, A. and Oefelein, J., "Comparison of energy-, pressure- and enthalpy-based approaches for modeling supercritical flows," *Computers & Fluids*, vol. 181, pp. 35–56, 2019, doi: http://dx.doi.org/10.1016/j.compfluid.2019.01.002. 51

[91] Leonard, B., "Order of accuracy of QUICK and related convection-diffusion schemes," *Applied Mathematical Modelling*, vol. 19, no. 11, pp. 640–653, 1995, doi: http://dx.doi.org/10.1016/0307-904x(95)00084-w. 53

[92] Patankar, S. V., *Numerical Heat Transfer and Fluid Flow*, 1st ed.   CRC Press, 1980, doi: http://dx.doi.org/10.1201/9781482234213. 53

[93] Raman, C. V. and Krishnan, K. S., "A New Type of Secondary Radiation," *Nature*, vol. 121, no. 3048, pp. 501–502, 1928, doi: http://dx.doi.org/10.1038/121501c0. 71